REPORT DOCUMENTATION PAGE

Form Approved
OMB No. 0704-0188

1. REPORT DATE *(DD-MM-YYYY)*	**2. REPORT TYPE**	**3. DATES COVERED** *(From - To)*
July 2015	Technical Paper	July 2015-July 2015

4. TITLE AND SUBTITLE
An Investigation of Spectral Imaging of Hall Thruster Plumes

5a. CONTRACT NUMBER
In-House

5b. GRANT NUMBER

5c. PROGRAM ELEMENT NUMBER

6. AUTHOR(S)
Michael Nakles, Michael Holmes, and William Hargus Jr.

5d. PROJECT NUMBER

5e. TASK NUMBER

5f. WORK UNIT NUMBER
Q1AU

7. PERFORMING ORGANIZATION NAME(S) AND ADDRESS(ES)

Air Force Research Laboratory (AFMC)
AFRL/RQRS
1 Ara Drive.
Edwards AFB, CA93524-7013

8. PERFORMING ORGANIZATION REPORT NO.

9. SPONSORING / MONITORING AGENCY NAME(S) AND ADDRESS(ES)
Air Force Research Laboratory (AFMC)
AFRL/RQR
5 Pollux Drive
Edwards AFB CA 93524-7048

10. SPONSOR/MONITOR'S ACRONYM(S)

11. SPONSOR/MONITOR'S REPORT NUMBER(S)
AFRL-RQ-ED-TP-2015-199

12. DISTRIBUTION / AVAILABILITY STATEMENT
Distribution A: Approved for Public Release; Distribution Unlimited.

13. SUPPLEMENTARY NOTES
Technical Paper and Briefing Charts presented at The 34th International Electric Propulsion Conference; Kobe, Japan; 1-6 July 2015. PA#15304.

14. ABSTRACT
An exploratory investigation of measuring xenon spectral emission lines in a Hall thruster plume through optical imaging techniques was performed on the SPT-100 Hall thruster. A 16 bit CCD camera was used with optical interference bandwidth filters to separately photograph neutral (823 nm) and ion (542 nm) xenon emission. The resulting images allowed for examination of the near-plume structure in terms of excited ions and neutral particles for various thruster operating conditions. Abel inversion analysis was applied to the photographs to examine the emission as a function of radius with the assumption of axial symmetry and optically thin plasma. This experimental technique may provide results useful for comparison with numerical near-plume predictions that incorporate collisional radiative models.

15. SUBJECT TERMS

16. SECURITY CLASSIFICATION OF:			**17. LIMITATION OF ABSTRACT**	**18. NUMBER OF PAGES**	**19a. NAME OF RESPONSIBLE PERSON**
					William Hargus
a. REPORT	**b. ABSTRACT**	**c. THIS PAGE**	SAR	40	**19b. TELEPHONE NO** *(include area code)*
Unclassified	**Unclassified**	**Unclassified**			661-275-6799

Standard Form 298 (Rev. 8-98)
Prescribed by ANSI Std. 239.18

An Investigation into the Spectral Imaging of Hall Thruster Plumes

IEPC-2015-416/ISTS-2015-b-416

Presented at Joint Conference of 30th International Symposium on Space Technology and Science, 34th International Electric Propulsion Conference and 6th Nano-satellite Symposium
Hyogo-Kobe, Japan
July 4–10, 2015

Michael R. Nakles*
ERC, Inc., Edwards Air Force Base, CA, 93524

Michael R. Holmes†and William A. Hargus, Jr.‡
Air Force Research Laboratory, Edwards Air Force Base, CA, 93524

An exploratory investigation of measuring xenon spectral emission lines in a Hall thruster plume through optical imaging techniques was performed on the SPT-100 Hall thruster. A 16 bit CCD camera was used with optical interference bandwidth filters to separately photograph neutral (823 nm) and ion (542 nm) xenon emission. The resulting images allowed for examination of the near-plume structure in terms of excited ions and neutral particles for various thruster operating conditions. Abel inversion analysis was applied to the photographs to examine the emission as a function of radius with the assumption of axial symmetry and an optically thin plasma. This experimental technique may provide results useful for comparison with numerical near-plume predictions that incorporate collisional radiative models.

Nomenclature

C	constant that accounts for optical geometry parameters and physical constants in optical calibrations
I_d	anode discharge current
f_i	fractional transmittance of neutral density filter
$\dot{m}_a$	anode propellant mass flow rate
$\dot{m}_b$	mass flow rate of additional background gas
$\dot{m}_c$	cathode propellant mass flow rate
n	CCD count value
P	vacuum chamber pressure
Q	quantum efficiency of CCD
r	radial coordinate about thrust axis
R	radiance
V_d	anode discharge voltage
x	axis in thruster coordinate system perpendicular to the cathode plane
y	axis in thruster coordinate system in the cathode plane
z	axis in thruster coordinate system in thrust direction
Δt	image exposure time
λ	wavelength

*Research Engineer, ERC, Inc., 1 Ara Rd. Edwards AFB, CA 93524
†Research Scientist, AFRL/RQRS, 1 Ara Rd. Edwards AFB, CA 93524
‡Research Engineer, AFRL/RQRS, 1 Ara Rd. Edwards AFB, CA 93524

Introduction

Hall effect thruster plumes present a challenging environment for the implementation plasma diagnostics. The near-plume region is an especially difficult region to characterize where changes in density and temperature occur over short distances. Here, the physical presence of probes is likely to perturb the plasma, affect thruster operation, cause heating effects, and lead to physical degradation of the probe itself. Even sizing a probe small enough for good spatial resolution can be difficult. Optical diagnostics such as laser-induced fluorescence[1] and microwave interferometry[2] are not encumbered by these limitations and have proven useful for reliable near-plume measurements.

The idea of using photography for certain types of plasma characterization is intriguing for its potential advantages. Images provide data in a virtually continuous fashion over a wide measurement domain, whereas most other diagnostics typically measure at one physical location at a time and must be physically moved to create a set of discrete data. The location of the camera outside of the chamber avoids physical disruption of the plasma and allows convenient access for the operator. Photographic images have been used to visually inspect basic changes in plume structure for different thruster operating modes.[3,4] Modern high-speed cameras can record images on timescales that allow the study of plasma oscillation modes in discharge channels.[3,5] Photography with optical filters has been used to image xenon ion and neutral emission separately in an ATON A53 Hall thruster.[6] This data was transformed from line-of-sight data into cross-sectional images of the plume for two operational modes through an inverse Abel transformation.

In this study, a 16 bit camera with optical interference bandwidth filters was used to examine the plasma structure of the near-plume of the SPT-100 in terms of optical emission of the 542 nm xenon ion line and the 823 nm xenon neutral line for various operating conditions. Optical emission is a function of both plasma density and temperature and can be predicted by collisional radiative models. The goal of this study was to examine the structure of the near-plume of the SPT-100 thruster at various operating conditions and to explore the use of Abel inversion analysis to deconvolve the image line-of-sight data into a radially dependent function with the assumption of axially symmetry and an optically thin plasma. The results of this experimental imaging may provide a useful comparison tool for numerical simulations of the near-plume region that incorporate collisional radiative models.

Experimental Apparatus and Techniques

Hall Effect Thruster

A flight model SPT-100 Hall effect thruster (Fig. 1) was used in this study. The axisymmetric thruster is equipped with two lanthanum hexaboride (LaB_6) cathodes (only one was used during these tests). This thruster has a conventional five magnetic core (one inner, four outer) magnetic circuit. Discharge current is routed through the magnetic circuit and thus no extra power source for the magnets is required. The acceleration channel of the thruster has a 100 mm outer diameter, a 69 mm inner diameter, and a channel depth of 25 mm. For its nominal xenon operating condition, the thruster has been characterized to have a thrust of 83 mN with a specific impulse of 1,600 s, yielding an anode efficiency near 50%.[7]

For this study, the thruster and cathode were powered with commercial off-the-shelf Sorenson power supplies instead of the PPU used on-orbit. A computer data acquisition system recorded the potential and current outputs of the power supplies used in the thruster operation at a rate of 2 Hz. For propellant flow, digital mass flow controllers from Aera dispersed gas to the anode and cathode taking the place of the xenon flow control system (XFC) used on-orbit. Therefore, propellant flow rate was constant for each given operating condition and not controlled by discharge current feedback as with an XFC system.

Test Facility

This study utilized Chamber 1 (Fig. 2(a)) at the Air Force Research Laboratory at Edwards Air Force Base. Chamber 1 is a cylindrical non-magnetic stainless steel vacuum chamber 2.4 m in diameter and 4.1 m in length. Pumping is provided by two liquid nitrogen baffled (70 K), 1.2 m flanged gaseous helium two stage cryogenic (15 K) vacuum pumps with a measured pumping speed on xenon of 48,500 L/s. Chamber pressure is monitored with a hot filament ionization gauge.

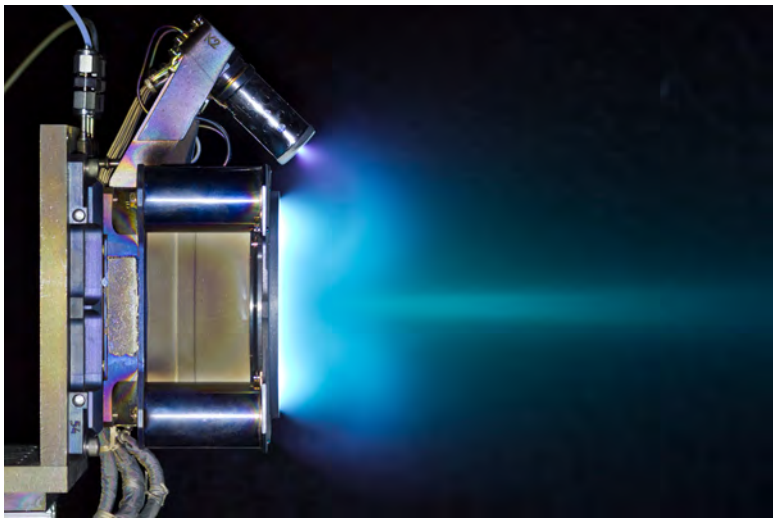

Figure 1. The SPT-100 firing in Chamber 1 photographed by a digital SLR from the same perspective as the scientific images presented in this study.

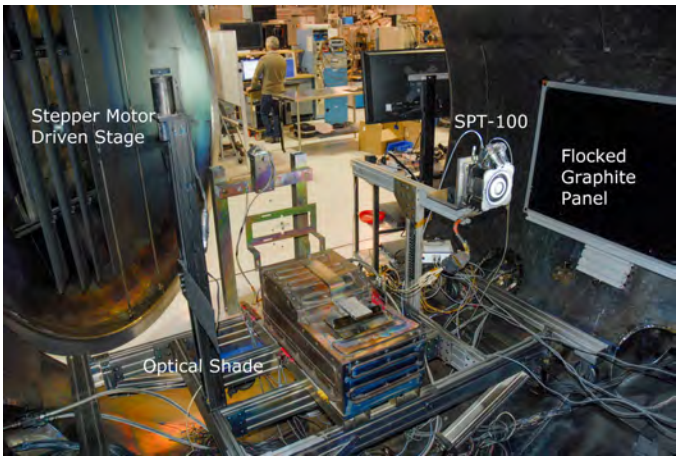

(a) The SPT-100 installed in Chamber 1 for the optical imaging. The optical viewport for imaging is beyond the left photo border.

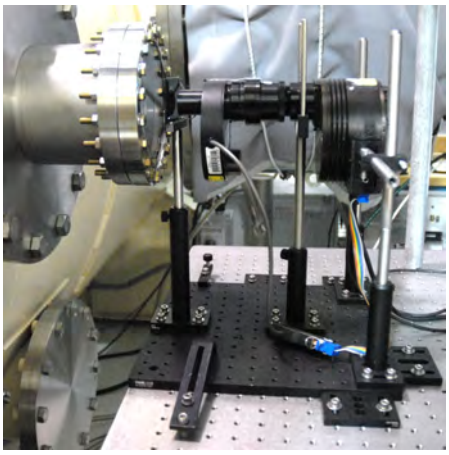

(b) The SBIG ST-10XE camera and optical components.

Figure 2. Experimental Setup

Optical Components

Camera

A Santa Barbara Instruments Group (SBIG) ST-10XE 16 bit CCD camera (Fig. 2(b))was used for this imaging experiment. It employs a Kodak KAF-3200E 3 megapixel CCD (2184×1472 with 6.8 μm pixels). The camera was designed for astronomical imaging and thus long exposure durations (the fastest shutter speed is 0.12 s). It interfaces with t-mount optical components. The instrument has an electronic chiller to reduce thermal image noise, which was set to 5°C for these measurements. A 70 mm focal length lens was mounted to the camera along with a variable aperture diaphragm set to a 9.7 mm diameter making for an f-number of f/7.2. Optical filters were stored and positioned with an SBIG CW-8 electronic filter wheel. The camera was controlled with a laptop PC. See Fig. 4 for a schematic of the optical set up.

Filters

Two 25 mm diameter interface filters from Custom Scientific were used to isolate xenon spectral emission lines. Singly charged ion emission was photographed through a bandwidth filter centered at 542 nm filter

with a transmission distribution function having a full width at half maximum (FWHM) of 10 nm. Neutral xenon emission was photographed with a filter centered at 823 nm also with a FWHM of 10 nm. Besides collecting signal from the 823 nm neutral line, this filter also gathers emission from the 828 nm neutral line. The high f-number of the optical setup prevented light with high incidence angle from reaching the CCD, which minimized potential filter tuning effects. Figure 3 shows the filter transmission functions along with the spectral radiance of the SPT-100 measured with a spectrometer through a diffuse optical collector.

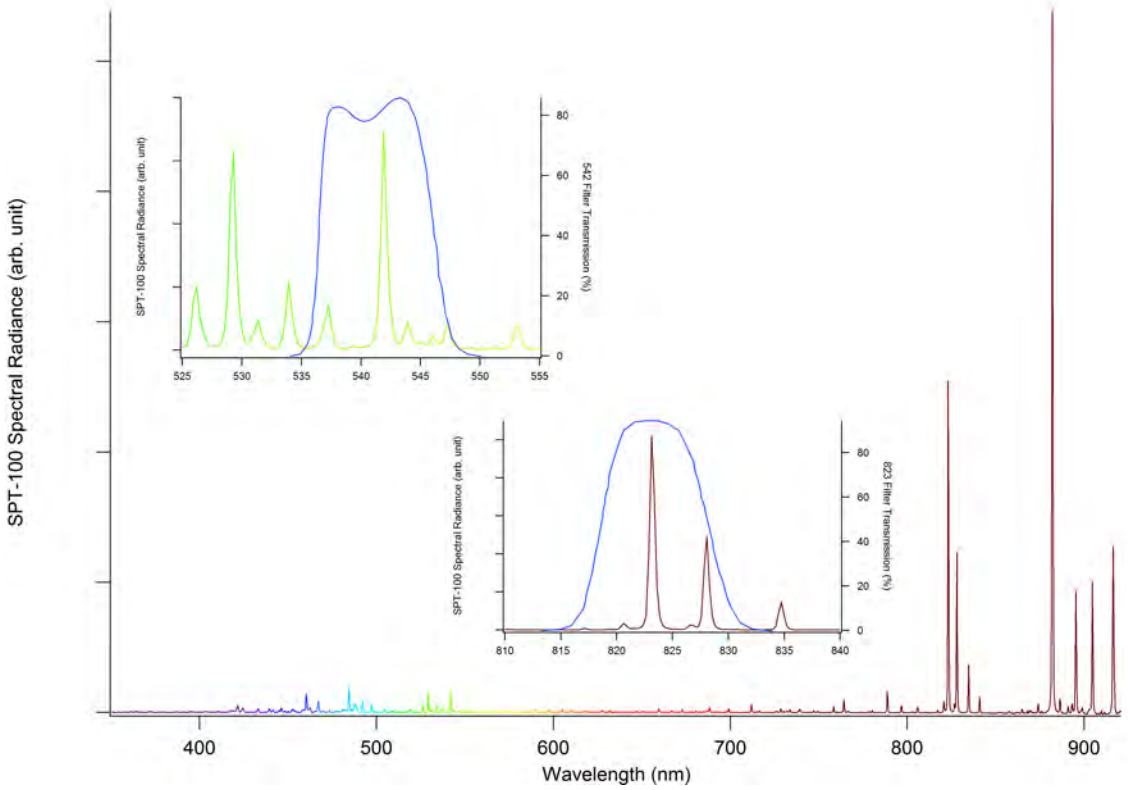

Figure 3. Filter transmission.

Testing Methodology

Optical Techniques

The SPT-100 was mounted with its centerline 198 cm from a 20 cm dia. optical view port on a lateral side the vacuum chamber. The camera was mounted on an optics table outside the chamber and pointed through the window for a profile view of the thruster and plume (Figs. 1 and 4). A flocked graphite panel was placed behind the thruster to serve as an non-reflective black background for the images.

The shiny surfaces of the optical interference filters in conjunction with the other optical surfaces created a mirrored and inverted reflection of the plume about the vertical centerline of the photo that appeared in the camera images. Constraining the plume image to one side of the frame was necessary to prevent unwanted reflections from becoming superimposed on the primary plume image. Thus, the thruster was framed in the camera's field of view with its plume confined to the right half the frame (with its downstream axis pointing rightward). Unfortunately, this solution to the reflection problem required discarding one half of the image area.

A motion stage controlled optical shade (Figs. 2(a) and 4) was constructed from a grafoil (flexible graphite) sheet covered with graphite felt and placed inside the chamber so that certain regions of the thruster, which varied drastically in brightness, could be selectively blocked from the view of the camera. The shade could be positioned so that it blocked the cathode (very bright neutral emission) or the region of the plume upstream of z=134 mm. Blocking bright regions of emission allowed for exposures of dimmer regions that more fully utilized the bit depth of the CCD by preventing overexposed regions with pixel bleeding. In some cases,

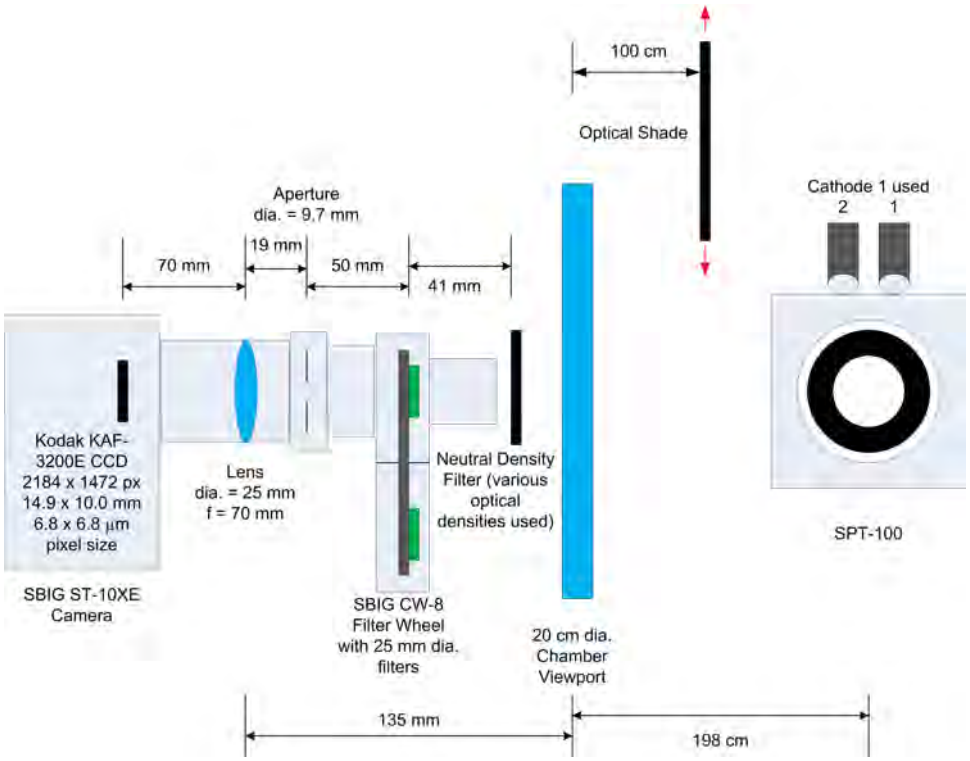

Figure 4. Schematic of optical setup

separate exposures for different regions were combined to form a composite photo, effectively increasing the dynamic range of the image. Three different neutral density (powers of 0.75, 2.0, and 2.5) were used to enable exposure times of between 1 s and 30 s and were selected based on the brightness of the region being photographed.

To improve the signal to noise ratio in the photographs, 10 exposures were averaged for each image. A dark frame (photo with shutter closed) for the same exposure duration and same CCD temperature was subtracted to remove noise caused by thermal effects. Images were also corrected with flat field images, which are images of a uniformly lit flat surface. Images are divided by the flat field image to correct for vignetting and variations in pixel response. Flat field corrections are important in photometric studies such as the present one where vignetting caused up to a 60% brightness variation between the image center and corner in uncorrected images.

Calibrations of the optical system were performed by photographing an integrating sphere inside the chamber illuminated by an Oriel Model 63355 quartz tungsten halogen lamp with a NIST traceable irradiance curve. Calibration photographs were used to determine the fractional transmittance of each neutral density filter at 542 nm and 823 nm. The relative quantum efficiency of the CCD at 542 nm and 823 nm was also measured through calibration photos. With knowledge of these parameters, images taken with different neutral density filters and interference filters could be scaled relative to each other in terms of radiance according to Eq. 1.

$$R = \frac{Cn}{Q\lambda\Delta t f_i} \tag{1}$$

Tests were performed to measure pixel response with exposure time to determine the point near the upper limit of pixel count range where the CCD response became nonlinear. All image exposure times were selected to ensure that pixel counts never exceeded the linear response limit.

Inverse Abel Transformation

These photographic images can be considered to approximate a line-of-sight data set where plume emission is integrated along the x-axis of the thruster coordinate system. In order to study emission as a function of r, an Abel inversion deconvolution was applied to image data. Besides the line-of-sight assumption, the plasma was also assumed to be optically thin and radially symmetric along the z-axis for a given direction of the y-axis. In this study, the half of the plume in the positive y-axis (non-cathode side) was chosen for Abel analysis because it was assumed to have a higher degree of symmetry due to less perturbation from cathode.

The forward Abel transform for a radially symmetric function, $f(r)$ is given by[8]

$$F(y) = 2\int_y^\infty \frac{f(r)rdr}{\sqrt{r^2 - y^2}} \tag{2}$$

and the analytical inverse transformation is

$$f(r) = -\frac{1}{\pi}\int_r^\infty \frac{dF}{dy}\frac{dy}{\sqrt{y^2 - r^2}} \tag{3}$$

The inverse Abel transform is impractical to solve directly with numerical data due to the fact that it requires differentiation of experimental data, which may be noisy, and contains a singularity.[9] There are several types of approaches to performing the inverse Abel transform.[10–12] Here the Fourier method described in Ref. 10 was used where the unknown radial function is constructed from a series expansion of cosine terms each multiplied by an amplitude factor. The amplitude value for each cosine term is determined through a least squares fit of the forward Abel transform equation with the line-of-sight data. The number of cosine terms chosen for the expansion determines the amount of resolution and noise filtering in the transform. In the present study, 50 cosine terms were used.

Thruster Operating Conditions

Thruster operating conditions for imaging were selected so that the effects of background pressure, discharge voltage, and propellant flow rate on emission could be characterized. The operating conditions photographed are summarized in Table 1. To artificially increase chamber background pressure, extra xenon gas was flowed into the chamber through a feed through at the chamber wall that was 5 cm downstream from the thruster exit plane and 70 cm from the thruster center line. Discharge voltage and propellant flow rates values were increased and decreased by 30% of their nominal values. It is important to note that varying propellant flow rate also affects this thruster's magnetic field because the discharge current is routed through the magnet coils. Therefore, changes in the plume emission for these cases are a result of both factors.

Operating Condition	V_d **(V)**	I_d **(A)**	**Power (W)**	$\dot{m}_a$ **(mg/s)**	$\dot{m}_c$ **(mg/s)**	$\dot{m}_b$ **(mg/s)**	P **(Torr-Xe)**
Nominal	300	4.61	1383	5.15	0.40	0.00	2.28E-05
High Back. Press.	300	4.57	1371	5.15	0.40	4.22	4.55E-05
Low Dis. Voltage	210	4.60	966	5.15	0.40	0.00	2.09E-05
High Dis. Voltage	390	4.56	1778	5.15	0.40	0.00	2.08E-05
Low Prop. Flow Rate	300	2.90	870	3.60	0.28	0.00	1.52E-05
High Prop. Flow Rate	300	5.99	1797	6.69	0.51	0.00	2.74E-05

Table 1. Thruster operating specifications.

Results

For each parameter variation, radiance photograph sets are presented for 542 nm and 823 nm emission showing the low and high value parameter cases side-by-side along with an image showing the change in radiance of the high value parameter case relative to the low value case (Figs. 5, 6, 9, 10, 12, and 13). For the delta images, gaussian smoothing was applied to the original images to control noise amplified through division. Linear color maps are applied to the images to illustrate the variation in radiance near the exit plane. However, radiance decays rapidly beyond about a thruster diameter downstream of the exit plane so

logarithmic contour lines are also added to delineate the shape and magnitude of the radiance. The lowest value contour lines were sometimes omitted where the data was noisy. Blocks were added to the images to denote the channel geometry. Only the plume downstream of the exit plane was photographed so any data that appears to be in the acceleration channel should be ignored. Abel inversion transform analysis was performed for the background pressure and discharge voltage variation cases at six different z-axis locations (2.5, 5, 10, 20, 40, and 80 mm). These data are presented along with the corresponding line-of-sight radiance data (Figs. 7 and 11).

Figures 5 and 6 show the 542 and 823 nm emission, respectively, for the background pressure variation. These photos show a distinct change of the emission structure of the plume for high background pressure where both ion and neutral emission decrease in the plume central core beyond z=50 mm and increase in the laterally surrounding areas. An interesting feature of highly increased 823 nm emission (and 542 nm emission to a lesser degree) is observed near the exit plane outside of the acceleration channel on the non-cathode side of the thruster (y=75 mm). This feature is asymmetric and not observed on the cathode side of the image. With the exception of the plume core, 823 nm emission increases throughout the measurement domain due to the higher density of neutral xenon atoms throughout the operating environment. However, fig. 5(c) shows a 10% decrease in 542 nm emission immediately downstream of the center magnetic pole within 20 mm of the exit plane while emission directly downstream of the acceleration channel remains nearly constant.

This region of decreased emission in the center of the plume may indicate a decrease of interaction between ion beams from opposite sides of the acceleration channel due to a smaller beamlet divergence angle at the exit plane. A study of the effects of background pressure on the SPT-100 performance observed that thrust increases with increasing background pressure.[13] This thrust increase was attributed mostly to decreased plume divergence as measured by probes, which may have been caused by the ion acceleration zone shifting to a more upstream location in the discharge channel as observed in Ref. 14 for the BHT-600 thruster likely due to increased electron mobility from Bohm diffusion.

Figure 7(a) shows a similar ion emission radial profile (calculated through Abel inversion) emanating from the discharge channel for both background pressures through z=20 mm. At 40 mm and beyond, the lower emission at center of the plume is consistent with the observations made from the line-of-sight data. The z=2.5 mm radial profile for the 823 nm emission shown in Fig. 7(b) shows a distinct maxima at the edges of the acceleration channel and a dip in the center. Interestingly, this distribution profile along the channel exit is consistent with laser-induced fluorescence measurements of neutral density for the SPT-140 described in Ref.15. Unlike the ion radial profiles, the neutral profiles change quickly between the two pressure cases with downstream distance. At z = 10 mm the local maxima from the discharge channel edges disappears for the high pressure case and the localized region of high emission centered at y=75 mm and z=20 mm distinctly appears as shown in Fig. 6(c).

The difference between 542 and 823 nm emission for the nominal operating condition is presented in Fig. 8. Throughout the plume, the radiance of the neutral line is stronger. The regions with the highest relative 542/823 emission are the central core of the plume beyond z=50 mm and near the exit of the acceleration channel The regions with the lowest relative emission are found in the lateral areas outside of the thruster plume where there are very few ions.

Figures 9 and 10 show the emission for the discharge voltage variation operating conditions. Figure 9(c) shows that increasing discharge voltage increases ion emission in the plume core 100 mm downstream of the exit plane while it decreases elsewhere. This plume shape may be indicative of the higher energy ions undergoing collisions from geometrical beam interactions farther downstream. A similar, but more broad collision region is seen for the neutral emission in Fig. 10(c) which may be from the beam ions colliding with the diffuse neutral propellant.

The radial ion emission profiles shown in Fig. 7(a) show a similar shape between the two discharge voltage cases with the low discharge voltage case emission significantly stronger near the exit plane. The magnitude of emission becomes nearly the same at z=80 mm. A similar trend is seen for the neutral emission in Fig. 7(b), but the high discharge voltage emission in the central plume is seen to be greater for the 40 and 80 mm traces.

Propellant flow rate effects (in combination with magnetic field effects) are shown in Figs. 12 and 13. Figures 12(b) and 12(b) show that at high propellant flow rate, the magnitude of the radiance becomes much greater and the plume emission appears spherical likely due to a higher rate of scattering collisions with the higher density of unionized propellant. This emission shape is a drastic change from the other test conditions where the shape appears to be influenced by geometrical beam interactions. The total thruster

radiance increases dramatically for these high flow rate cases because of the highly increased collisionality of the plume. The increase in collisions happens mostly in the first 100 mm of the exit plane.

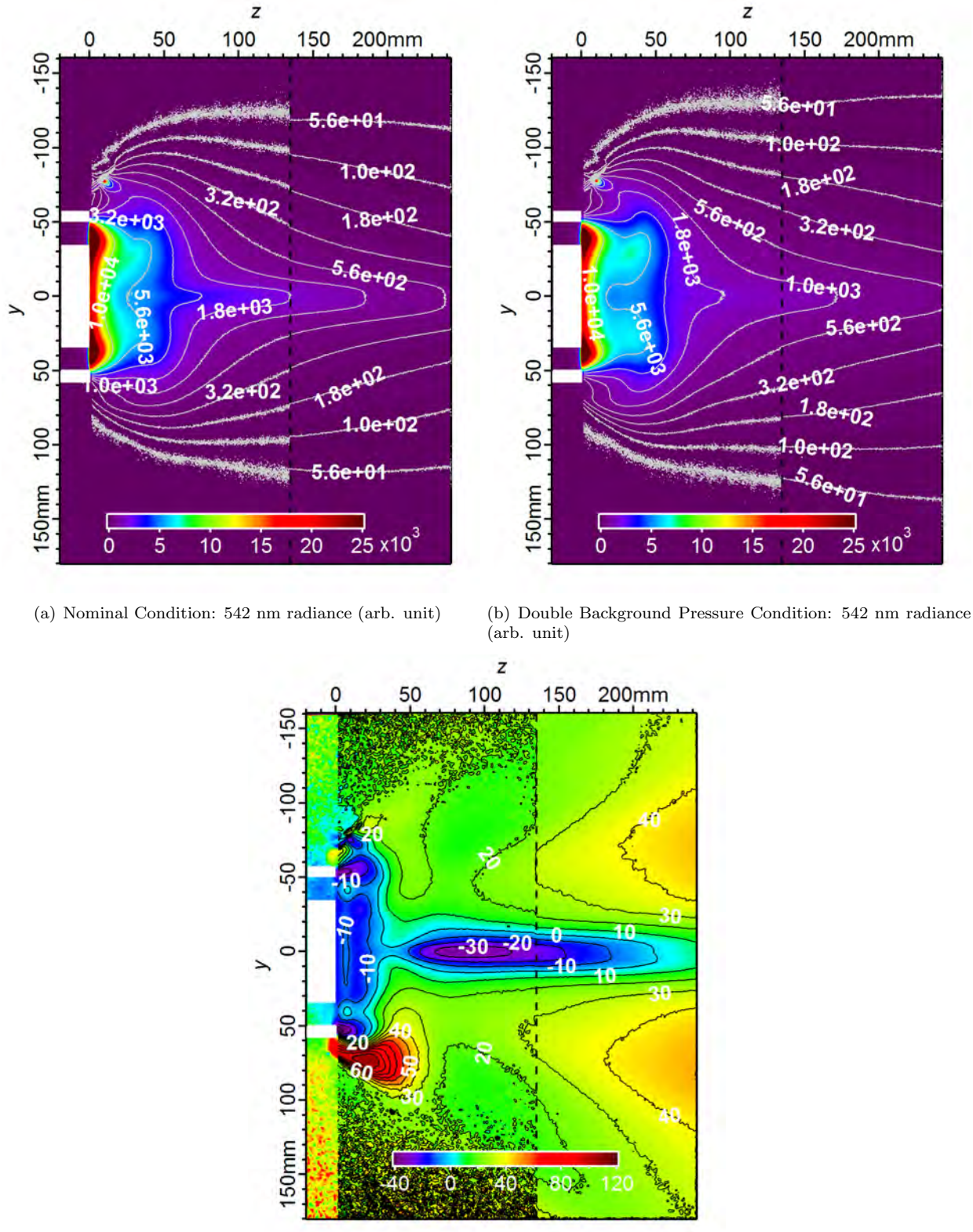

(a) Nominal Condition: 542 nm radiance (arb. unit)

(b) Double Background Pressure Condition: 542 nm radiance (arb. unit)

(c) Δ Radiance (%): $(R_{542:DP} - R_{542:Nom})/R_{542:Nom} \times 100$

Figure 5. Ion emission radiance (542 nm) of the nominal operating condition and the double background pressure condition. Dotted lines mark boundaries of composite photos.

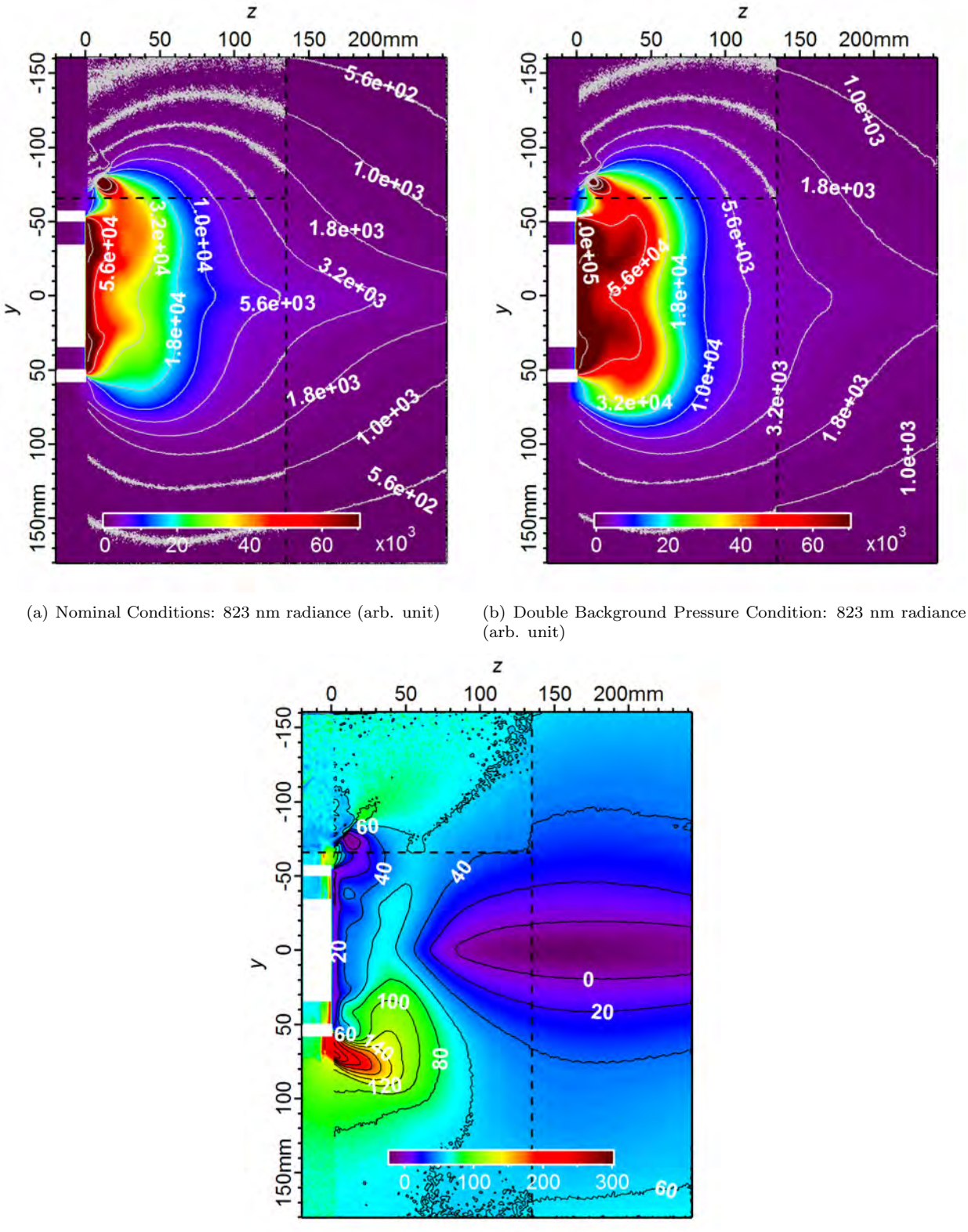

(a) Nominal Conditions: 823 nm radiance (arb. unit)

(b) Double Background Pressure Condition: 823 nm radiance (arb. unit)

(c) Δ Radiance (%): $(R_{823:DP} - R_{823:Nom})/R_{823:Nom} \times 100$

Figure 6. Neutral emission radiance (823 nm) of the nominal operating condition and double background pressure condition. Dotted lines mark boundaries of composite photos.

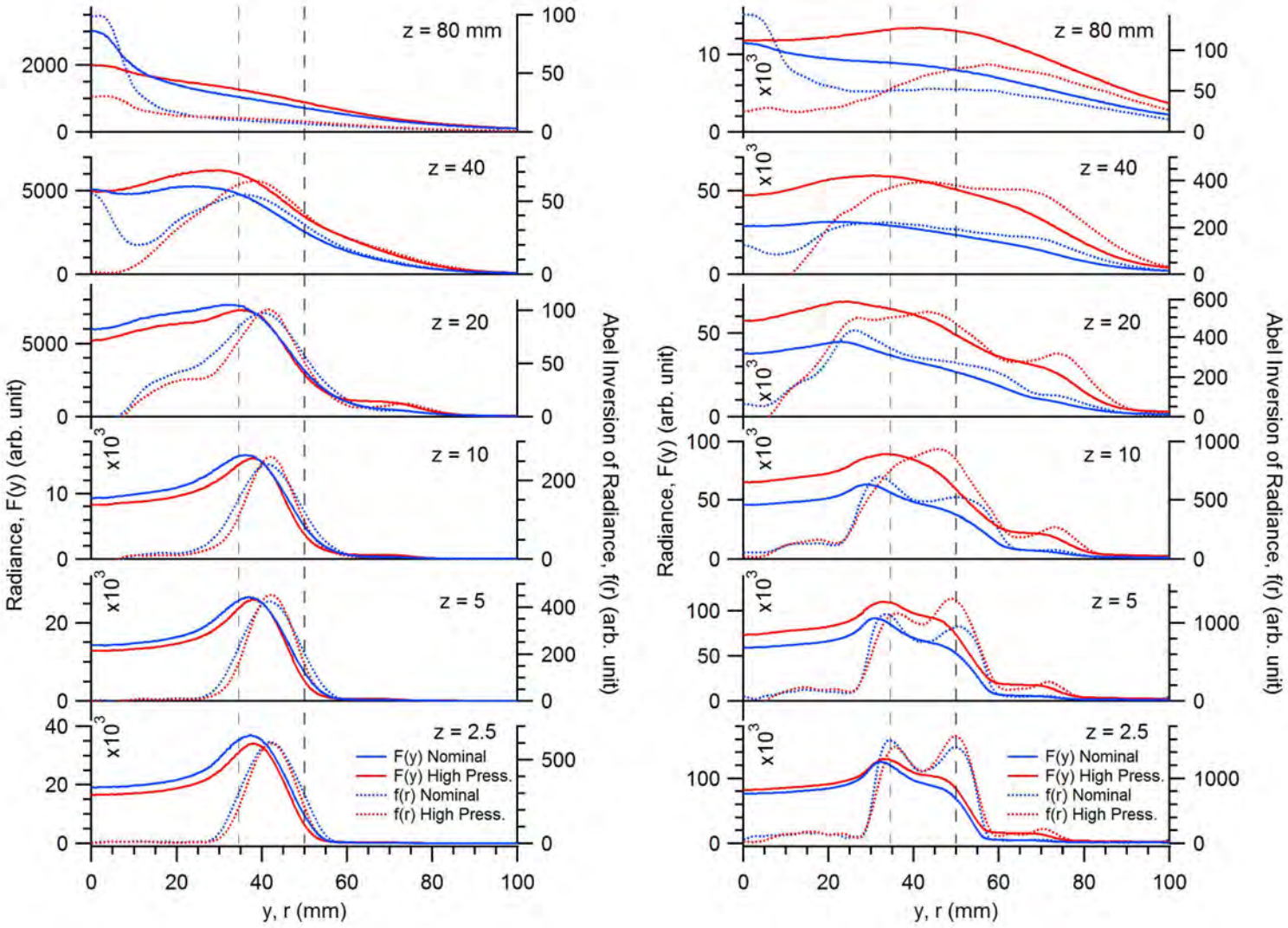

(a) 542 nm emission

(b) 823 nm emission

Figure 7. Cross sections of radiance data for the nominal and high background pressure case at various z locations and their inverse Abel transforms. Dashed lines represent acceleration channel boundaries.

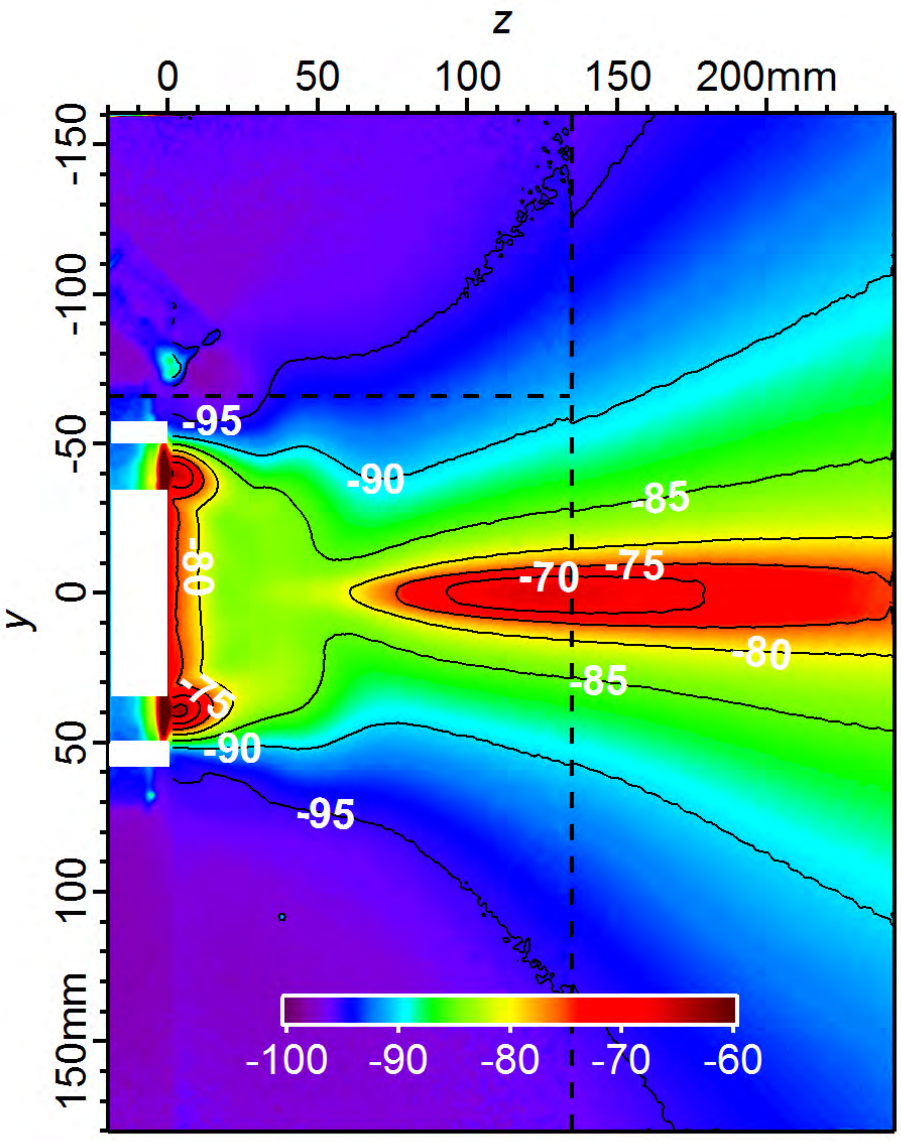

Figure 8. Δ Radiance (%): $(R_{542:Nom} - R_{823:Nom})/R_{823:Nom} \times 100$

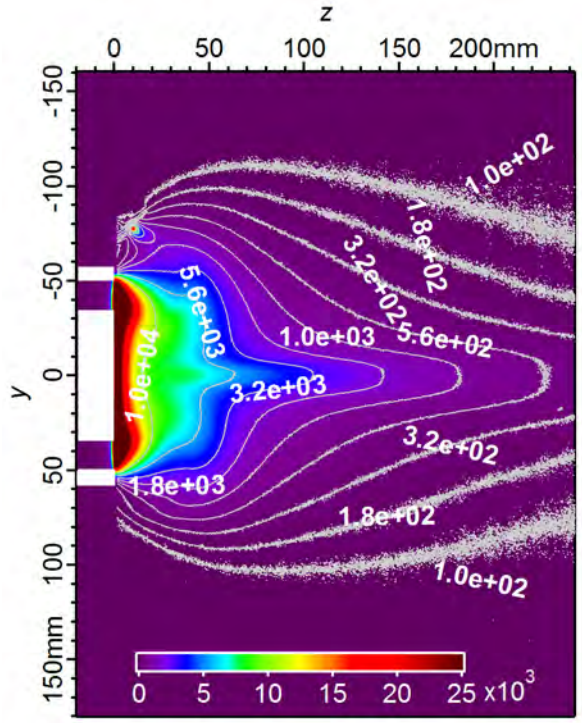

(a) V_d =210 V: 542 nm Radiance (arb. unit)

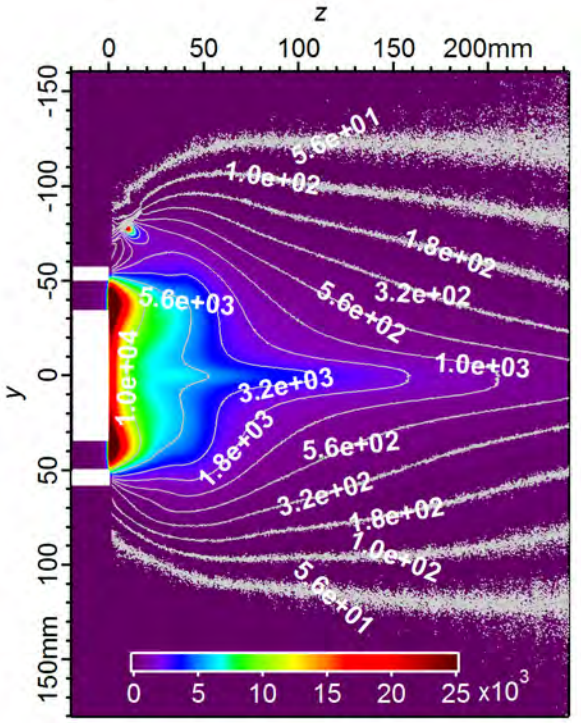

(b) V_d =390 V: 542 nm Radiance (arb. unit)

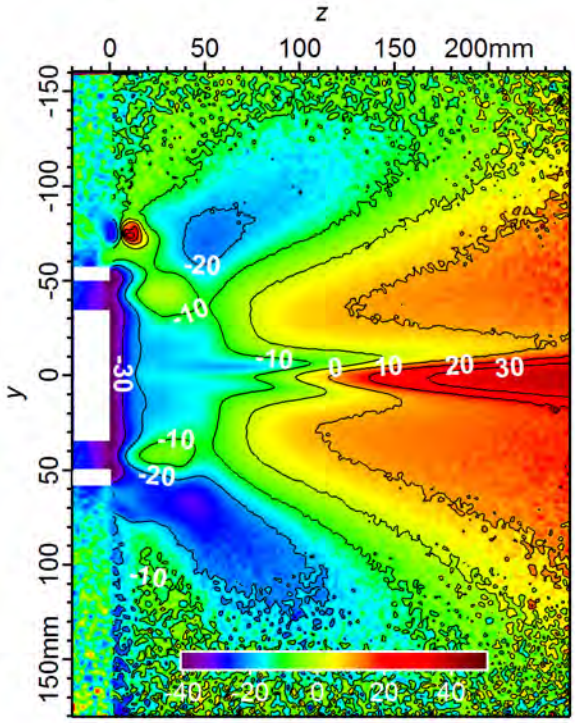

(c) Δ Radiance (%): $(R_{542:Vd390} - R_{542:Vd210})/R_{542:Vd210} \times 100$

Figure 9. Ion emission radiance (542 nm) of the V_d =210 V operating condition and the V_d =390 V condition.

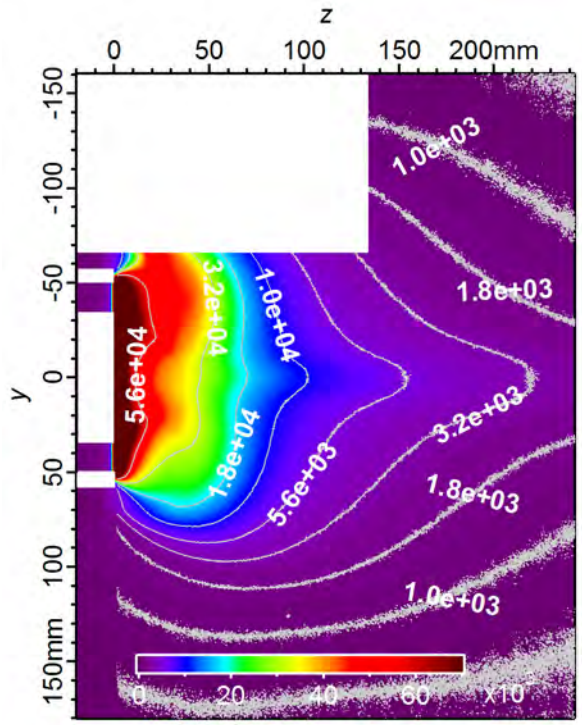

(a) V_d =210 V: 823 nm Radiance (arb. unit)

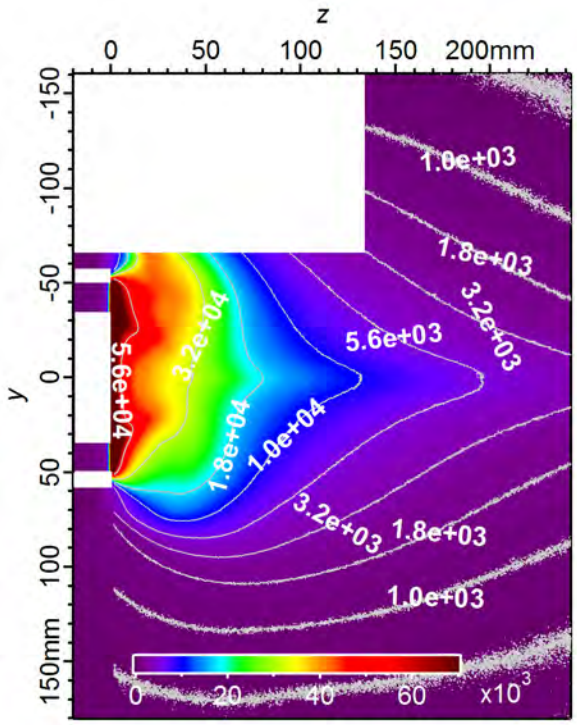

(b) V_d =390 V: 823 nm Radiance (arb. unit)

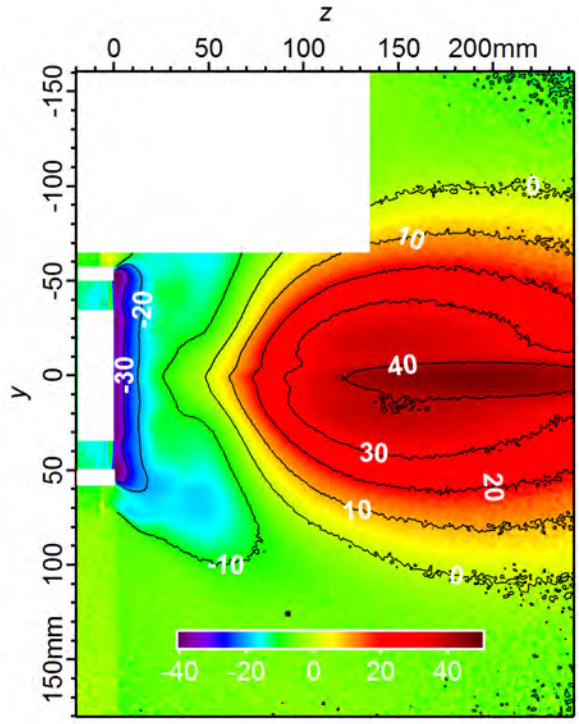

(c) Δ Radiance (%): $(R_{823:Vd390} - R_{823:Vd210})/R_{823:Vd210} \times 100$

Figure 10. Neutral emission radiance (823 nm) of the V_d =210 V operating condition and the V_d =390 V condition. Missing image portion is where optical shade blocked view of cathode.

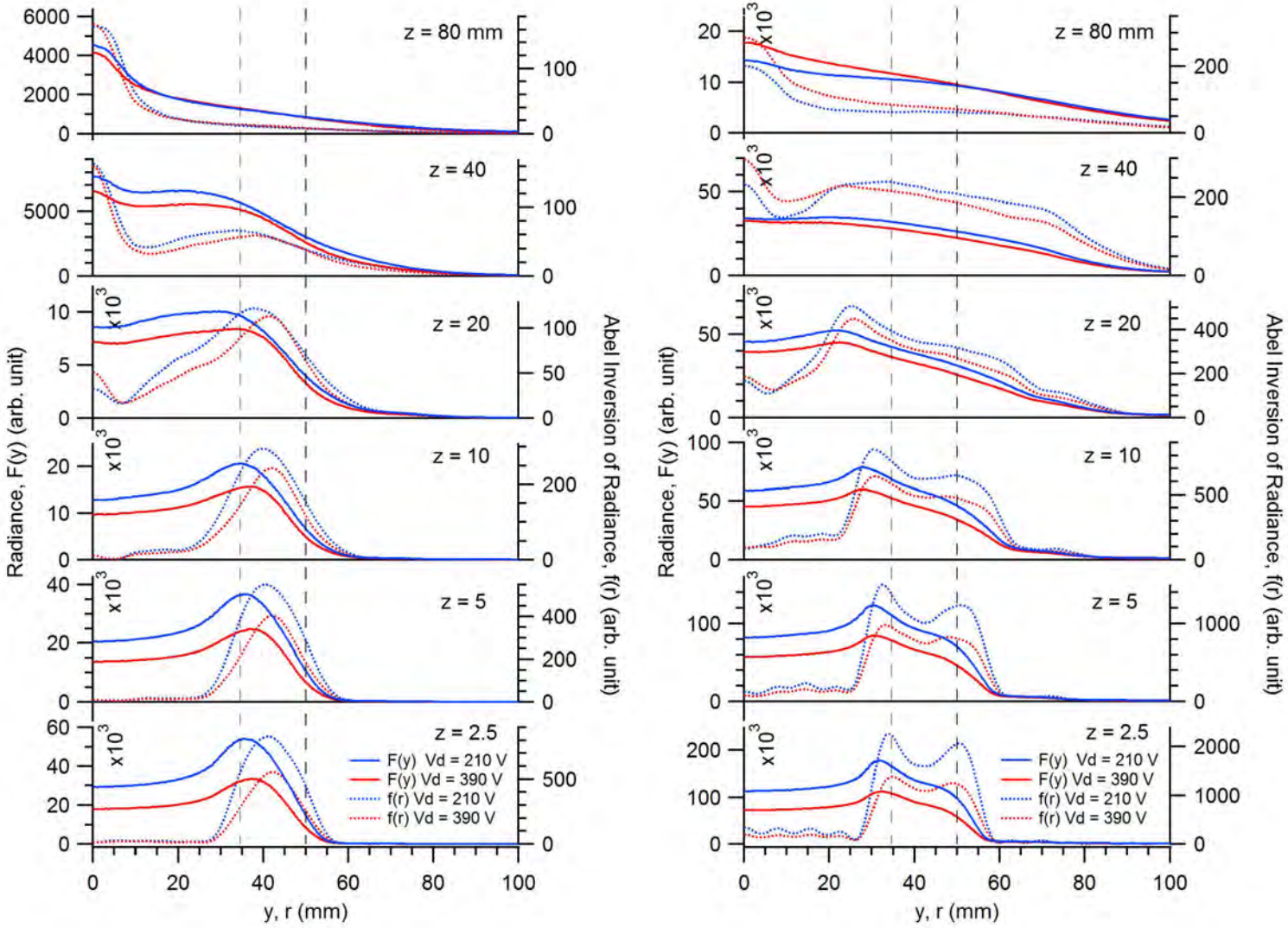

(a) 542 nm emission

(b) 823 nm emission

Figure 11. Cross sections of radiance data for the V_d =210 V and V_d =390 V cases at various z locations and their inverse Abel transforms. Dashed lines represent acceleration channel boundaries.

Conclusions

The imaging of a Hall thruster plume with spectral line filters shows distinct changes in the plume emission structure from ions and neutral particles as operating conditions are changed. These changes reflect variations in plume density and temperature. Photographic measurements can be used as a convenient method for qualitatively examining plume structure, but may also provide a source of useful quantitative analysis when compared to collisional radiative models in numerical simulations or if they can be correlated to other diagnostic measurements of density and/or temperature.

The experimental techniques used in this study showed good promise. Exposures of separate regions of the plume with various integration times and neutral density filters scaled remarkably well in magnitude and plume features blended almost seamlessly when combined for composite images. Overall, the Abel inversion of the photographic data appeared to resolve the evolution of the plume from the exit plane with good detail showing effects that corresponded with the channel geometry. In a few cases, the inversion had trouble resolving data near the plume center and resulted in negative values, but perhaps using a different range of cosine frequencies for the solution or a different inversion technique may alleviate the problem.

In the future, photographic measurements may be performed to match a numerically simulated data set that includes a collisional radiative model for model validation purposes. A more thorough optical calibration technique would allow absolute measurements of thruster radiance, which would add extra value for comparison. Near-field probe measurements of density may be performed to explore the possibility of using photographic data to estimate density values where temperature gradients are sufficiently low. It may be interesting to photograph these probes in the near-field plume to examine the effect their presence has on plasma. The photographic techniques in this study may also be applicable to high-speed photography where time-resolved measurements could be used to study emission as a function of thruster breathing mode oscillations.

References

[1]Hargus Jr., W. A. and Cappelli, M. A., "Laser-Induced Fluorescence Measurements of Velocity within a Hall Discharge," *Applied Physics B*, Vol. 72, No. 8, June 2001, pp. 961–969.

[2]Reed, G. D., William A. Hargus, J., and Cappelli, M. A., "Microwave interferometry (90 GHz) for Hall Thruster Plume Density Characterization," *Proceedings of the 41st AIAA/ASME/SAE/ASEE Joint Propulsion Conference and Exhibit*, 2005, AIAA-2005-4399.

[3]Sekerak, M. J., *Plasma Oscillations and Operational Modes in Hall Effect Thrusters*, Ph.D. thesis, University of Michigan, 2014.

[4]Brown, D. L., *Investigation of Low Discharge Voltage Hall Thruster Characteristics and Evaluation of Loss Mechanisms*, Ph.D. thesis, University of Michigan, 2009.

[5]Sekerak, M. J. et al., "Azimuthal Spoke Propagation in Hall Effect Thrusters," *IEEE Transactions On Plasma Science*, Vol. 43, No. 1, 2014, pp. 72–85.

[6]Roche, S., Bechu, S., Prioul, M., Pagnon, D., Gascon, N., Bouchoule, A., Magne, L., Lasgorceix, P., and Touzeau, M., "Plasma characterisation of an ATON-Hall thruster - Channel and plume investigation," *Proceedings of the 36th AIAA/ASME/SAE/ASEE Joint Propulsion Conference and Exhibit*, 2000, AIAA-2000-3523.

[7]Garner, C. E., Brophy, J. R., Polk, J. E., and Pless, L. C., "Cyclic Endurance Test of a SPT-100 Stationary Plasma Thruster," *In the Proceeding of the 30th AIAA/SAE/ASME/ASEE Joint Propulsion Conference and Exhibit*, 1994, AIAA-94-2856.

[8]Hutchinson, I., *Principles of Plasma Diagnostics*, Cambridge University Press, New York, 1994.

[9]Dribinski, V., Ossadtchi, A., Mandelshtam, V. A., and Reisler, H., "Reconstruction of Abel-transformable images: The Gaussian basis-set expansion Abel transform method," *Review of Scientific Instruments*, Vol. 73, No. 7, 2002, pp. 2634–2642.

[10]Pretzier, G., Jger, H., Neger, T., Philipp, H., and Woisetschlger, J., "Comparison of Different Methods of Abel Inversion Using Computer Simulated and Experimental Side-On Data," *Zeitschrift fr Naturforschung*, Vol. 47a, 1992, pp. 955–970.

[11]Fulge, H., Knapp, A., Eichhorn, C., Wernitz, R., Lohle, S., Fasoulaskand, S., and Herdrich, G., "Improved Abel Inversion Method for Analysis of Spectral and Photo-Optical Data of Magnetic Influenced Plasma Flows," *Proceedings of the 42nd AIAA Plasmadynamics and Lasers Conference*, 2011, AIAA-2011-3456.

[12]Matlock, T., Hargus, Jr., W., Larson, C., and Nakles, M., "Inversion Method for Reconstructing Hall Thruster Plume Parameters from Optical Measurements," *43rd AIAA/ASME/SAE/ASEE Joint Propulsion Conference*, Cincinnati, OH, 2007, AIAA-2007-5303.

[13]Diamant, K. D., Liang, R., and Corey, R. L., "The Effect of Background Pressure on SPT-100 Hall Thruster Performance," *Proceedings of the 50th AIAA/ASME/SAE/ASEE Joint Propulsion Conference*, 2014, AIAA-2014-3710.

[14]Nakles, M. R. and Hargus Jr., W. A., "Background Pressure Effects on Ion Velocity Distribution Within a Medium-Powered Hall Thruster," *Journal of Propulsion and Power*, Vol. 27, No. 4, 2011, pp. 737–743.

[15]Crofton, M. et al., "Neutral Density in the SPT-140 Near-Field Plume," *Proceedings of the 33rd International Electric Propulsion Conference*, 2013, IEPC-2013-399.

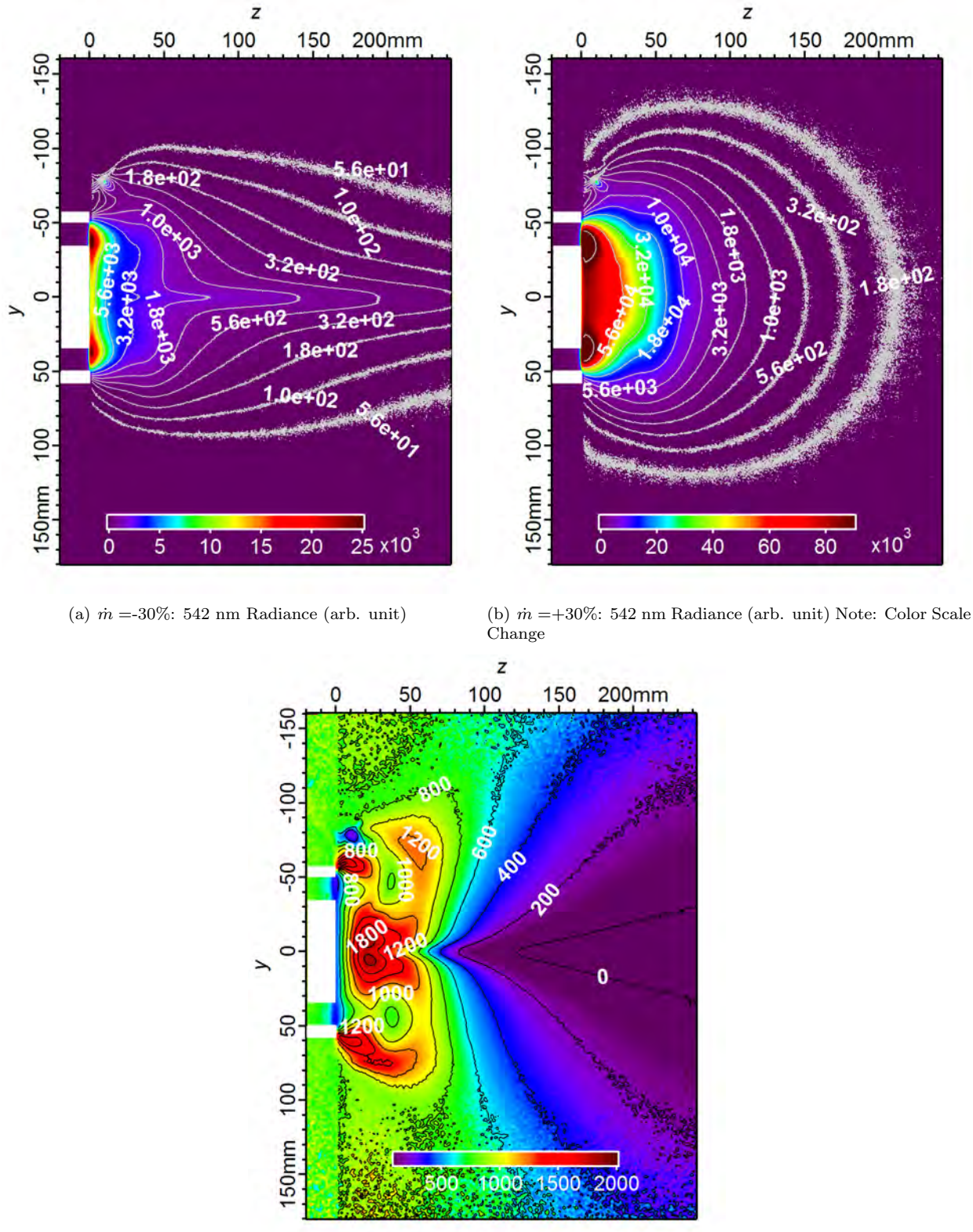

(a) $\dot{m}$ =-30%: 542 nm Radiance (arb. unit)

(b) $\dot{m}$ =+30%: 542 nm Radiance (arb. unit) Note: Color Scale Change

(c) Δ Radiance (%): $(R_{542:m+30\%} - R_{542:m-30\%})/R_{542:m-30\%} \times 100$

Figure 12. Ion emission radiance (542 nm) of the $\dot{m}$ =-30% operating condition and the $\dot{m}$ =+30% condition.

Joint Conference of 30th ISTS, 34th IEPC and 6th NSAT, Kobe-Hyogo, Japan, July 4-10, 2015

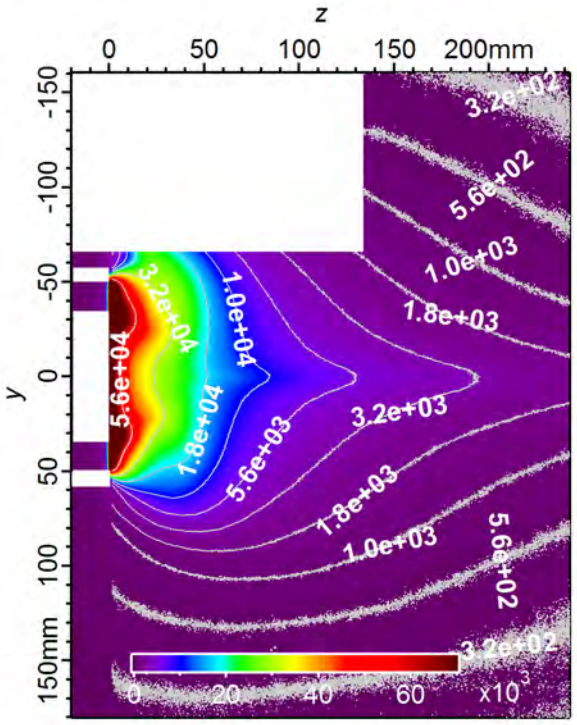

(a) $\dot{m}$ =-30%: 823 nm Radiance (arb. unit)

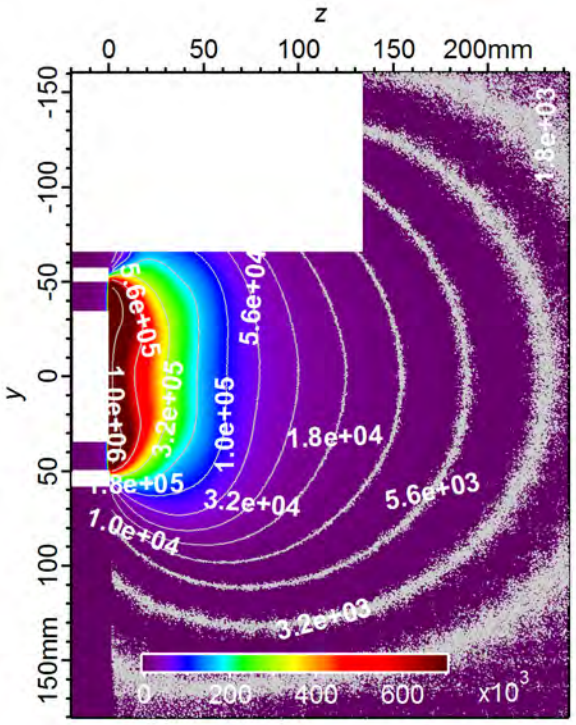

(b) $\dot{m}$ =+30%: 823 nm Radiance (arb. unit) Note: Color Scale Change

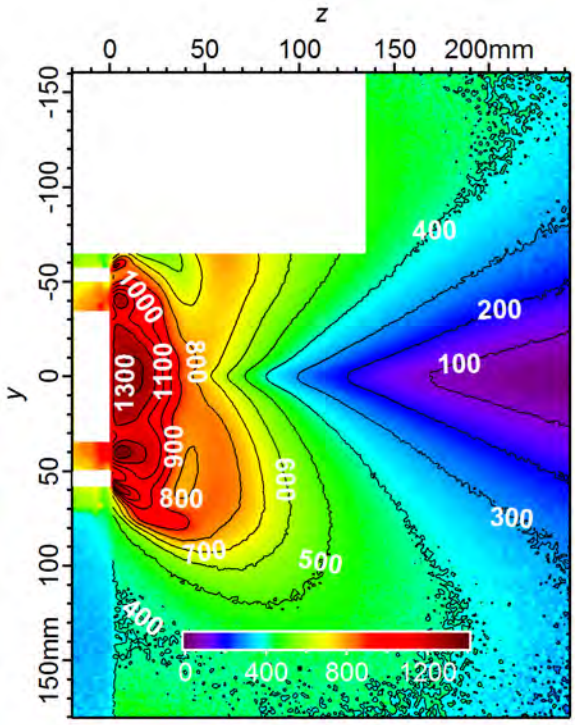

(c) Δ Radiance (%): $(R_{823:m+30\%} - R_{823:m-30\%})/R_{823:m-30\%} \times 100$

Figure 13. Ion emission radiance (823 nm) of the $\dot{m}$ =-30% operating condition and the $\dot{m}$ =+30% condition. Missing image portion is where optical shade blocked view of cathode.

IEPC-2015-416/ISTS-2015-b-416

An Investigation into the Spectral Imaging of Hall Thruster Plumes

M.R. Nakles
ERC, Inc.
Spacecraft Propulsion Branch
Edwards Air Force Base, CA

M.R. Holmes, W.A. Hargus, Jr.
Air Force Research Laboratory
Spacecraft Propulsion Branch
Edwards Air Force Base, CA

Introduction

- **Motivation**
  - Explore the possibility of using photography as a non-intrusive near-field optical diagnostic
  - Emission data can be compared to numerical simulations with collisional radiative models
- **Summary of Experimental Objectives**
  - Use a 16 bit camera with optical interference filters to image ion and neutral emission lines (542, 823 nm)
  - Examine how various operating conditions affect the near-field plume emission of the SPT-100
    - Subtract photos to view relative changes between operating conditions
  - Convert line-of-sight image data to radially dependent emission functions through Abel inversion

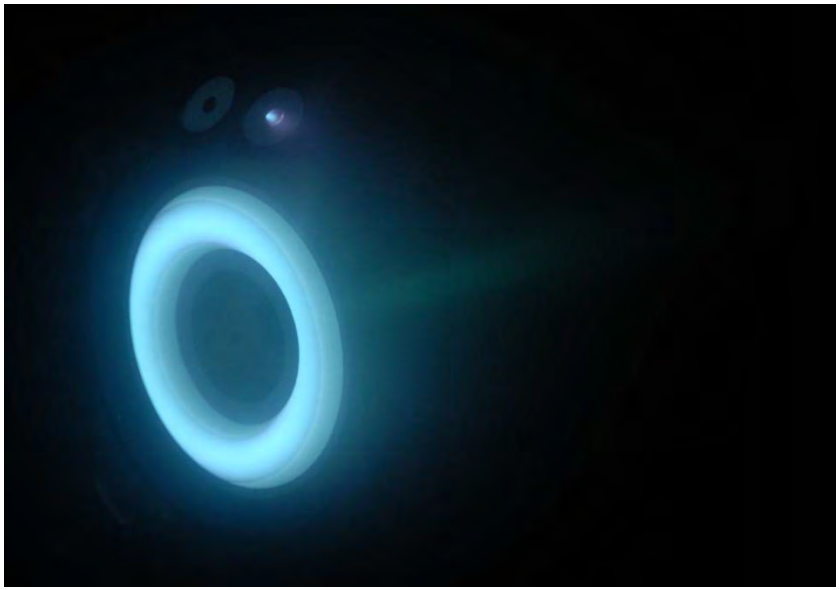

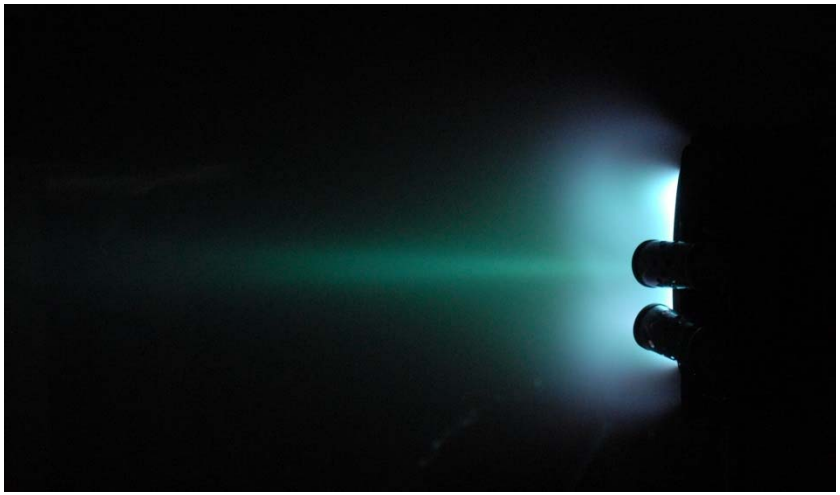

Testing Facility and Hall Thruster

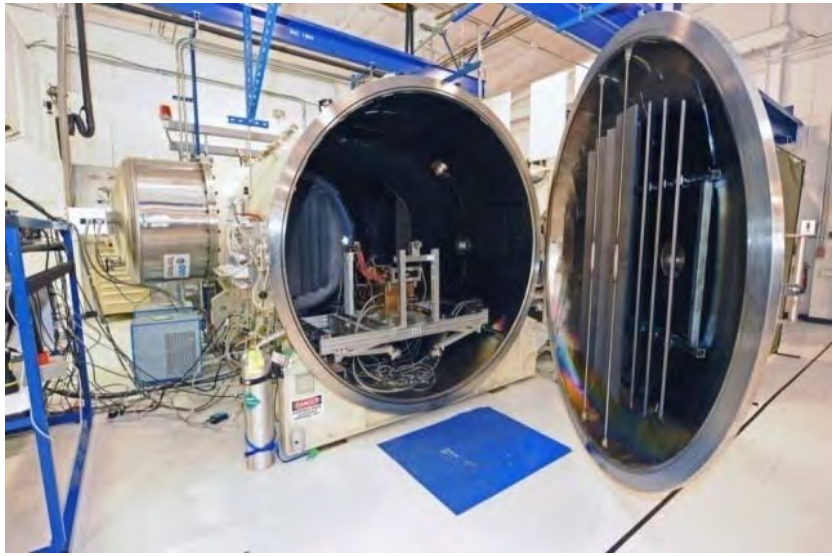

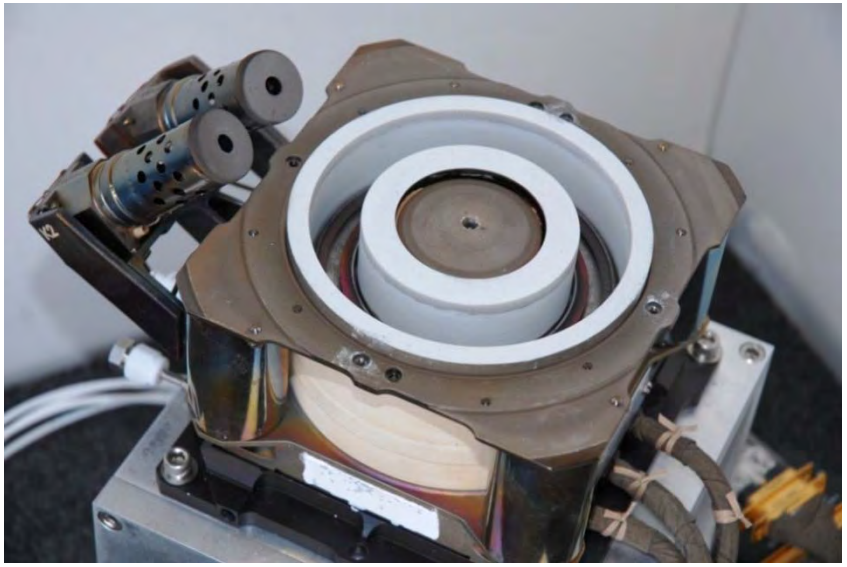

- **Chamber 1 AFRL Edwards AFB**
  - 2.4 m dia., 4.1 m length, stainless steel
  - Two cryogenic pumps
    - 1.2 m dia., LN2 baffled (70 K), 2 stage He (15 K)
    - SPT-100 nominal operation background pressure with Xe: 2.3×10^{-5} Torr (5.55 mg/s)

- **Flight Model SPT-100**
  - Nominal Anode Power: 1350 W
  - Conventional 5 magnetic core design
    - One inner, four outer connected in series
    - Magnetic circuit current supplied by anode current
  - Acceleration channel: 100 mm outer dia., 69 mm inner dia., 28 mm depth
  - 2 lanthanum hexaboride (LaB_6) cathodes

Optical Setup

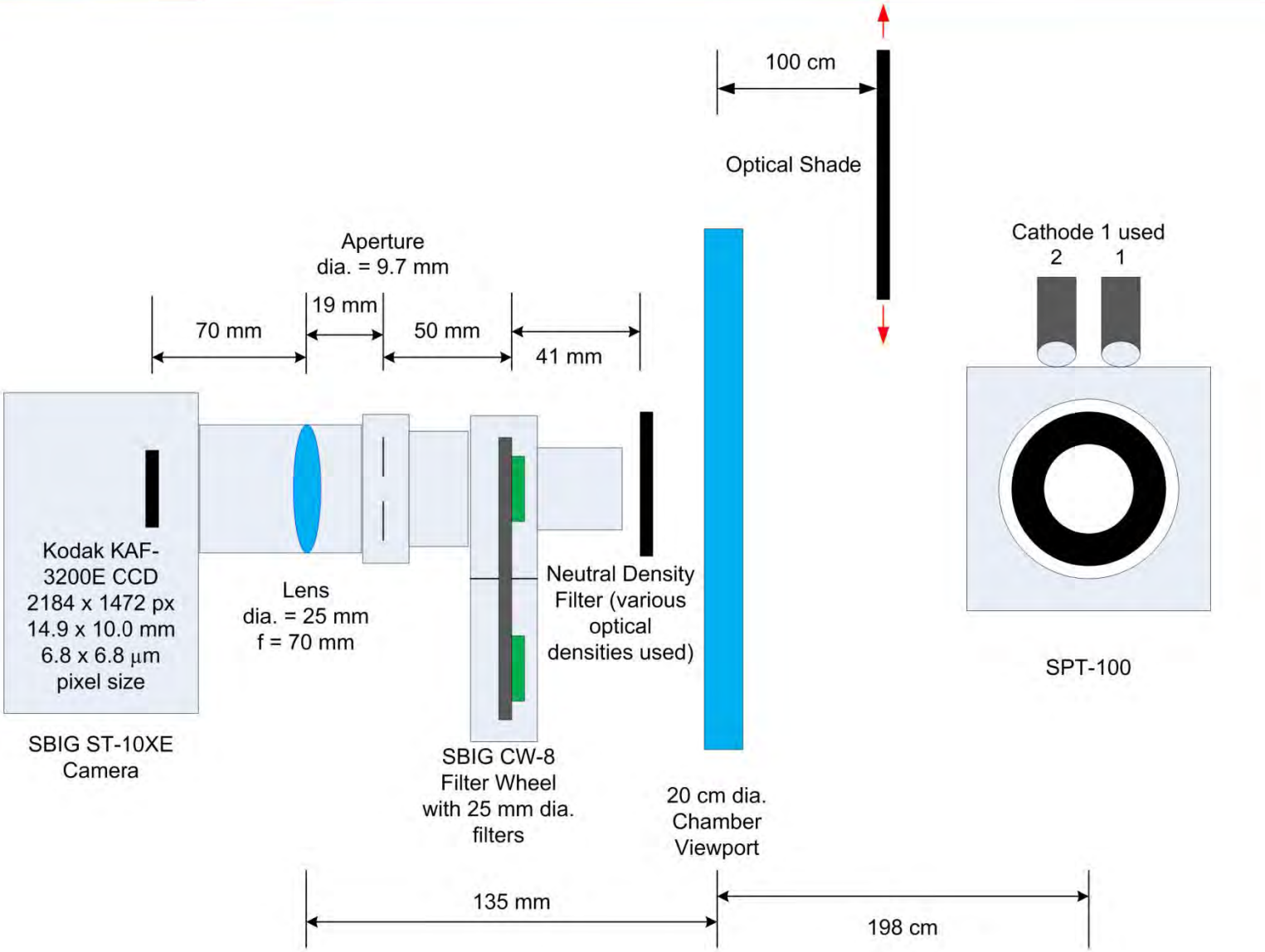

Optical Setup (Continued)

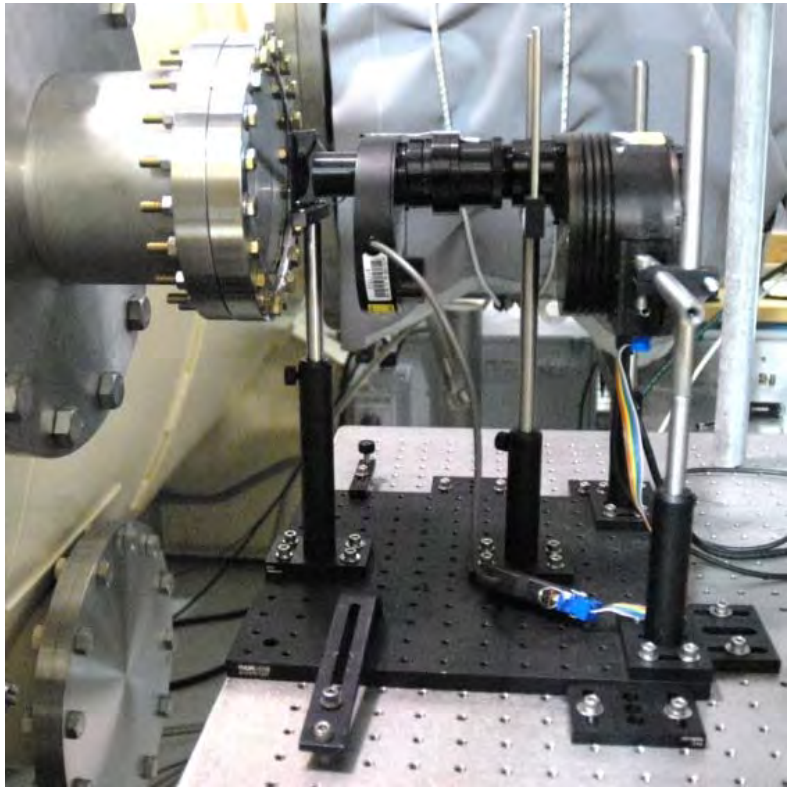

- **SBIG ST-10XE Camera**
  - 16 bit, 3 MP
  - f/7.2 optical setup
  - Covered with shroud during exposures

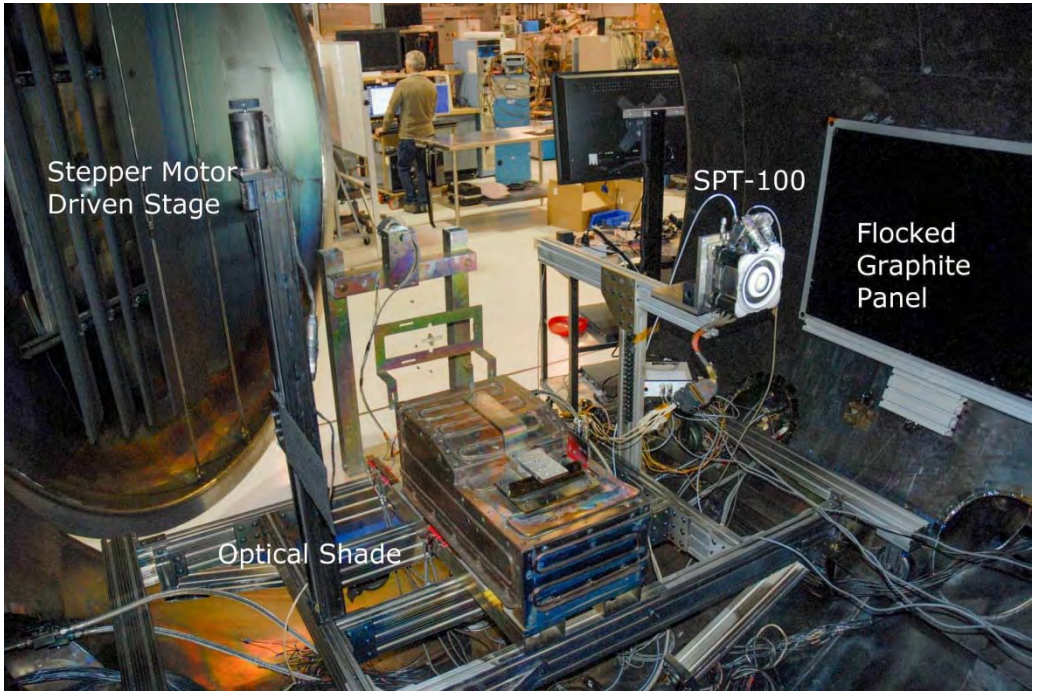

- **Chamber 1 Interior Setup**
  - Thruster mounted for profile view
  - Optical shade controlled with stepper motor driven stage
    - Blocks cathode and upstream plume
  - Non-reflective flocked graphite panel for background

Optical Interference Filters

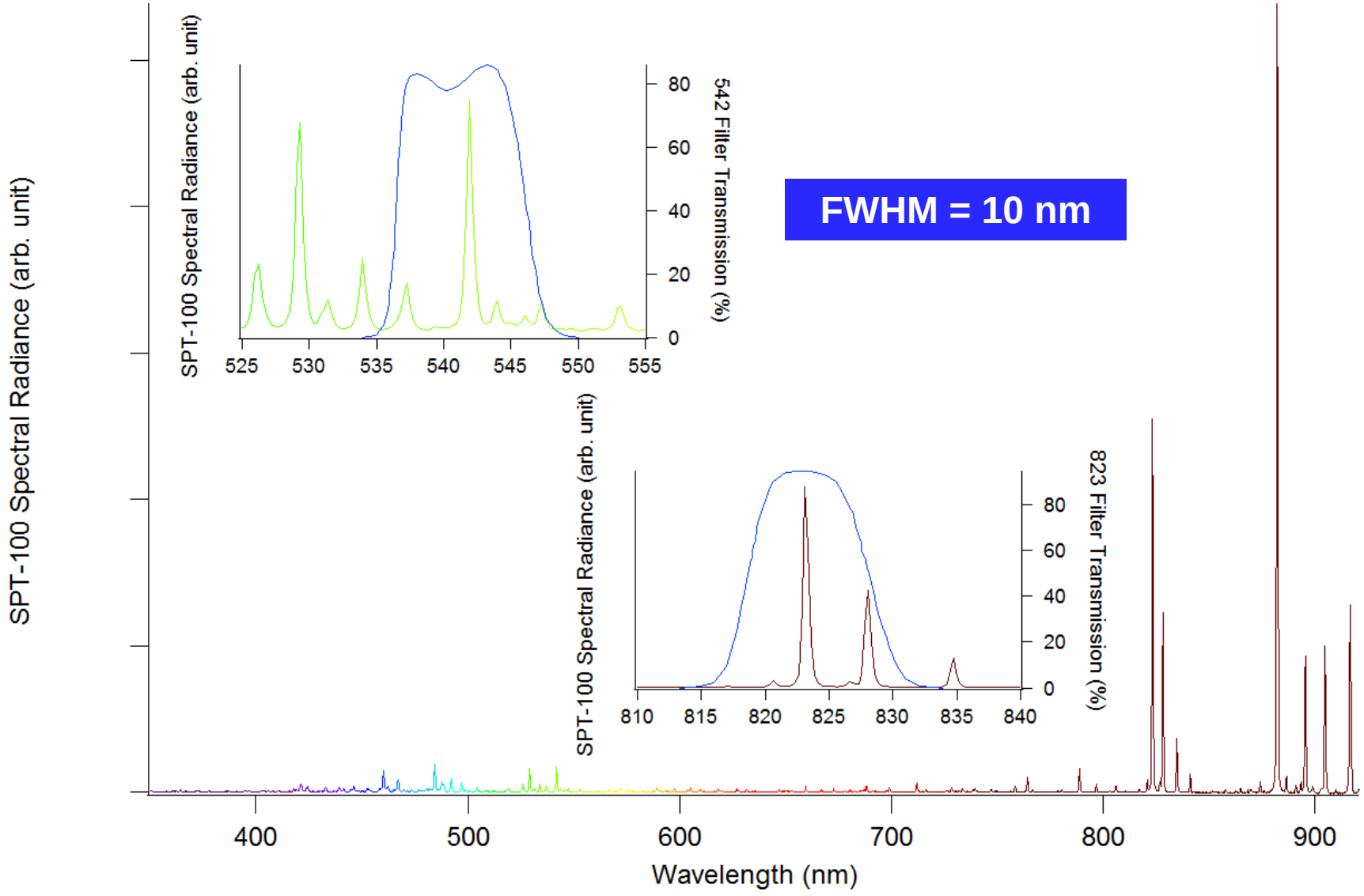

FWHM = 10 nm

Optical Techniques

- **Image Noise Reduction**
  - Average 10 exposures for each image
  - Subtract dark frame from image
  - Set camera's electronic chiller to 5° C
- **Flat-Field Correction**
  - Photograph uniformly illuminated surface
  - Divide images by flat-field images to correct for:
    - Vignetting (up to 60% brightness variation from center to corner in non-corrected images)
    - Non-uniform pixel response
    - Dust particles on CCD

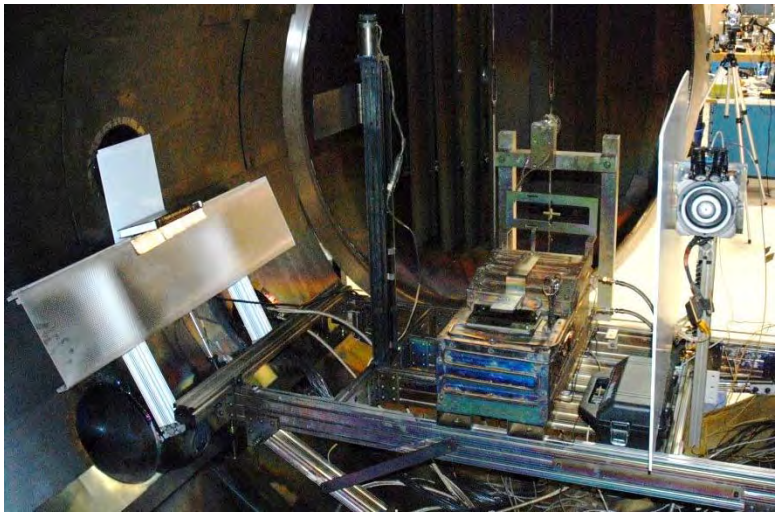

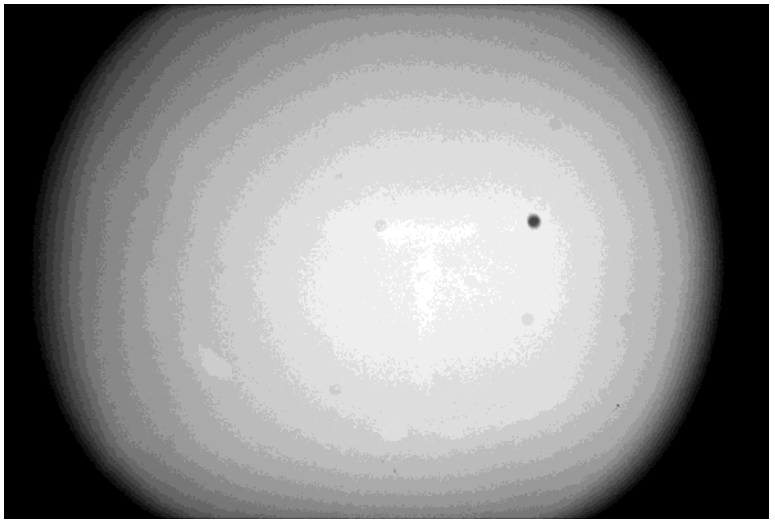

Relative Radiance Calibration

- Scale images through relative radiance calibration
  - Integrating sphere
  - Quartz tungsten lamp with NIST traceable irradiance curve
- Calculate f_λ and Q_{823} / Q_{542}
- Characterize pixel response to ensure exposures are within the linear regime

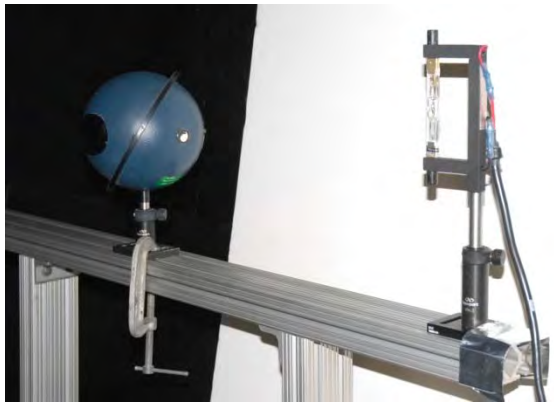

$$R = \frac{n}{f_\lambda Q_\lambda \frac{\lambda}{hc} A_{\text{pixel}} \frac{A_{\text{lens}}}{s'^2} \Delta t} = C \frac{n}{Q_\lambda \lambda \Delta t f_\lambda}$$

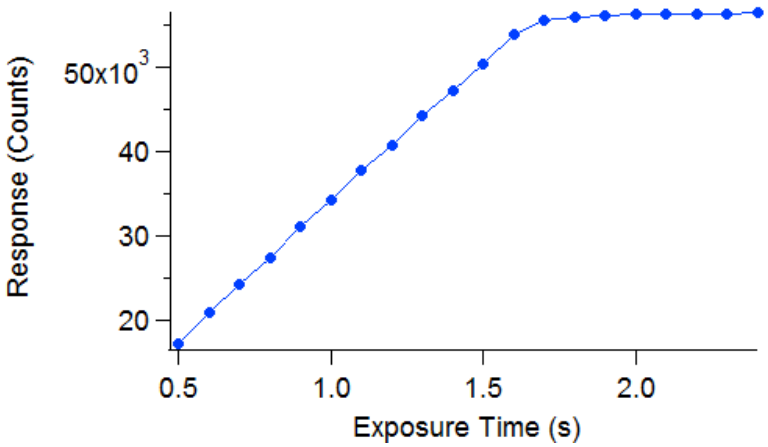

$$\frac{R_1}{R_2} = \frac{n_1}{n_2} \frac{Q_{\lambda 2}}{Q_{\lambda 1}} \frac{\lambda_2}{\lambda_1} \frac{\Delta t_2}{\Delta t_1} \frac{f_{\lambda 2}}{f_{\lambda 1}}$$

C = combined physical and geometrical constants
n = CCD count value
f_λ = fractional transmittance of ND filter at a given wavelength
Q_λ = CCD quantum efficiency at a given wavelength
Λ = wavelength
h = Planck constant
c = speed of light
A_{pixel} = area of CCD pixel
A_{lens} = area of lens
s' = distance between lens and CCD
Δt = exposure time

Abel Inversion Technique

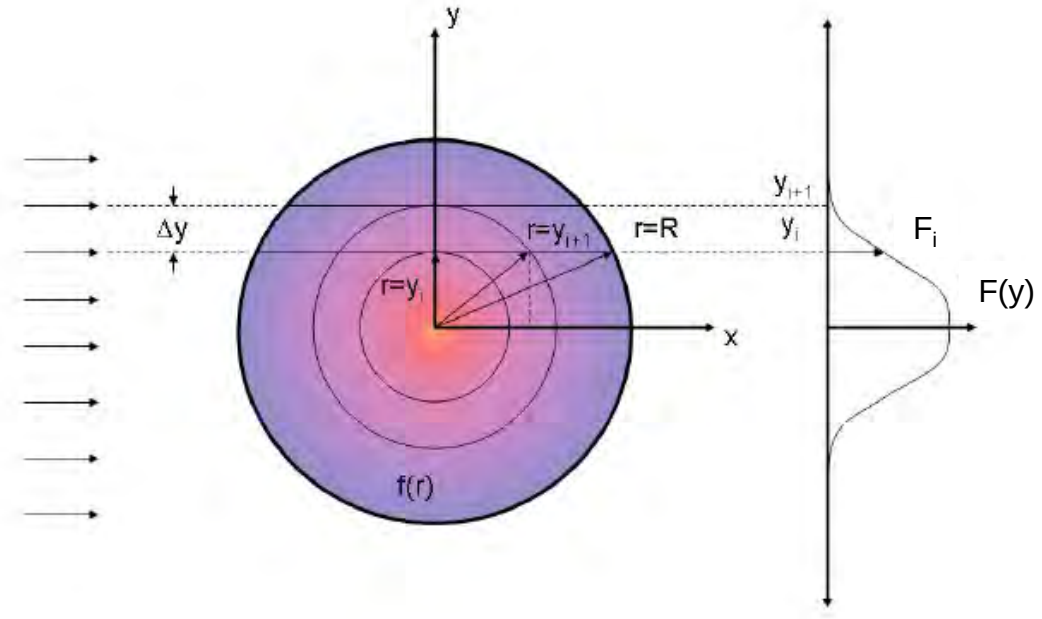

Forward Transform

$$F(y) = 2\int_y^R f(r)\frac{r}{\sqrt{r^2 - y^2}}dr$$

Inverse Transform

$$f(r) = -\frac{1}{\pi}\int_y^R \frac{dF(y)}{dy}\frac{dy}{\sqrt{y^2 - r^2}}$$

- Inverse Abel Transform is not practical to solve directly with numerical means
  - Singularity
  - Requires derivative of experimental data
- Use "Fourier Method"* to approximate *f(r)* as a cosine expansion

$$f(r) = \sum_{N_l}^{N_u} A_n f_n(r)$$

$$f_0(r) = 1,$$

$$\boldsymbol{f_n(r) = 1 - (-1)^n \cos\left(n\pi\frac{r}{R}\right)}$$

- Choose frequency limits to balance noise filtering and detail retention
- Least squares fit of forward transform with experimental data determines values of A_n

*Pretzier, G., Jger, H., Neger, T., Philipp, H., and Woisetschlger, J., "Comparison of Different Methods of Abel Inversion Using Computer Simulated and Experimental Side-On Data," *Zeitschrift fr Naturforschung*, Vol. 47a, 1992, pp. 955-970.

Thruster Operating Conditions

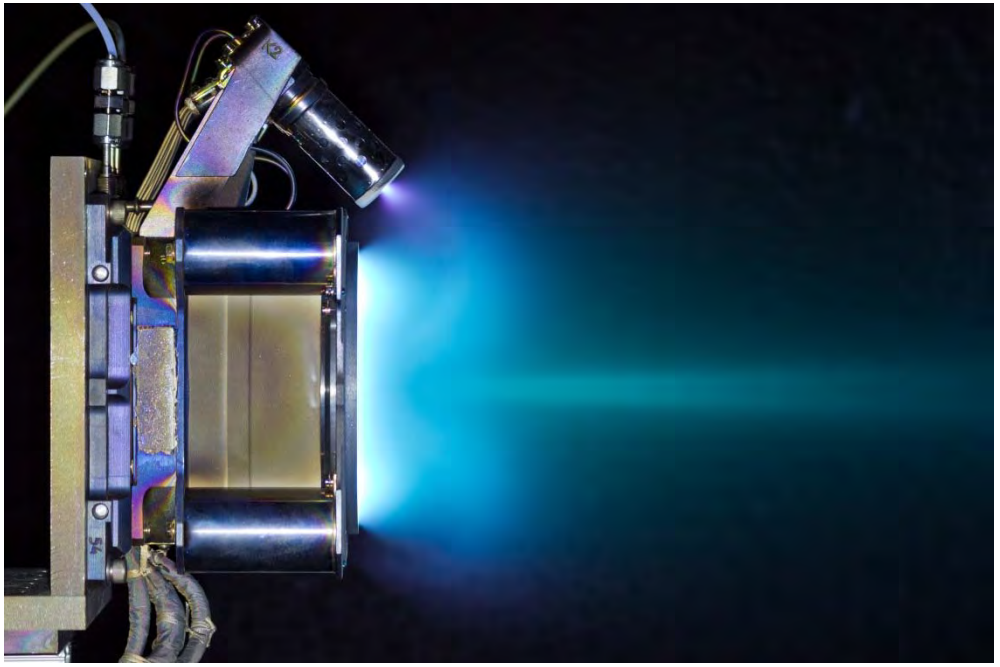

Operating Condition	V_d (V)	I_d (A)	Power (W)	$\dot{m}_a$ (mg/s)	$\dot{m}_c$ (mg/s)	$\dot{m}_b$ (mg/s)	P (Torr-Xe)	P (Pa-Xe)
Nominal	300	4.61	1383	5.15	0.40	0	2.28E-05	3.04E-03
High Back. Press.	300	4.57	1371	5.15	0.40	4.22	4.55E-05	6.07E-03
Low Dis. Voltage	210	4.60	966	5.15	0.40	0	2.09E-05	2.79E-03
High Dis. Voltage	390	4.56	1778	5.15	0.40	0	2.08E-05	2.78E-03
Low Prop. Flow Rate	300	2.90	870	3.60	0.28	0	1.52E-05	2.03E-03
High Prop. Flow Rate	300	5.99	1797	6.69	0.51	0	2.74E-05	3.66E-03

Comparison of Ion and Neutral Emission Radiance (arb. unit)

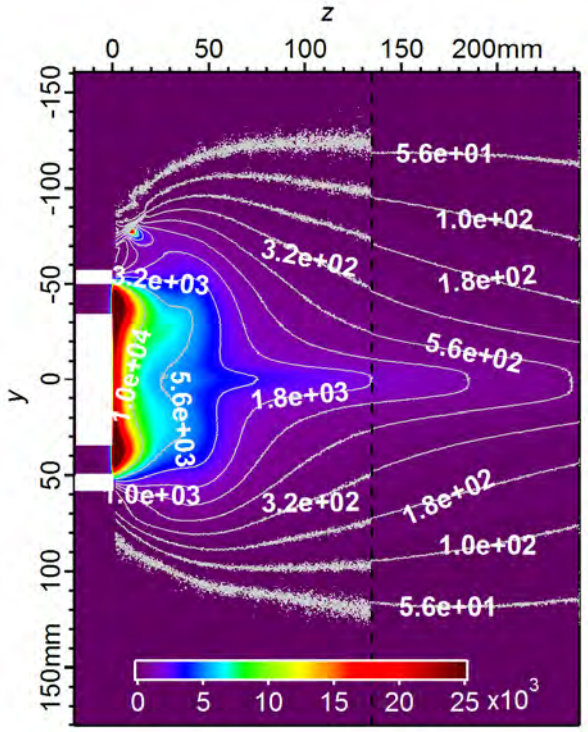

542 nm (ion)

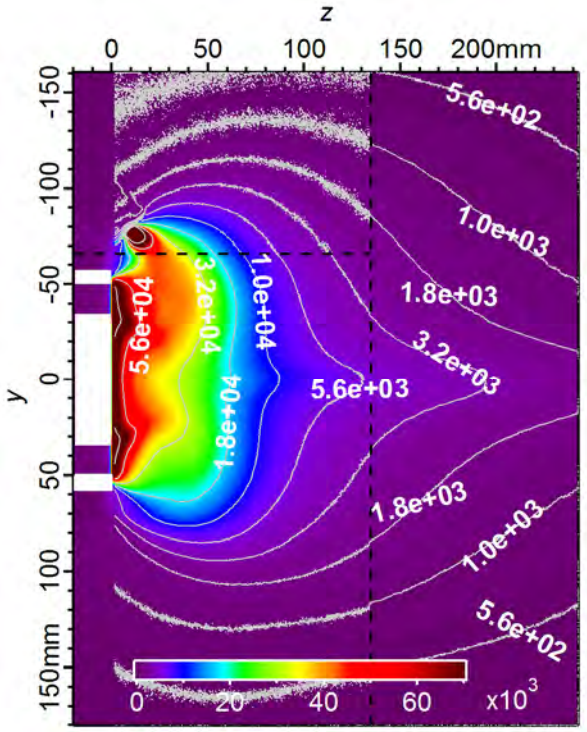

823 nm (neutral)

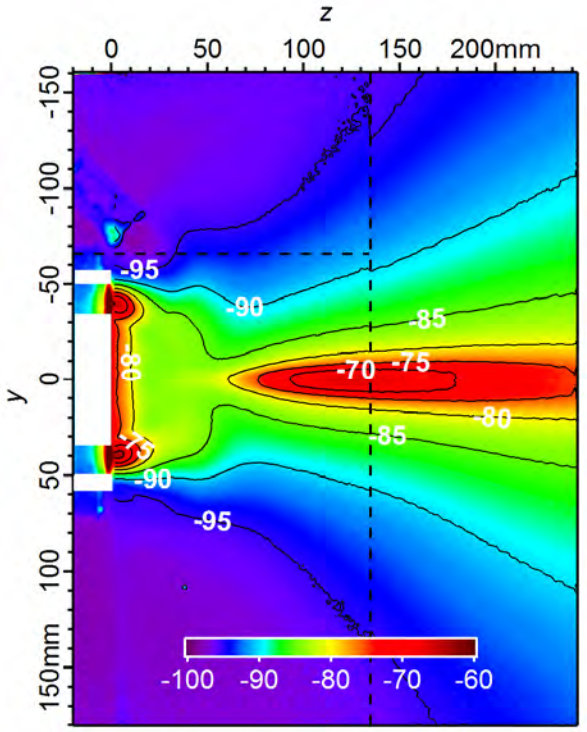

$$\Delta R(\%) = \frac{(R_{542:Nom} - R_{823:Nom})}{R_{823:Nom}} \times 100$$

- Neutral emission is greater than ion emission throughout plume, especially at the cathode (26× greater radiance)
- Highest regions of relative ion emission found at channel exits and central plume core, lowest regions outside of plume beam

542 nm (Ion) Emission Double BG Press. Radiance (arb. unit)

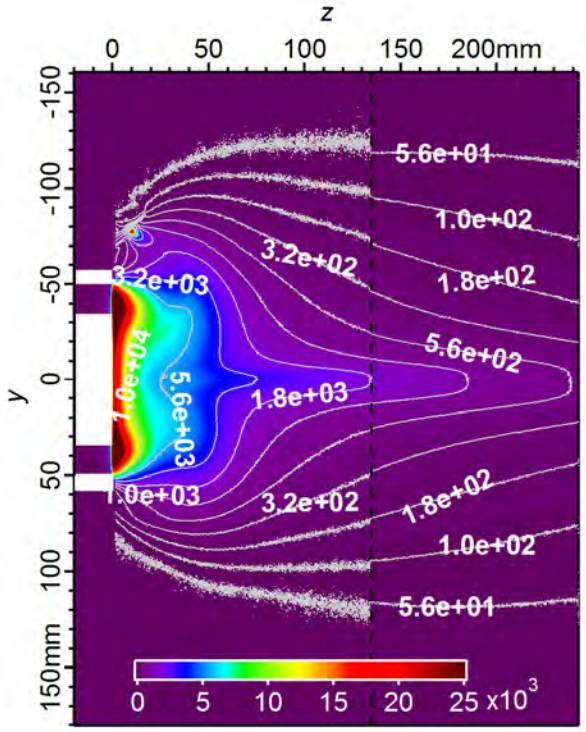

Nominal (P = 2.3e-5 Torr)

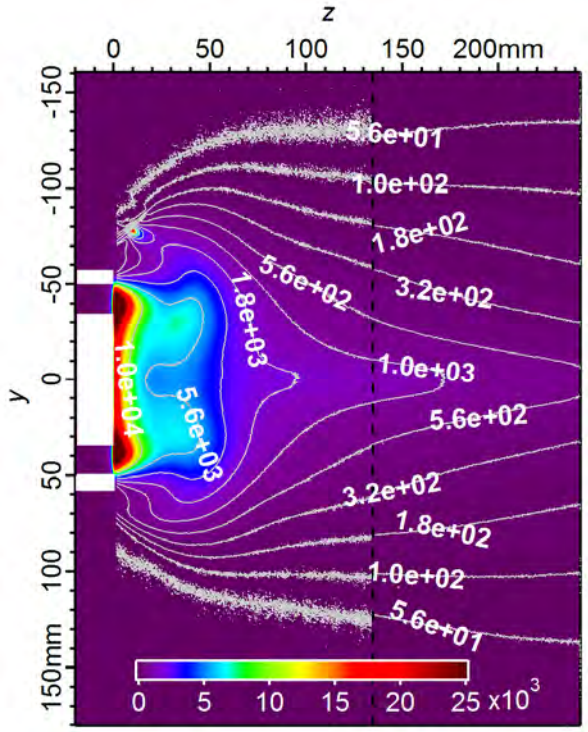

High Pressure (P = 4.6e-5 Torr)

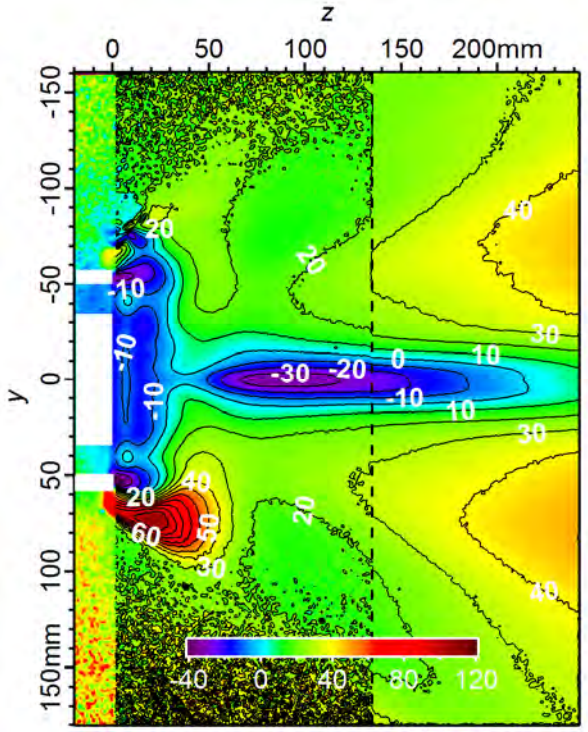

$$\Delta R(\%) = \frac{(R_{542:DP} - R_{542:Nom})}{R_{542:Nom}} \times 100$$

- Higher thrust measured as background pressure increases due mostly to less plume divergence*
- Asymmetrical region of high emission at *z* = 20, y = 75 mm
- Lower emission in plume core and near exit plane, higher elsewhere
  - Maybe less beamlet divergence from channel exits, from upstream shift of ion acceleration region
- Similar emission at channel exit.

*Diamant, K. D., Liang, R., and Corey, R. L., "The Effect of Background Pressure on SPT-100 Hall Thruster Performance," *Proceedings of the 50th AIAA/ASME/SAE/ASEE Joint Propulsion Conference*, 2014, AIAA-2014-3710.

823 nm (Neutral) Emission Double BG Press. Radiance (arb. unit)

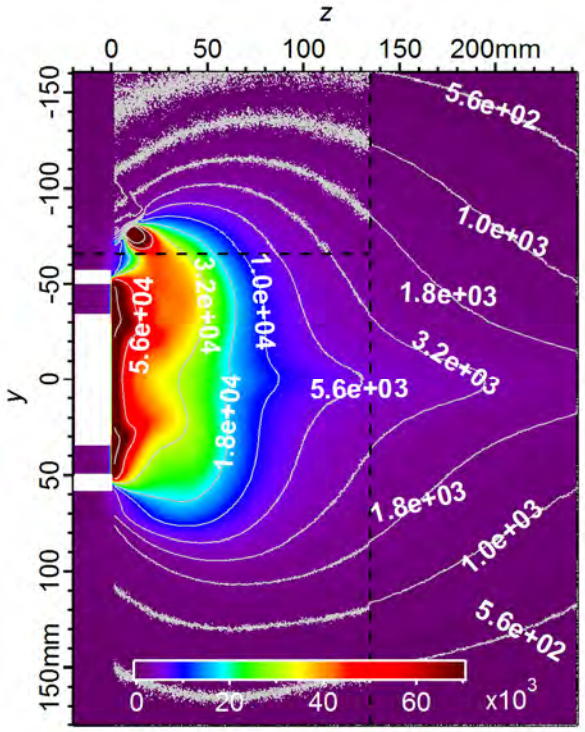

Nominal

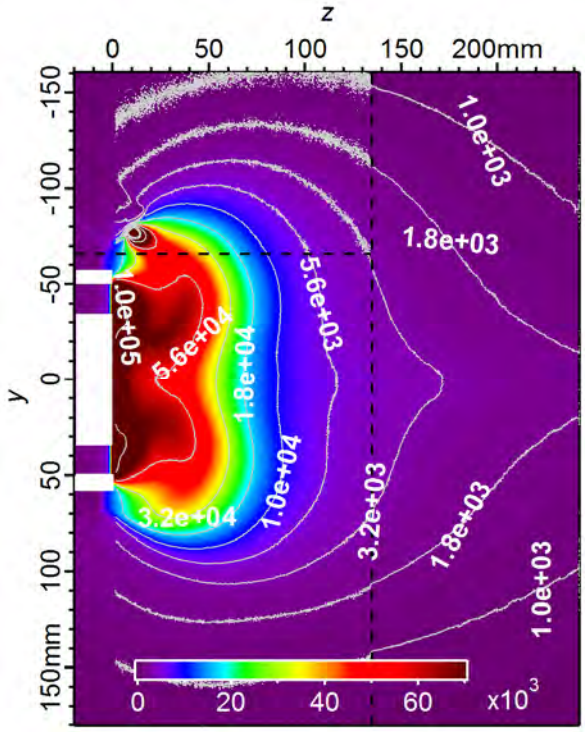

Double BG Pressure

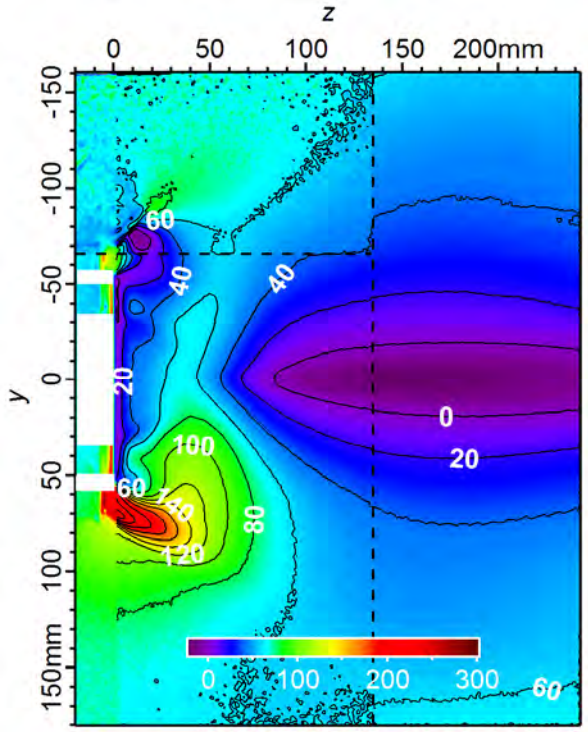

$$\Delta R(\%) = \frac{(R_{823:DP} - R_{823:Nom})}{R_{823:Nom}} \times 100$$

- Similar, but more intense asymmetrical region of high emission at z = 20, y = 75 mm as ion emission
- Broader low emission region in plume core beyond z = 50 mm

Radial Profiles: Double BG Press. vs. Nominal

542 nm (ion)

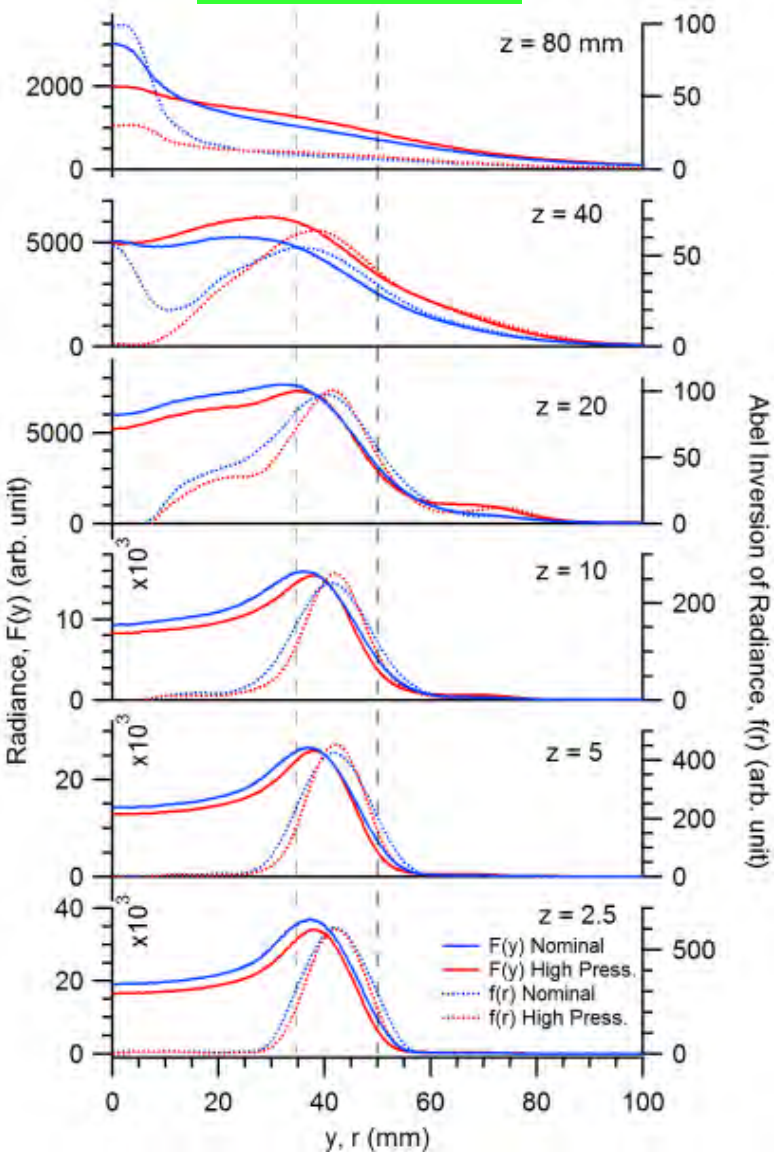

823 nm (neutral)

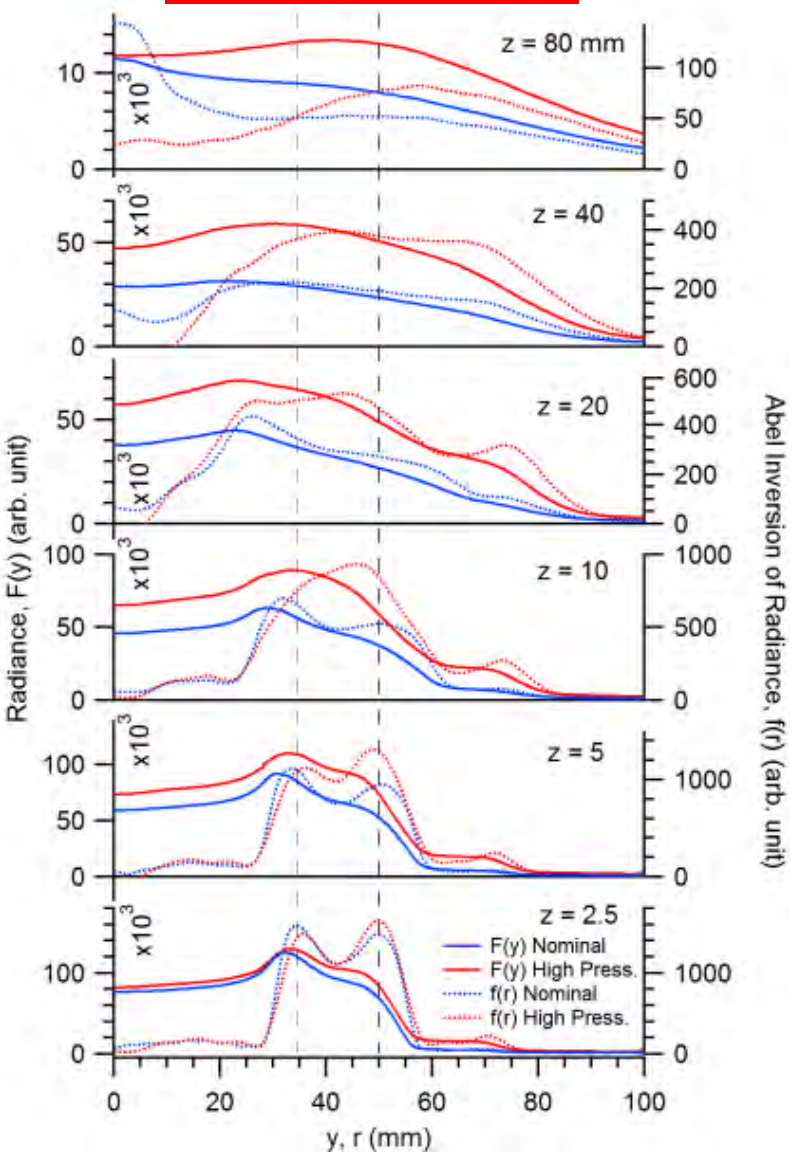

542 nm (Ion) Emission V_d Variations
Radiance (arb. unit)

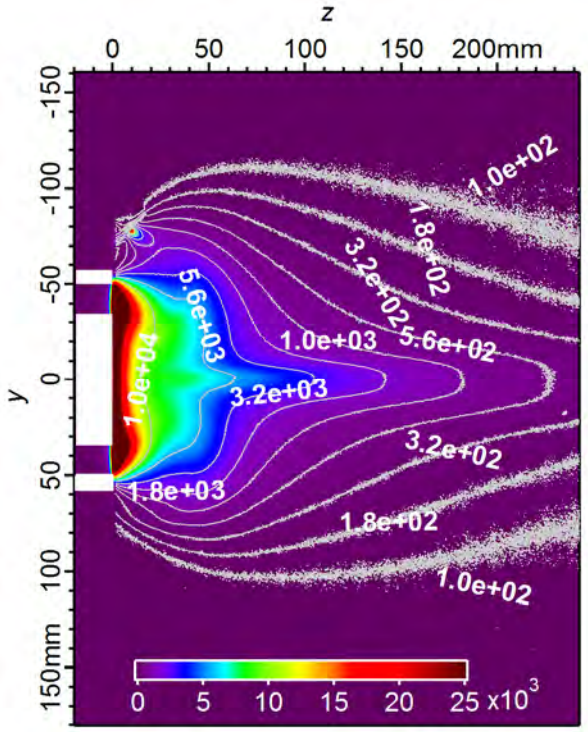

V_d = 210 V

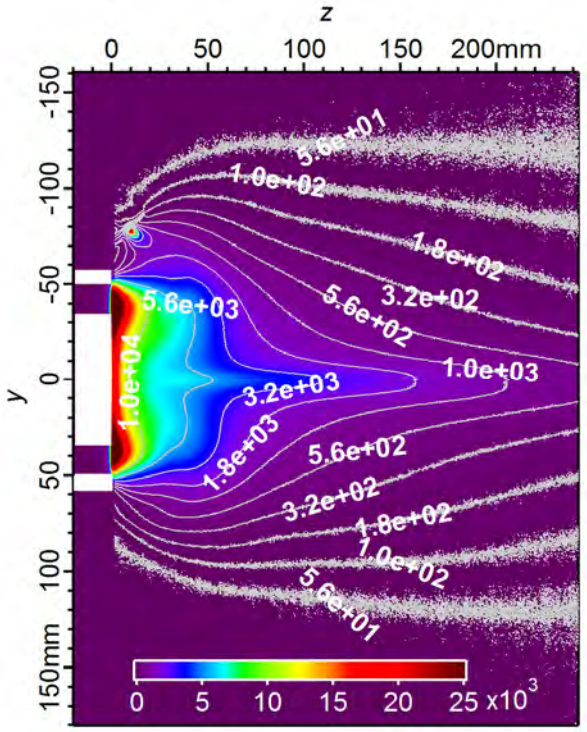

V_d = 390 V

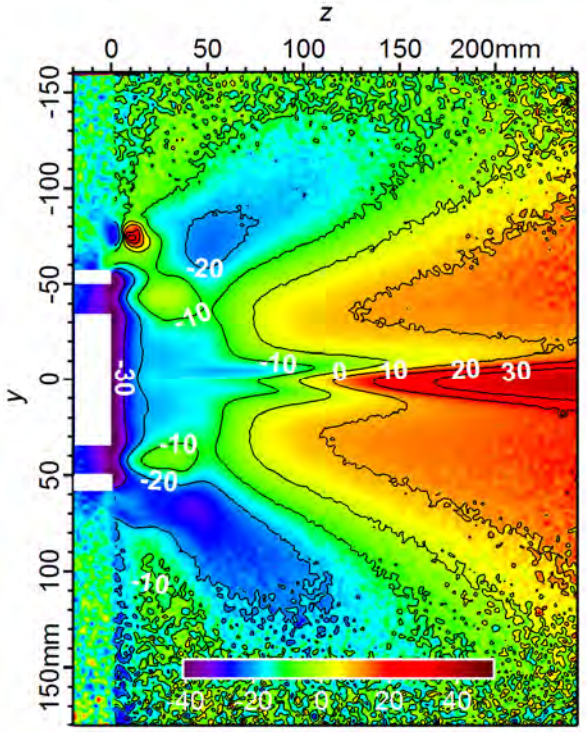

$$\Delta R(\%) = \frac{(R_{542:Vd390} - R_{542:Vd210})}{R_{542:Vd210}} \times 100$$

- Greater emission in plume beyond z = 100 mm, lower upstream
- Maybe beam interaction is occurring farther downstream with the faster ions

823 nm (Neutral) Emission V_d Variations
Radiance (arb. unit)

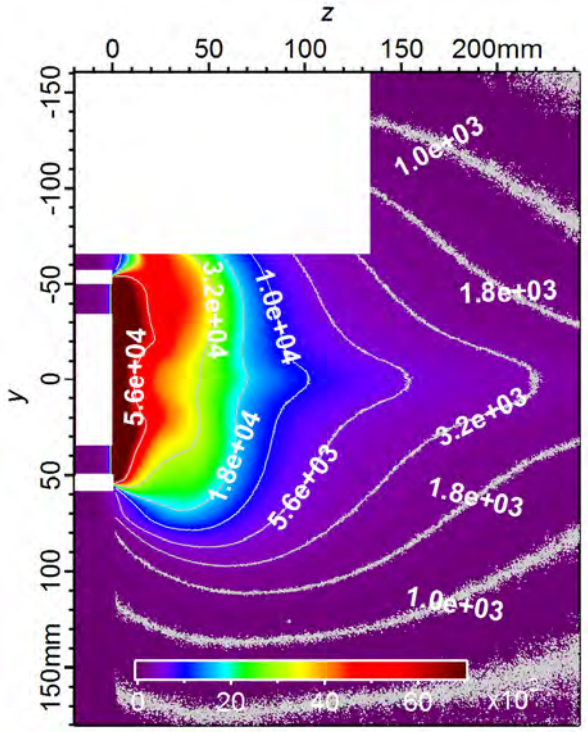

V_d = 210 V

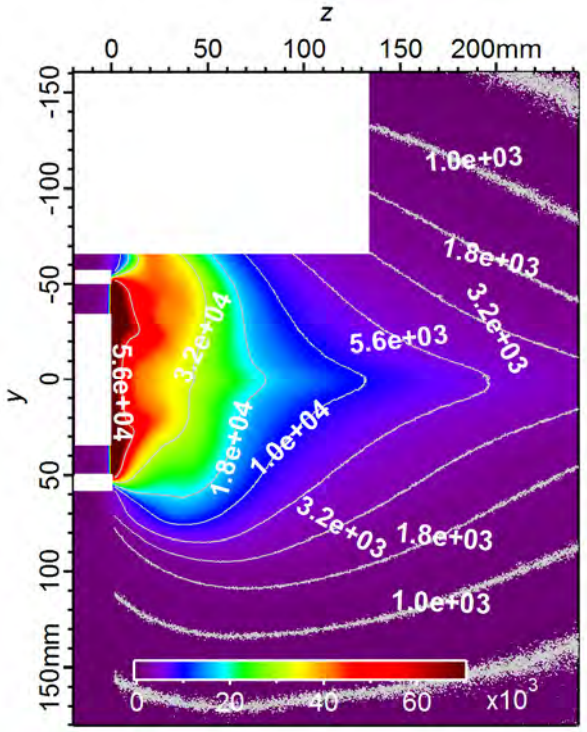

V_d = 390 V

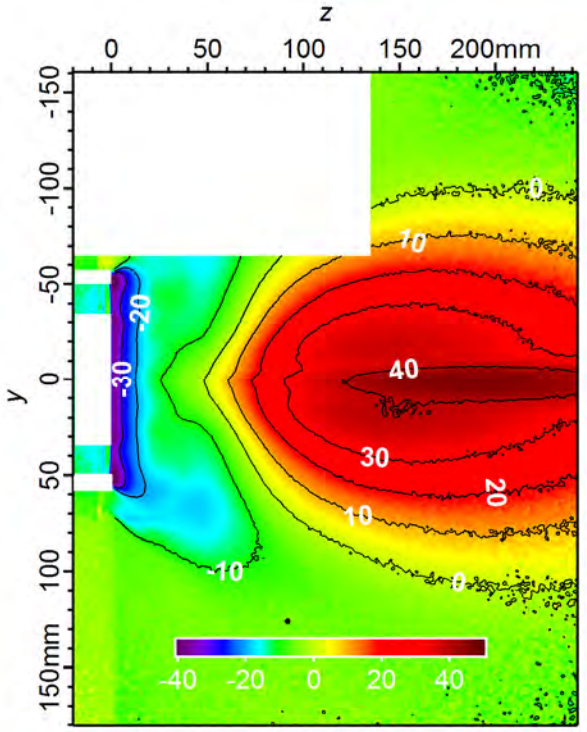

$$\Delta R(\%) = \frac{(R_{823:Vd390} - R_{823:Vd210})}{R_{823:Vd210}} \times 100$$

- Similar changes compared to ion emission, but with broader plume emission features

Radial Profiles: V_d = 210 V vs. V_d = 390 V

542 nm (ion)

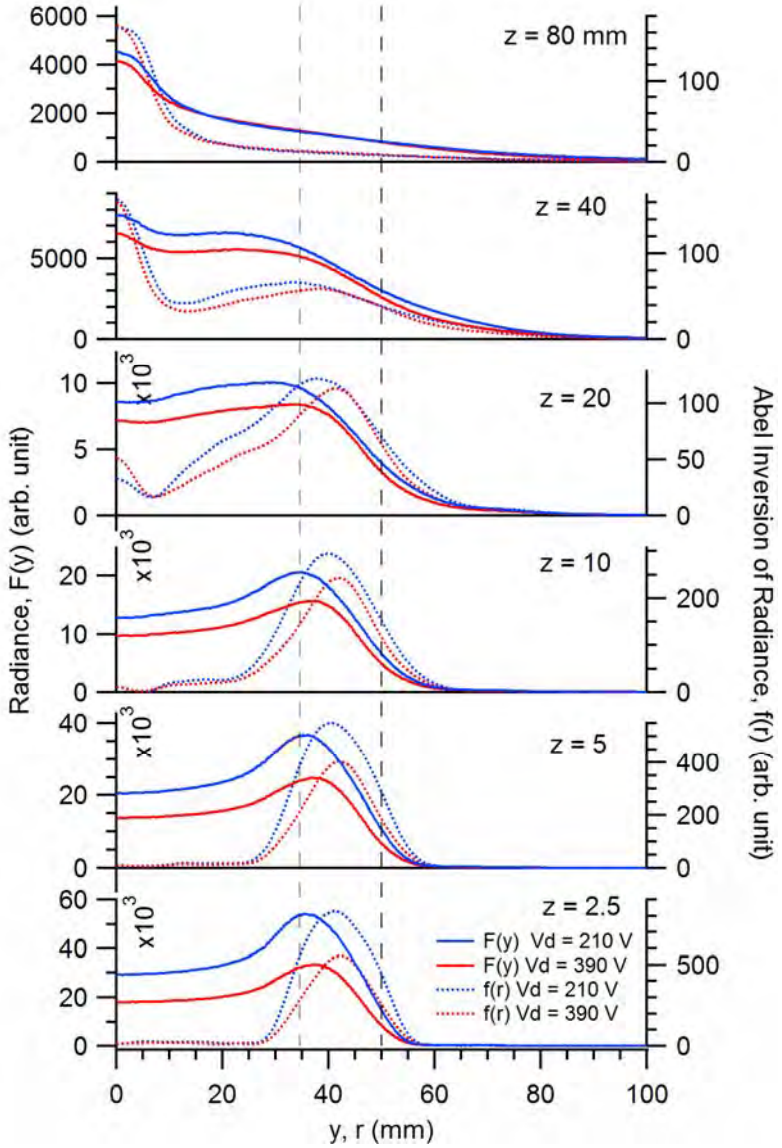

823 nm (neutral)

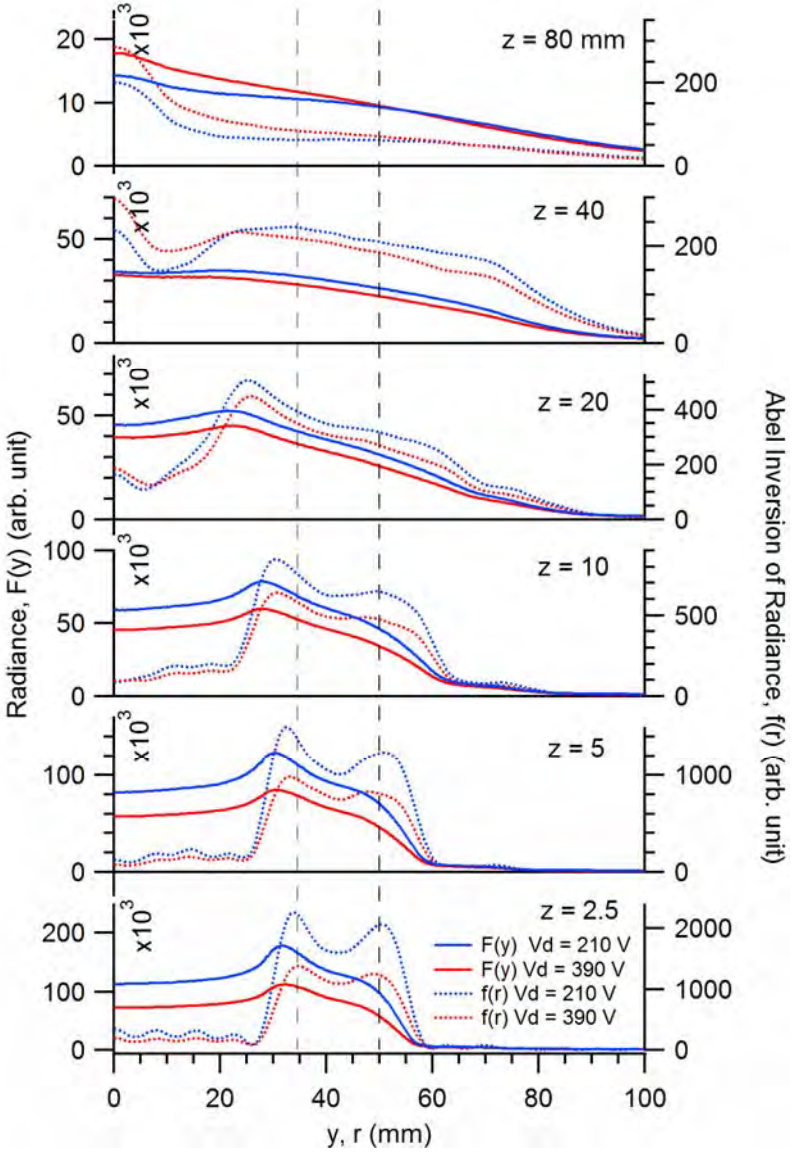

542 nm (Ion) Emission $\dot{m}$ Variations
Radiance (arb. unit)

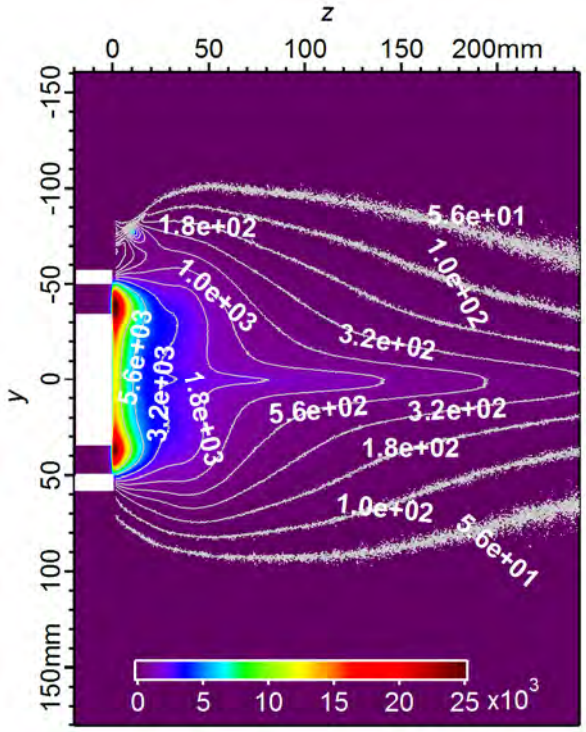

$\dot{m}$ = -30% ($\dot{m}$ = 3.88 mg/s)

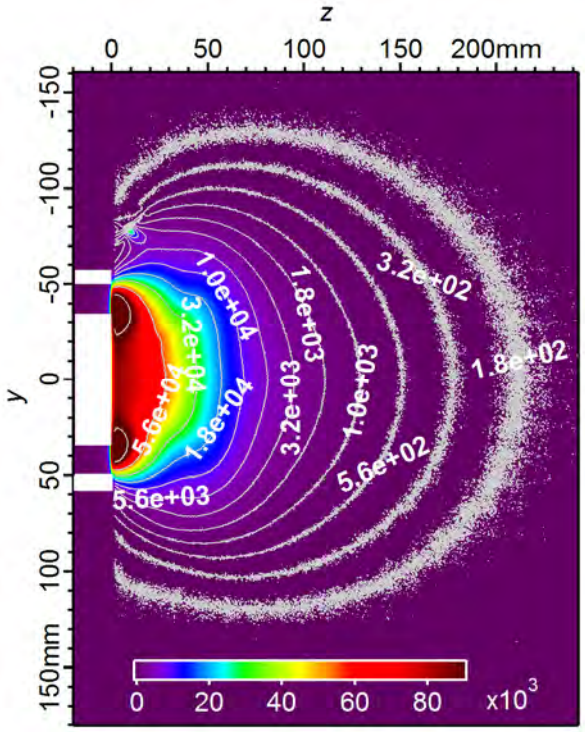

$\dot{m}$ = +30% ($\dot{m}$ = 7.20 mg/s)

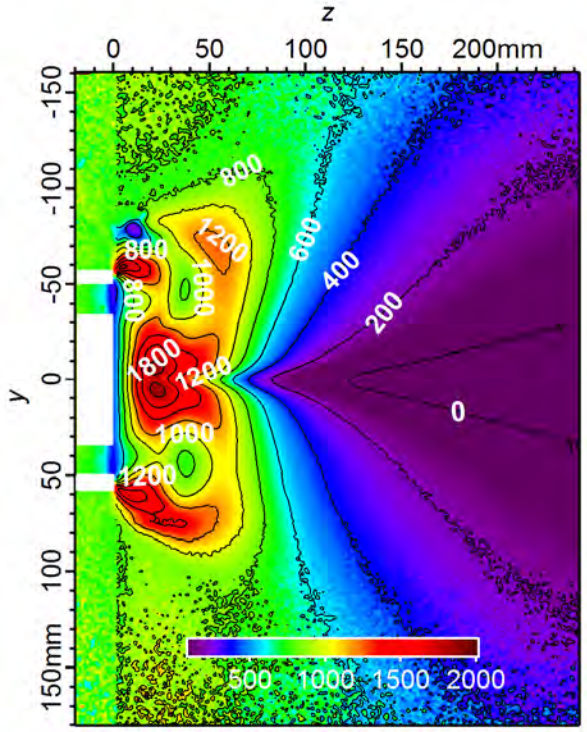

$$\Delta R(\%) = \frac{(R_{542:\dot{m}+30\%} - R_{542:\dot{m}-30\%})}{R_{542:\dot{m}-30\%}} \times 100$$

- Dramatic increase in emission for high propellant flow rate (note color scale change)
  - Highest increase directly downstream of center magnetic pole and outside of channel
  - More collisions with unionized propellant
- Spherical emission shape different from other cases
  - Scattering collisions diffusing plume

823 nm (Neutral) Emission $\dot{m}$ Variations
Radiance (arb. unit)

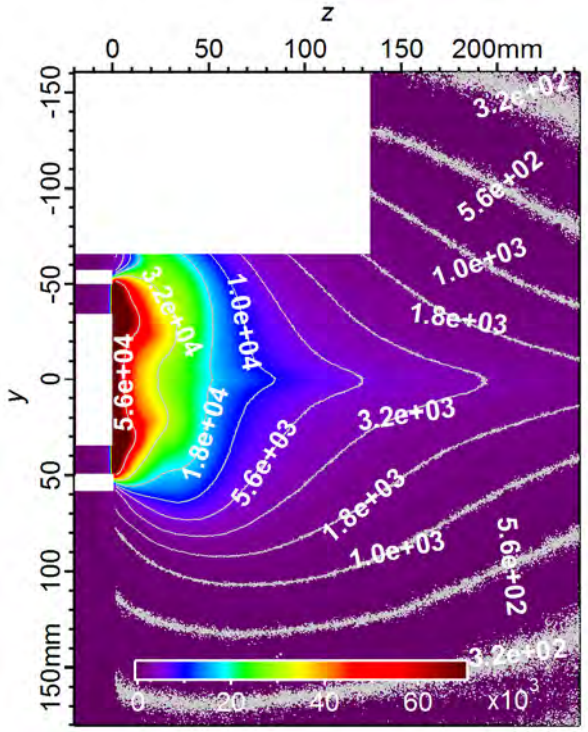

$\dot{m}$ = -30% ($\dot{m}$ = 3.88 mg/s)

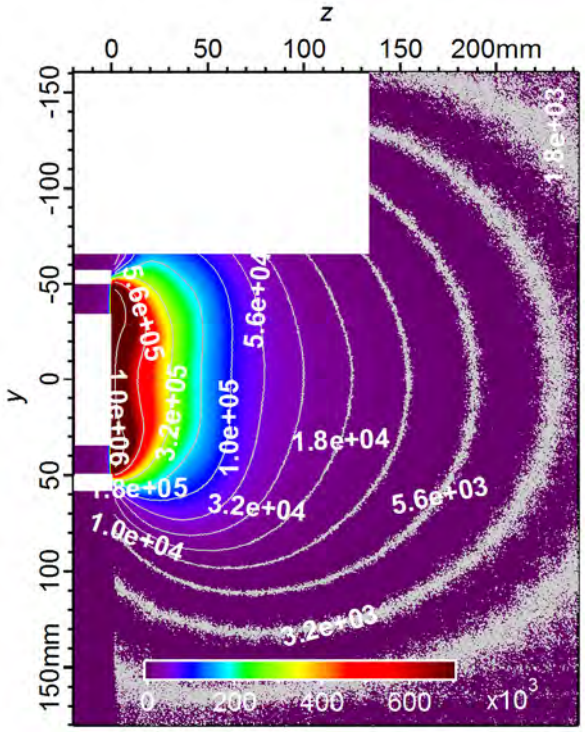

$\dot{m}$ = +30% ($\dot{m}$ = 7.20 mg/s)

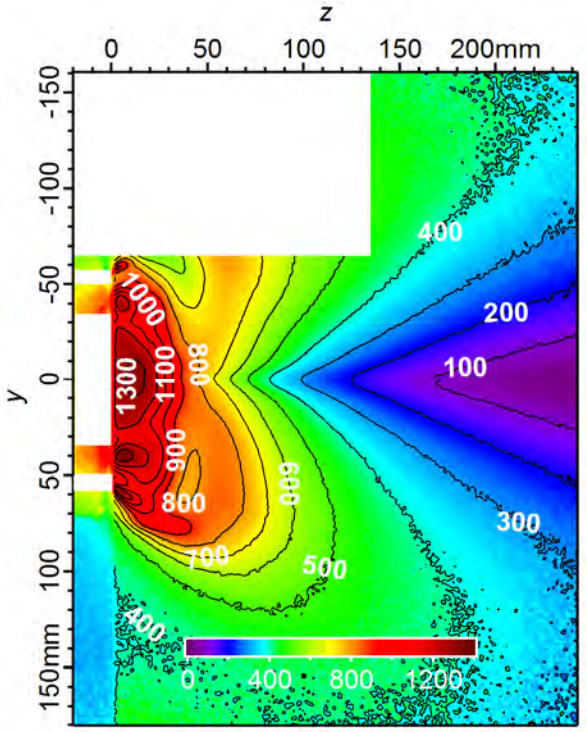

$$\Delta R(\%) = \frac{(R_{823:\dot{m}+30\%} - R_{823:\dot{m}-30\%})}{R_{823:\dot{m}-30\%}} \times 100$$

- Similar changes to plume emission shape as seen for 542 emission
  - High increase in emission directly downstream of channel exit

Conclusions and Future Work

- **Conclusions**
  - **Optical Technique**
    - High degree of repeatability
    - Exposures of separate regions of plume scaled well for composite image increasing dynamic range of data
    - Inverse Abel inversion analysis technique performed well overall
      - Resolved emission detail related to acceleration channel geometry
      - Similar neutral distribution shape across channel as seen in LIF density measurements SPT-140 near-field plume*
      - A few problem areas near $r = 0$ where $f(r) < 0$
  - **Plume Analysis**
    - Distinct changes in emission structure of plume observed for various operating conditions

- **Future Work**
  - ❑ **Model Comparison**
    - Perform measurements to match a numerical model of the near-field plume that includes CRM
    - Compare experimental and numerical results for model validation
    - Examine scaling of emission with density in numerical results to see if photographic density estimates are appropriate
  - ❑ **Probe Comparison**
    - Directly measure density and/or temperature with a probe in the near-field
    - Compare results with emission data to see if density can be estimated from emission where temperature gradients are adequately low
    - Photograph probe in plume to examine the perturbation as function of emission
  - ❑ **Apply experimental technique with high speed camera to study breathing mode**

*Crofton, M. et al., "Neutral Density in the SPT-140 Near-Field Plume," *Proceedings of the 33rd International Electric Propulsion Conference*, 2013, IEPC-2013-399.

Abel Inversion Technique Equations

Forward Abel Inversion

$$h(y) = 2 \int_y^R f(r) \frac{r}{\sqrt{r^2 - y^2}} \, \mathrm{d}r$$

Inverse Abel Inversion

$$f(r) = -\frac{1}{\pi} \int_y^R \frac{\mathrm{d}h(y)}{\mathrm{d}y} \cdot \frac{\mathrm{d}y}{\sqrt{y^2 - r^2}}$$

Approximate *f(r)* as cosine func. expansion

$$f(r) = \sum_{n=N_l}^{N_u} A_n f_n(r)$$

$$f_0(r) = 1 \,,$$

$$f_n(r) = 1 - (-1)^n \cos\left(n \pi \frac{r}{R}\right)$$

Forward Abel Inversion becomes

$$H(y) = 2 \sum_{n=N_l}^{N_u} A_n \int_y^R f_n(r) \frac{r \, \mathrm{d}r}{\sqrt{r^2 - y^2}}$$

Set each integral term numerically

$$h_n(y) = \int_y^R f_n(r) \frac{r \, \mathrm{d}r}{\sqrt{r^2 - y^2}}$$

Perform least squares fit to fit amplitude values A_n

$$2 \sum_{n=N_l}^{N_u} \left(A_n \sum_{k=1}^{N} h_n(y_k) \, h_m(y_k) \right) = \sum_{k=1}^{N} h(y_k) \, h_m(y_k),$$

$$\forall m: \; N_l \le m \le N_u$$

$$\sum_{k=1}^{N} [H(y_k) - h(y_k)]^2 \stackrel{!}{=} \text{Min}$$

*Pretzier, G., Jger, H., Neger, T., Philipp, H., and Woisetschlger, J., “Comparison of Different Methods of Abel Inversion Using Computer Simulated and Experimental Side-On Data," *Zeitschrift fr Naturforschung*, Vol. 47a, 1992, pp. 955-970.

An Investigation into the Spectral Imaging of Hall Thruster Plumes

IEPC-2015-416/ISTS-2015-b-416

Presented at Joint Conference of 30th International Symposium on Space Technology and Science, 34th International Electric Propulsion Conference and 6th Nano-satellite Symposium
Hyogo-Kobe, Japan
July 4–10, 2015

Michael R. Nakles*
ERC, Inc., Edwards Air Force Base, CA, 93524

Michael R. Holmes†and William A. Hargus, Jr.‡
Air Force Research Laboratory, Edwards Air Force Base, CA, 93524

An exploratory investigation of measuring xenon spectral emission lines in a Hall thruster plume through optical imaging techniques was performed on the SPT-100 Hall thruster. A 16 bit CCD camera was used with optical interference bandwidth filters to separately photograph neutral (823 nm) and ion (542 nm) xenon emission. The resulting images allowed for examination of the near-plume structure in terms of excited ions and neutral particles for various thruster operating conditions. Abel inversion analysis was applied to the photographs to examine the emission as a function of radius with the assumption of axial symmetry and an optically thin plasma. This experimental technique may provide results useful for comparison with numerical near-plume predictions that incorporate collisional radiative models.

Nomenclature

C	constant that accounts for optical geometry parameters and physical constants in optical calibrations
I_d	anode discharge current
f_i	fractional transmittance of neutral density filter
$\dot{m}_a$	anode propellant mass flow rate
$\dot{m}_b$	mass flow rate of additional background gas
$\dot{m}_c$	cathode propellant mass flow rate
n	CCD count value
P	vacuum chamber pressure
Q	quantum efficiency of CCD
r	radial coordinate about thrust axis
R	radiance
V_d	anode discharge voltage
x	axis in thruster coordinate system perpendicular to the cathode plane
y	axis in thruster coordinate system in the cathode plane
z	axis in thruster coordinate system in thrust direction
Δt	image exposure time
λ	wavelength

*Research Engineer, ERC, Inc., 1 Ara Rd. Edwards AFB, CA 93524
†Research Scientist, AFRL/RQRS, 1 Ara Rd. Edwards AFB, CA 93524
‡Research Engineer, AFRL/RQRS, 1 Ara Rd. Edwards AFB, CA 93524

Introduction

Hall effect thruster plumes present a challenging environment for the implementation plasma diagnostics. The near-plume region is an especially difficult region to characterize where changes in density and temperature occur over short distances. Here, the physical presence of probes is likely to perturb the plasma, affect thruster operation, cause heating effects, and lead to physical degradation of the probe itself. Even sizing a probe small enough for good spatial resolution can be difficult. Optical diagnostics such as laser-induced fluorescence[1] and microwave interferometry[2] are not encumbered by these limitations and have proven useful for reliable near-plume measurements.

The idea of using photography for certain types of plasma characterization is intriguing for its potential advantages. Images provide data in a virtually continuous fashion over a wide measurement domain, whereas most other diagnostics typically measure at one physical location at a time and must be physically moved to create a set of discrete data. The location of the camera outside of the chamber avoids physical disruption of the plasma and allows convenient access for the operator. Photographic images have been used to visually inspect basic changes in plume structure for different thruster operating modes.[3,4] Modern high-speed cameras can record images on timescales that allow the study of plasma oscillation modes in discharge channels.[3,5] Photography with optical filters has been used to image xenon ion and neutral emission separately in an ATON A53 Hall thruster.[6] This data was transformed from line-of-sight data into cross-sectional images of the plume for two operational modes through an inverse Abel transformation.

In this study, a 16 bit camera with optical interference bandwidth filters was used to examine the plasma structure of the near-plume of the SPT-100 in terms of optical emission of the 542 nm xenon ion line and the 823 nm xenon neutral line for various operating conditions. Optical emission is a function of both plasma density and temperature and can be predicted by collisional radiative models. The goal of this study was to examine the structure of the near-plume of the SPT-100 thruster at various operating conditions and to explore the use of Abel inversion analysis to deconvolve the image line-of-sight data into a radially dependent function with the assumption of axially symmetry and an optically thin plasma. The results of this experimental imaging may provide a useful comparison tool for numerical simulations of the near-plume region that incorporate collisional radiative models.

Experimental Apparatus and Techniques

Hall Effect Thruster

A flight model SPT-100 Hall effect thruster (Fig. 1) was used in this study. The axisymmetric thruster is equipped with two lanthanum hexaboride (LaB_6) cathodes (only one was used during these tests). This thruster has a conventional five magnetic core (one inner, four outer) magnetic circuit. Discharge current is routed through the magnetic circuit and thus no extra power source for the magnets is required. The acceleration channel of the thruster has a 100 mm outer diameter, a 69 mm inner diameter, and a channel depth of 25 mm. For its nominal xenon operating condition, the thruster has been characterized to have a thrust of 83 mN with a specific impulse of 1,600 s, yielding an anode efficiency near 50%.[7]

For this study, the thruster and cathode were powered with commercial off-the-shelf Sorenson power supplies instead of the PPU used on-orbit. A computer data acquisition system recorded the potential and current outputs of the power supplies used in the thruster operation at a rate of 2 Hz. For propellant flow, digital mass flow controllers from Aera dispersed gas to the anode and cathode taking the place of the xenon flow control system (XFC) used on-orbit. Therefore, propellant flow rate was constant for each given operating condition and not controlled by discharge current feedback as with an XFC system.

Test Facility

This study utilized Chamber 1 (Fig. 2(a)) at the Air Force Research Laboratory at Edwards Air Force Base. Chamber 1 is a cylindrical non-magnetic stainless steel vacuum chamber 2.4 m in diameter and 4.1 m in length. Pumping is provided by two liquid nitrogen baffled (70 K), 1.2 m flanged gaseous helium two stage cryogenic (15 K) vacuum pumps with a measured pumping speed on xenon of 48,500 L/s. Chamber pressure is monitored with a hot filament ionization gauge.

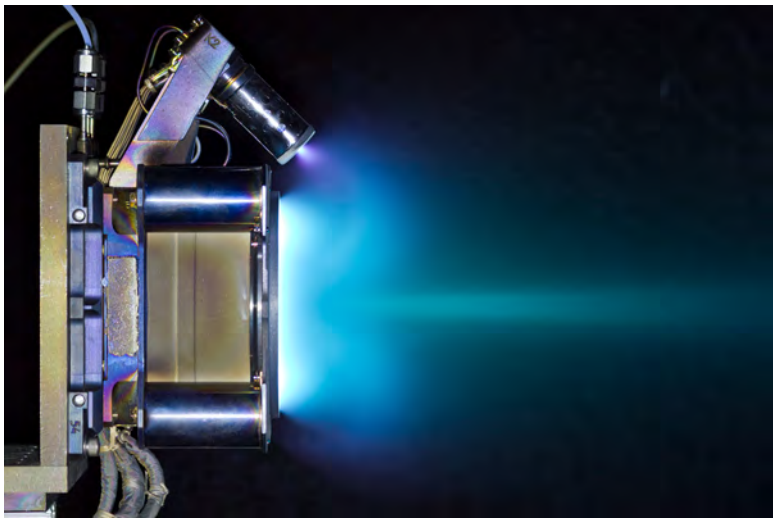

Figure 1. The SPT-100 firing in Chamber 1 photographed by a digital SLR from the same perspective as the scientific images presented in this study.

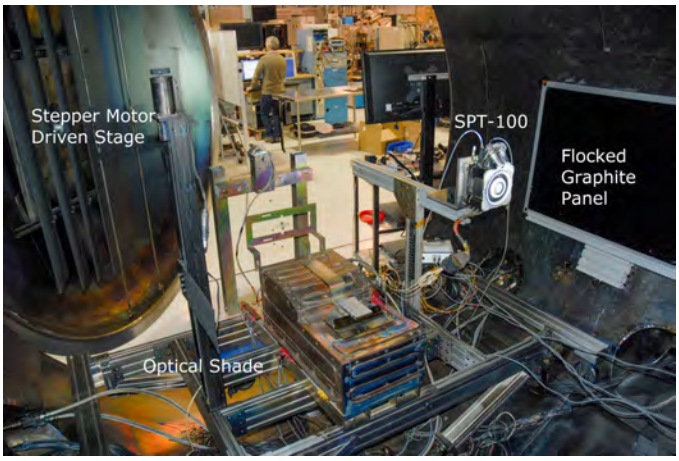

(a) The SPT-100 installed in Chamber 1 for the optical imaging. The optical viewport for imaging is beyond the left photo border.

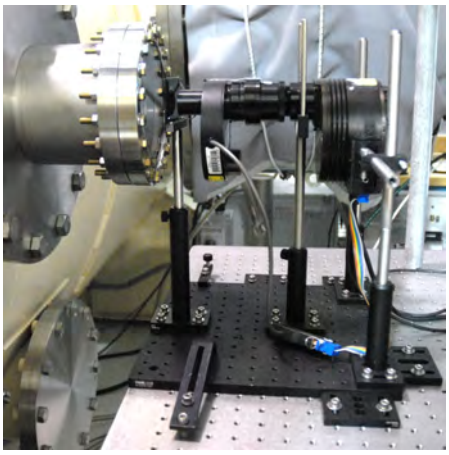

(b) The SBIG ST-10XE camera and optical components.

Figure 2. Experimental Setup

Optical Components

Camera

A Santa Barbara Instruments Group (SBIG) ST-10XE 16 bit CCD camera (Fig. 2(b))was used for this imaging experiment. It employs a Kodak KAF-3200E 3 megapixel CCD (2184×1472 with 6.8 μm pixels). The camera was designed for astronomical imaging and thus long exposure durations (the fastest shutter speed is 0.12 s). It interfaces with t-mount optical components. The instrument has an electronic chiller to reduce thermal image noise, which was set to 5°C for these measurements. A 70 mm focal length lens was mounted to the camera along with a variable aperture diaphragm set to a 9.7 mm diameter making for an f-number of f/7.2. Optical filters were stored and positioned with an SBIG CW-8 electronic filter wheel. The camera was controlled with a laptop PC. See Fig. 4 for a schematic of the optical set up.

Filters

Two 25 mm diameter interface filters from Custom Scientific were used to isolate xenon spectral emission lines. Singly charged ion emission was photographed through a bandwidth filter centered at 542 nm filter

with a transmission distribution function having a full width at half maximum (FWHM) of 10 nm. Neutral xenon emission was photographed with a filter centered at 823 nm also with a FWHM of 10 nm. Besides collecting signal from the 823 nm neutral line, this filter also gathers emission from the 828 nm neutral line. The high f-number of the optical setup prevented light with high incidence angle from reaching the CCD, which minimized potential filter tuning effects. Figure 3 shows the filter transmission functions along with the spectral radiance of the SPT-100 measured with a spectrometer through a diffuse optical collector.

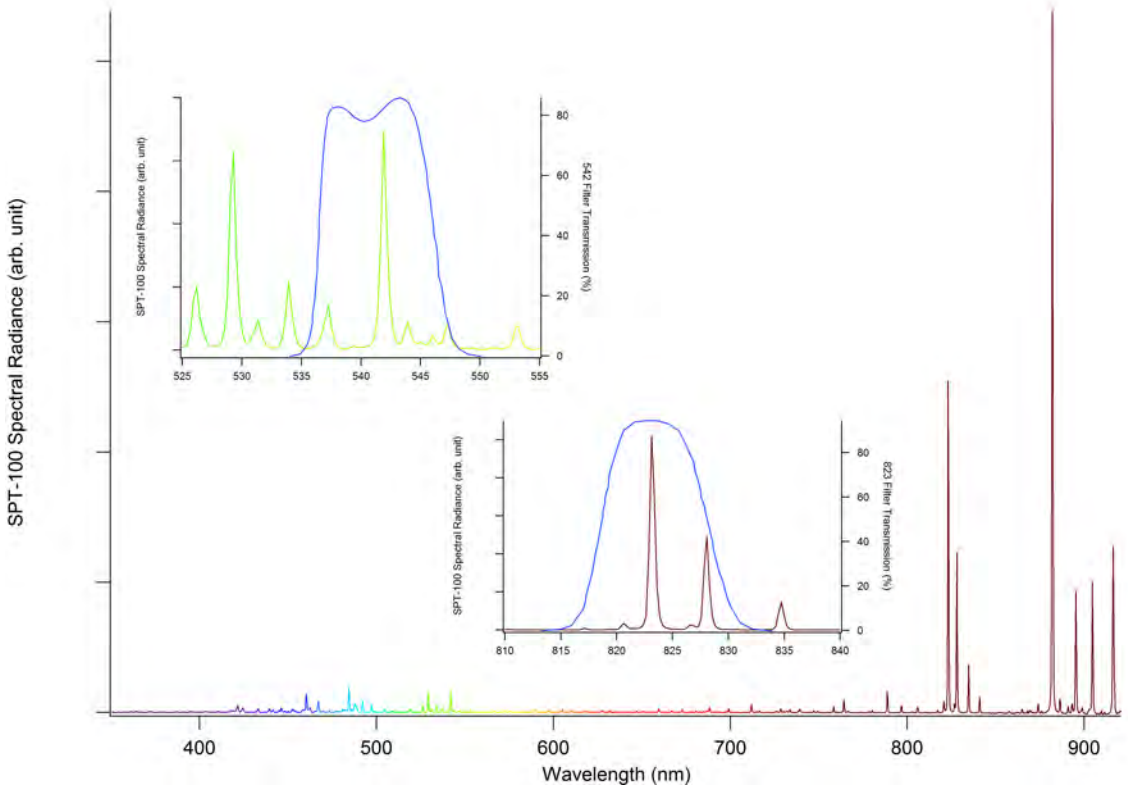

Figure 3. Filter transmission.

Testing Methodology

Optical Techniques

The SPT-100 was mounted with its centerline 198 cm from a 20 cm dia. optical view port on a lateral side the vacuum chamber. The camera was mounted on an optics table outside the chamber and pointed through the window for a profile view of the thruster and plume (Figs. 1 and 4). A flocked graphite panel was placed behind the thruster to serve as an non-reflective black background for the images.

The shiny surfaces of the optical interference filters in conjunction with the other optical surfaces created a mirrored and inverted reflection of the plume about the vertical centerline of the photo that appeared in the camera images. Constraining the plume image to one side of the frame was necessary to prevent unwanted reflections from becoming superimposed on the primary plume image. Thus, the thruster was framed in the camera's field of view with its plume confined to the right half the frame (with its downstream axis pointing rightward). Unfortunately, this solution to the reflection problem required discarding one half of the image area.

A motion stage controlled optical shade (Figs. 2(a) and 4) was constructed from a grafoil (flexible graphite) sheet covered with graphite felt and placed inside the chamber so that certain regions of the thruster, which varied drastically in brightness, could be selectively blocked from the view of the camera. The shade could be positioned so that it blocked the cathode (very bright neutral emission) or the region of the plume upstream of z=134 mm. Blocking bright regions of emission allowed for exposures of dimmer regions that more fully utilized the bit depth of the CCD by preventing overexposed regions with pixel bleeding. In some cases,

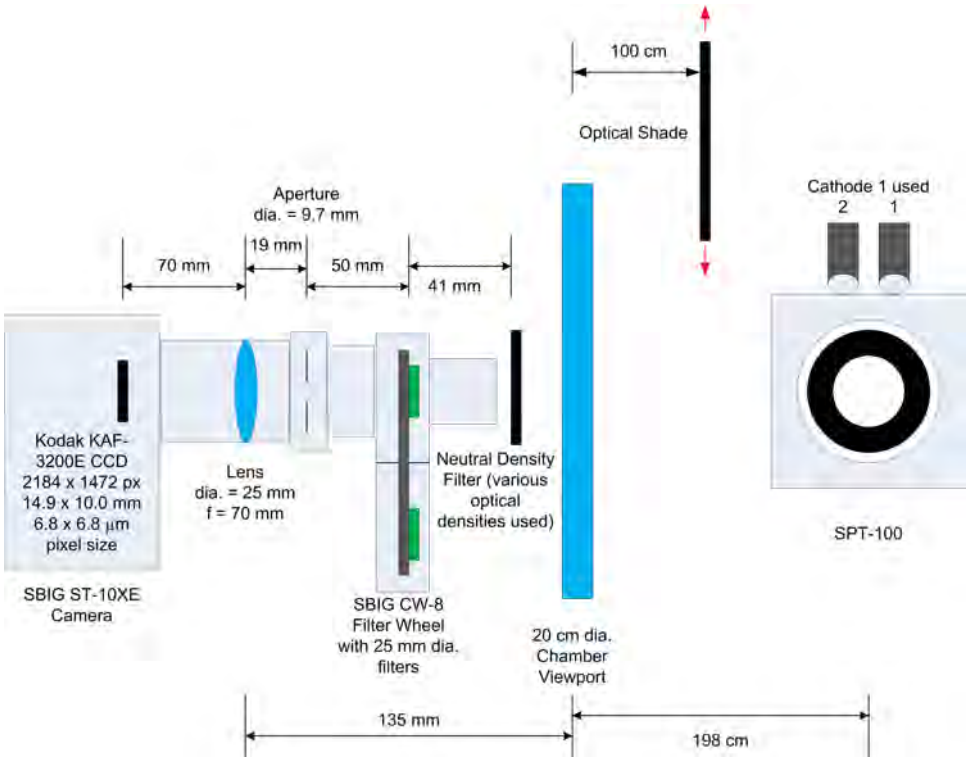

Figure 4. Schematic of optical setup

separate exposures for different regions were combined to form a composite photo, effectively increasing the dynamic range of the image. Three different neutral density (powers of 0.75, 2.0, and 2.5) were used to enable exposure times of between 1 s and 30 s and were selected based on the brightness of the region being photographed.

To improve the signal to noise ratio in the photographs, 10 exposures were averaged for each image. A dark frame (photo with shutter closed) for the same exposure duration and same CCD temperature was subtracted to remove noise caused by thermal effects. Images were also corrected with flat field images, which are images of a uniformly lit flat surface. Images are divided by the flat field image to correct for vignetting and variations in pixel response. Flat field corrections are important in photometric studies such as the present one where vignetting caused up to a 60% brightness variation between the image center and corner in uncorrected images.

Calibrations of the optical system were performed by photographing an integrating sphere inside the chamber illuminated by an Oriel Model 63355 quartz tungsten halogen lamp with a NIST traceable irradiance curve. Calibration photographs were used to determine the fractional transmittance of each neutral density filter at 542 nm and 823 nm. The relative quantum efficiency of the CCD at 542 nm and 823 nm was also measured through calibration photos. With knowledge of these parameters, images taken with different neutral density filters and interference filters could be scaled relative to each other in terms of radiance according to Eq. 1.

$$R = \frac{Cn}{Q\lambda\Delta t f_i} \tag{1}$$

Tests were performed to measure pixel response with exposure time to determine the point near the upper limit of pixel count range where the CCD response became nonlinear. All image exposure times were selected to ensure that pixel counts never exceeded the linear response limit.

Inverse Abel Transformation

These photographic images can be considered to approximate a line-of-sight data set where plume emission is integrated along the x-axis of the thruster coordinate system. In order to study emission as a function of r, an Abel inversion deconvolution was applied to image data. Besides the line-of-sight assumption, the plasma was also assumed to be optically thin and radially symmetric along the z-axis for a given direction of the y-axis. In this study, the half of the plume in the positive y-axis (non-cathode side) was chosen for Abel analysis because it was assumed to have a higher degree of symmetry due to less perturbation from cathode.

The forward Abel transform for a radially symmetric function, $f(r)$ is given by[8]

$$F(y) = 2\int_y^\infty \frac{f(r)rdr}{\sqrt{r^2 - y^2}} \tag{2}$$

and the analytical inverse transformation is

$$f(r) = -\frac{1}{\pi}\int_r^\infty \frac{dF}{dy}\frac{dy}{\sqrt{y^2 - r^2}} \tag{3}$$

The inverse Abel transform is impractical to solve directly with numerical data due to the fact that it requires differentiation of experimental data, which may be noisy, and contains a singularity.[9] There are several types of approaches to performing the inverse Abel transform.[10–12] Here the Fourier method described in Ref. 10 was used where the unknown radial function is constructed from a series expansion of cosine terms each multiplied by an amplitude factor. The amplitude value for each cosine term is determined through a least squares fit of the forward Abel transform equation with the line-of-sight data. The number of cosine terms chosen for the expansion determines the amount of resolution and noise filtering in the transform. In the present study, 50 cosine terms were used.

Thruster Operating Conditions

Thruster operating conditions for imaging were selected so that the effects of background pressure, discharge voltage, and propellant flow rate on emission could be characterized. The operating conditions photographed are summarized in Table 1. To artificially increase chamber background pressure, extra xenon gas was flowed into the chamber through a feed through at the chamber wall that was 5 cm downstream from the thruster exit plane and 70 cm from the thruster center line. Discharge voltage and propellant flow rates values were increased and decreased by 30% of their nominal values. It is important to note that varying propellant flow rate also affects this thruster's magnetic field because the discharge current is routed through the magnet coils. Therefore, changes in the plume emission for these cases are a result of both factors.

Operating Condition	V_d **(V)**	I_d **(A)**	**Power (W)**	$\dot{m}_a$ **(mg/s)**	$\dot{m}_c$ **(mg/s)**	$\dot{m}_b$ **(mg/s)**	P **(Torr-Xe)**
Nominal	300	4.61	1383	5.15	0.40	0.00	2.28E-05
High Back. Press.	300	4.57	1371	5.15	0.40	4.22	4.55E-05
Low Dis. Voltage	210	4.60	966	5.15	0.40	0.00	2.09E-05
High Dis. Voltage	390	4.56	1778	5.15	0.40	0.00	2.08E-05
Low Prop. Flow Rate	300	2.90	870	3.60	0.28	0.00	1.52E-05
High Prop. Flow Rate	300	5.99	1797	6.69	0.51	0.00	2.74E-05

Table 1. Thruster operating specifications.

Results

For each parameter variation, radiance photograph sets are presented for 542 nm and 823 nm emission showing the low and high value parameter cases side-by-side along with an image showing the change in radiance of the high value parameter case relative to the low value case (Figs. 5, 6, 9, 10, 12, and 13). For the delta images, gaussian smoothing was applied to the original images to control noise amplified through division. Linear color maps are applied to the images to illustrate the variation in radiance near the exit plane. However, radiance decays rapidly beyond about a thruster diameter downstream of the exit plane so

logarithmic contour lines are also added to delineate the shape and magnitude of the radiance. The lowest value contour lines were sometimes omitted where the data was noisy. Blocks were added to the images to denote the channel geometry. Only the plume downstream of the exit plane was photographed so any data that appears to be in the acceleration channel should be ignored. Abel inversion transform analysis was performed for the background pressure and discharge voltage variation cases at six different z-axis locations (2.5, 5, 10, 20, 40, and 80 mm). These data are presented along with the corresponding line-of-sight radiance data (Figs. 7 and 11).

Figures 5 and 6 show the 542 and 823 nm emission, respectively, for the background pressure variation. These photos show a distinct change of the emission structure of the plume for high background pressure where both ion and neutral emission decrease in the plume central core beyond z=50 mm and increase in the laterally surrounding areas. An interesting feature of highly increased 823 nm emission (and 542 nm emission to a lesser degree) is observed near the exit plane outside of the acceleration channel on the non-cathode side of the thruster (y=75 mm). This feature is asymmetric and not observed on the cathode side of the image. With the exception of the plume core, 823 nm emission increases throughout the measurement domain due to the higher density of neutral xenon atoms throughout the operating environment. However, fig. 5(c) shows a 10% decrease in 542 nm emission immediately downstream of the center magnetic pole within 20 mm of the exit plane while emission directly downstream of the acceleration channel remains nearly constant.

This region of decreased emission in the center of the plume may indicate a decrease of interaction between ion beams from opposite sides of the acceleration channel due to a smaller beamlet divergence angle at the exit plane. A study of the effects of background pressure on the SPT-100 performance observed that thrust increases with increasing background pressure.[13] This thrust increase was attributed mostly to decreased plume divergence as measured by probes, which may have been caused by the ion acceleration zone shifting to a more upstream location in the discharge channel as observed in Ref. 14 for the BHT-600 thruster likely due to increased electron mobility from Bohm diffusion.

Figure 7(a) shows a similar ion emission radial profile (calculated through Abel inversion) emanating from the discharge channel for both background pressures through z=20 mm. At 40 mm and beyond, the lower emission at center of the plume is consistent with the observations made from the line-of-sight data. The z=2.5 mm radial profile for the 823 nm emission shown in Fig. 7(b) shows a distinct maxima at the edges of the acceleration channel and a dip in the center. Interestingly, this distribution profile along the channel exit is consistent with laser-induced fluorescence measurements of neutral density for the SPT-140 described in Ref.15. Unlike the ion radial profiles, the neutral profiles change quickly between the two pressure cases with downstream distance. At z = 10 mm the local maxima from the discharge channel edges disappears for the high pressure case and the localized region of high emission centered at y=75 mm and z=20 mm distinctly appears as shown in Fig. 6(c).

The difference between 542 and 823 nm emission for the nominal operating condition is presented in Fig. 8. Throughout the plume, the radiance of the neutral line is stronger. The regions with the highest relative 542/823 emission are the central core of the plume beyond z=50 mm and near the exit of the acceleration channel The regions with the lowest relative emission are found in the lateral areas outside of the thruster plume where there are very few ions.

Figures 9 and 10 show the emission for the discharge voltage variation operating conditions. Figure 9(c) shows that increasing discharge voltage increases ion emission in the plume core 100 mm downstream of the exit plane while it decreases elsewhere. This plume shape may be indicative of the higher energy ions undergoing collisions from geometrical beam interactions farther downstream. A similar, but more broad collision region is seen for the neutral emission in Fig. 10(c) which may be from the beam ions colliding with the diffuse neutral propellant.

The radial ion emission profiles shown in Fig. 7(a) show a similar shape between the two discharge voltage cases with the low discharge voltage case emission significantly stronger near the exit plane. The magnitude of emission becomes nearly the same at z=80 mm. A similar trend is seen for the neutral emission in Fig. 7(b), but the high discharge voltage emission in the central plume is seen to be greater for the 40 and 80 mm traces.

Propellant flow rate effects (in combination with magnetic field effects) are shown in Figs. 12 and 13. Figures 12(b) and 12(b) show that at high propellant flow rate, the magnitude of the radiance becomes much greater and the plume emission appears spherical likely due to a higher rate of scattering collisions with the higher density of unionized propellant. This emission shape is a drastic change from the other test conditions where the shape appears to be influenced by geometrical beam interactions. The total thruster

radiance increases dramatically for these high flow rate cases because of the highly increased collisionality of the plume. The increase in collisions happens mostly in the first 100 mm of the exit plane.

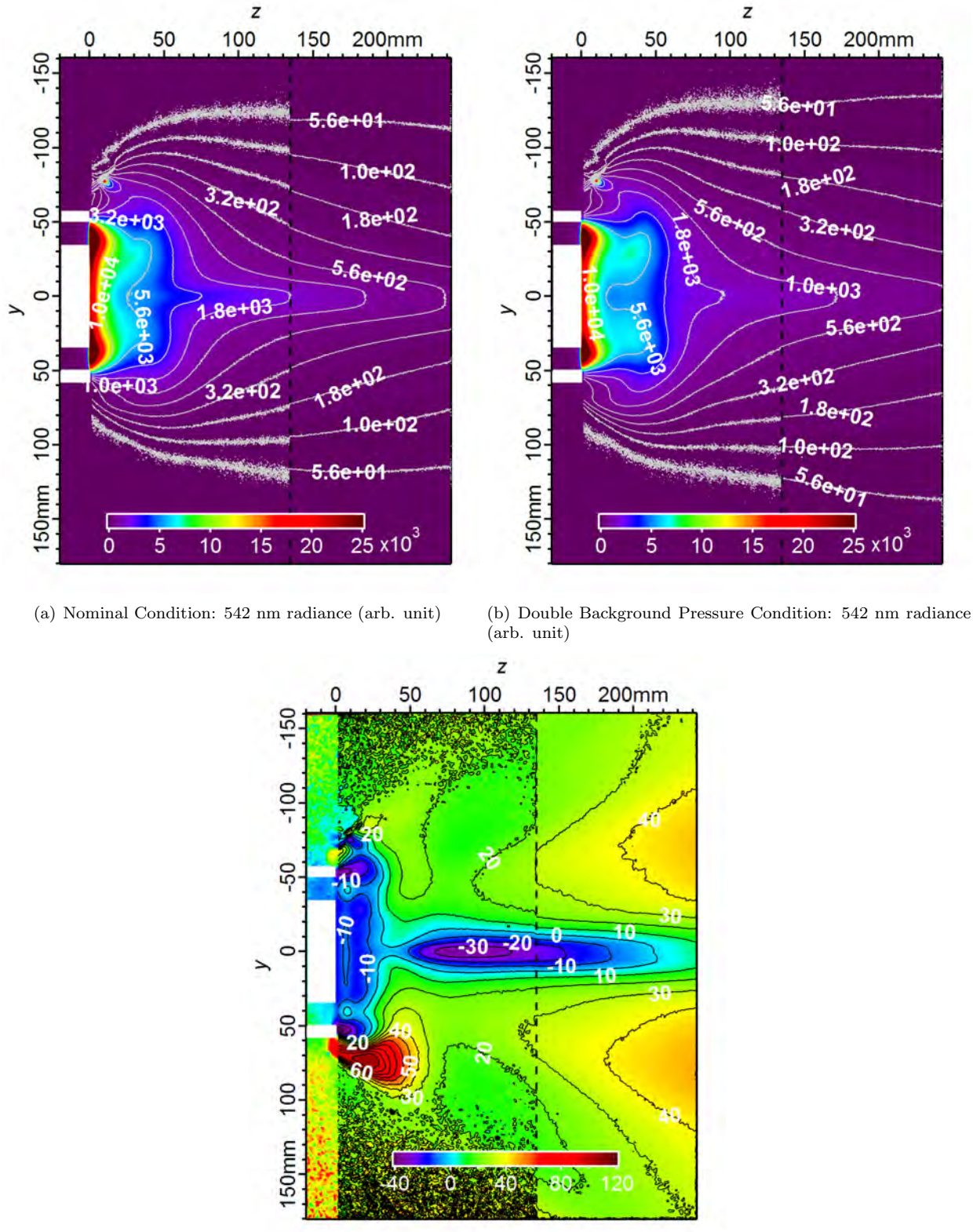

(a) Nominal Condition: 542 nm radiance (arb. unit)

(b) Double Background Pressure Condition: 542 nm radiance (arb. unit)

(c) Δ Radiance (%): $(R_{542:DP} - R_{542:Nom})/R_{542:Nom} \times 100$

Figure 5. Ion emission radiance (542 nm) of the nominal operating condition and the double background pressure condition. Dotted lines mark boundaries of composite photos.

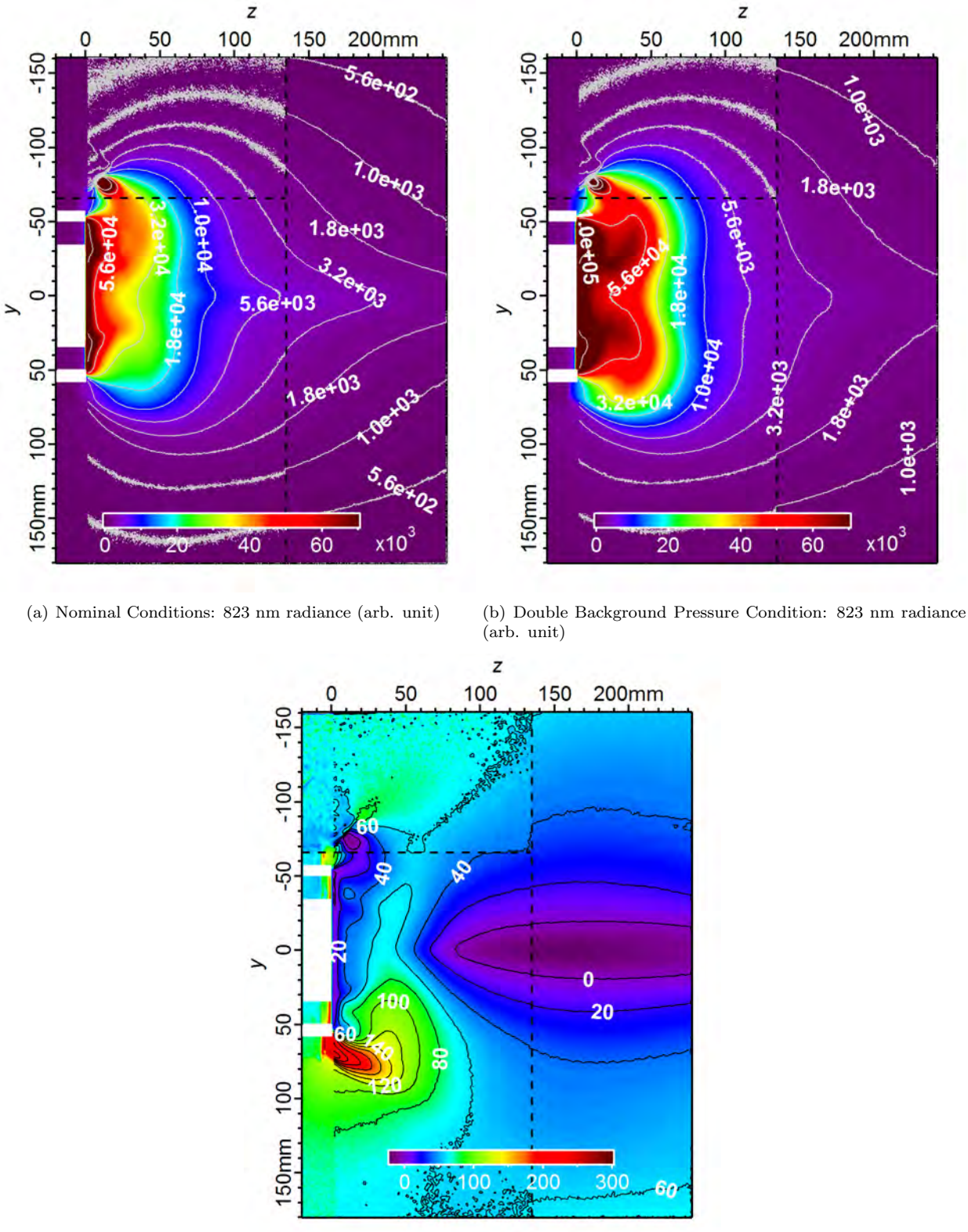

(a) Nominal Conditions: 823 nm radiance (arb. unit)

(b) Double Background Pressure Condition: 823 nm radiance (arb. unit)

(c) Δ Radiance (%): $(R_{823:DP} - R_{823:Nom})/R_{823:Nom} \times 100$

Figure 6. Neutral emission radiance (823 nm) of the nominal operating condition and double background pressure condition. Dotted lines mark boundaries of composite photos.

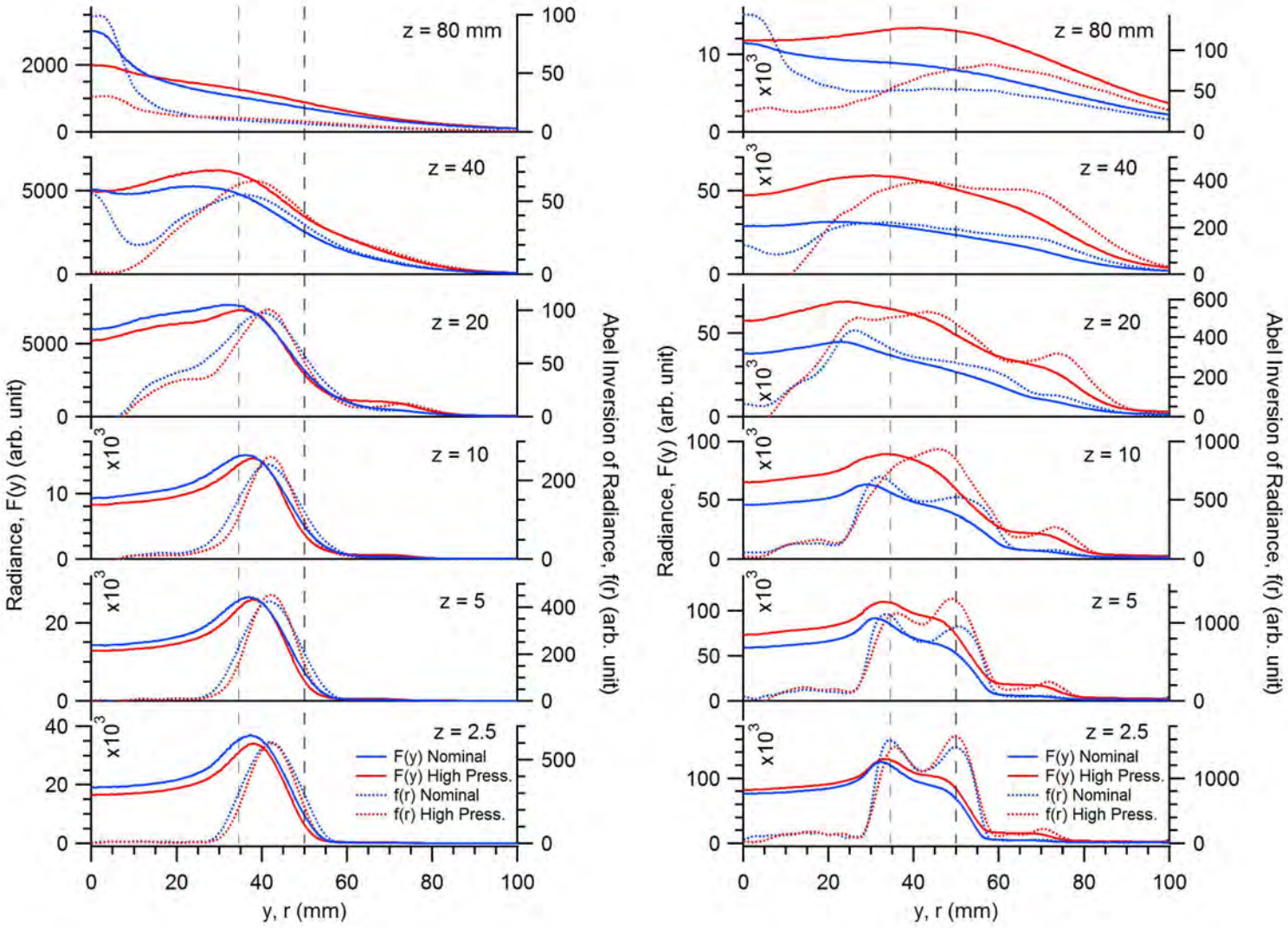

(a) 542 nm emission

(b) 823 nm emission

Figure 7. Cross sections of radiance data for the nominal and high background pressure case at various z locations and their inverse Abel transforms. Dashed lines represent acceleration channel boundaries.

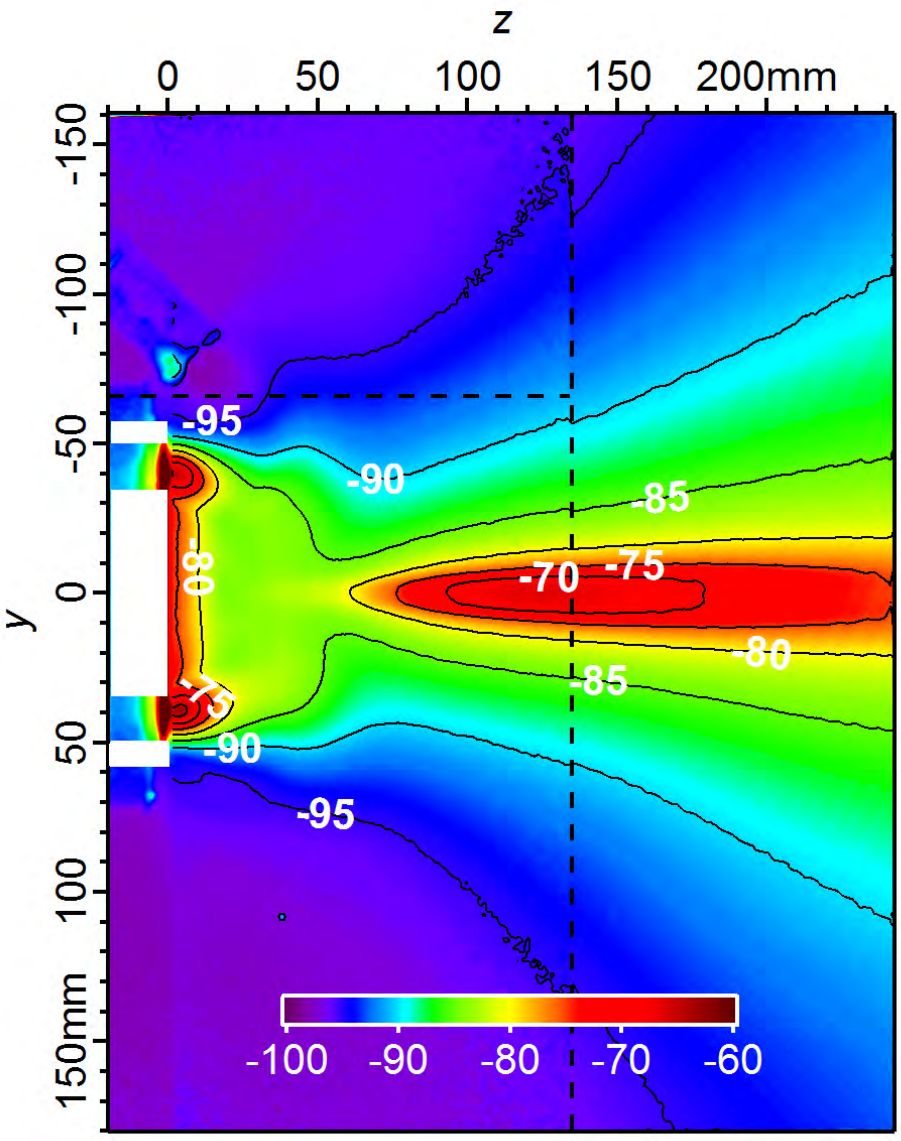

Figure 8. Δ Radiance (%): $(R_{542:Nom} - R_{823:Nom})/R_{823:Nom} \times 100$

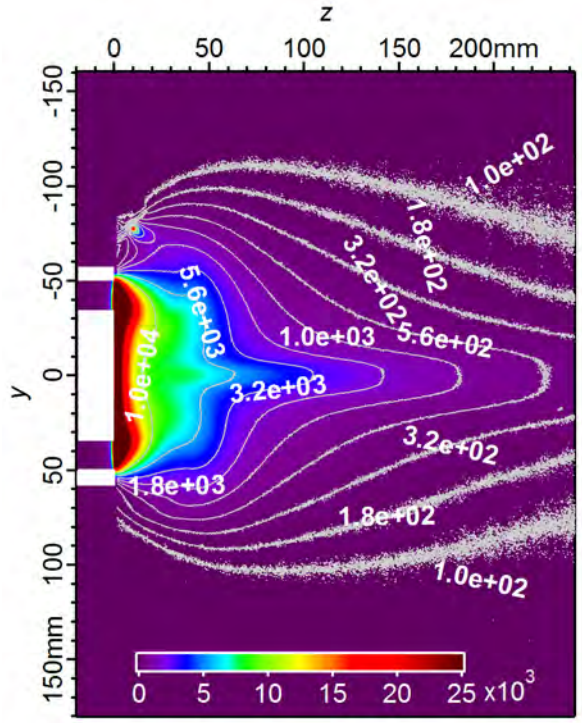

(a) V_d =210 V: 542 nm Radiance (arb. unit)

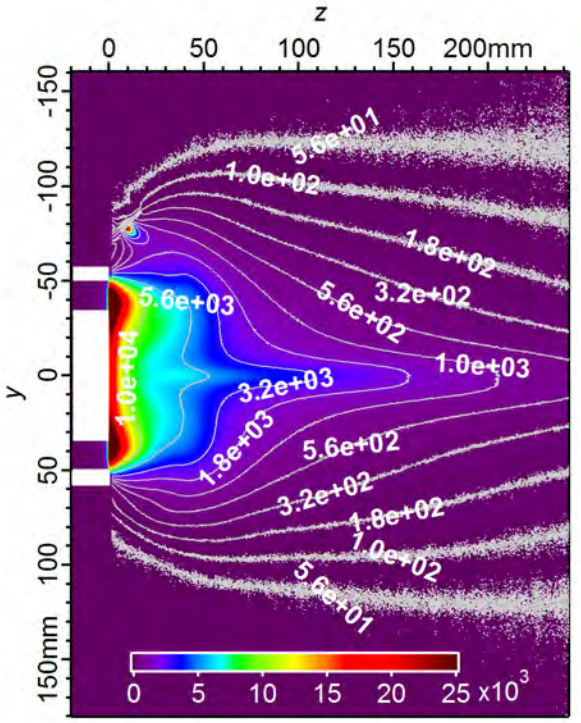

(b) V_d =390 V: 542 nm Radiance (arb. unit)

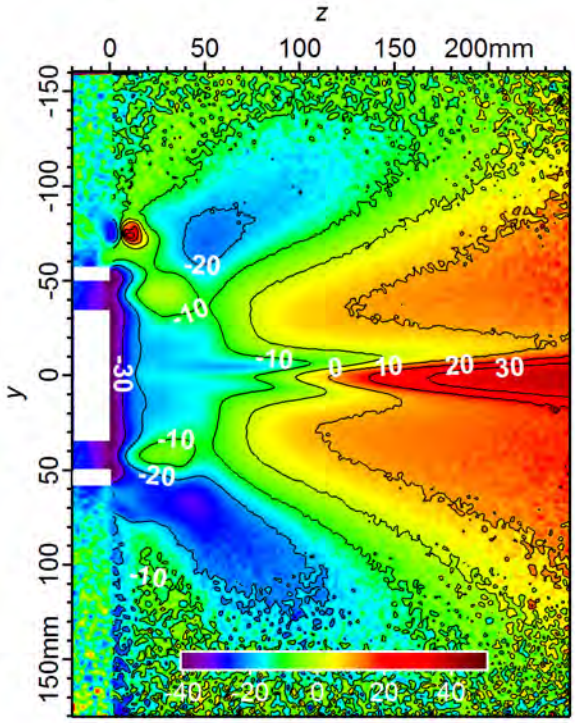

(c) Δ Radiance (%): $(R_{542:Vd390} - R_{542:Vd210})/R_{542:Vd210} \times 100$

Figure 9. Ion emission radiance (542 nm) of the V_d =210 V operating condition and the V_d =390 V condition.

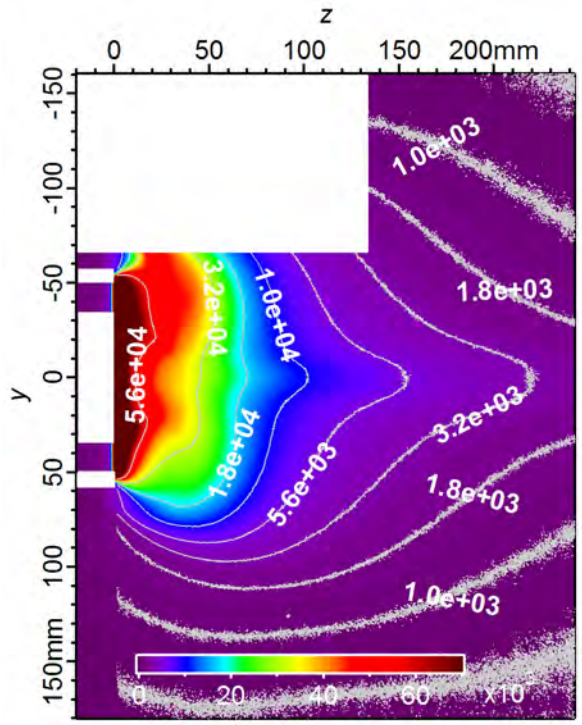

(a) V_d =210 V: 823 nm Radiance (arb. unit)

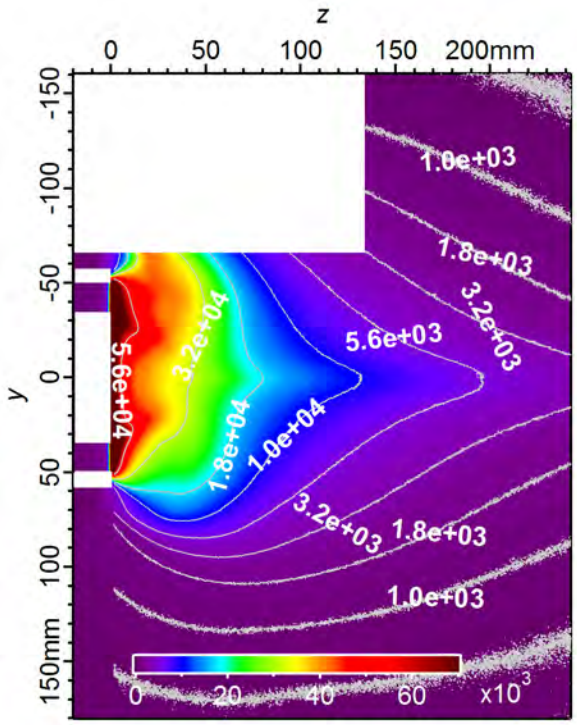

(b) V_d =390 V: 823 nm Radiance (arb. unit)

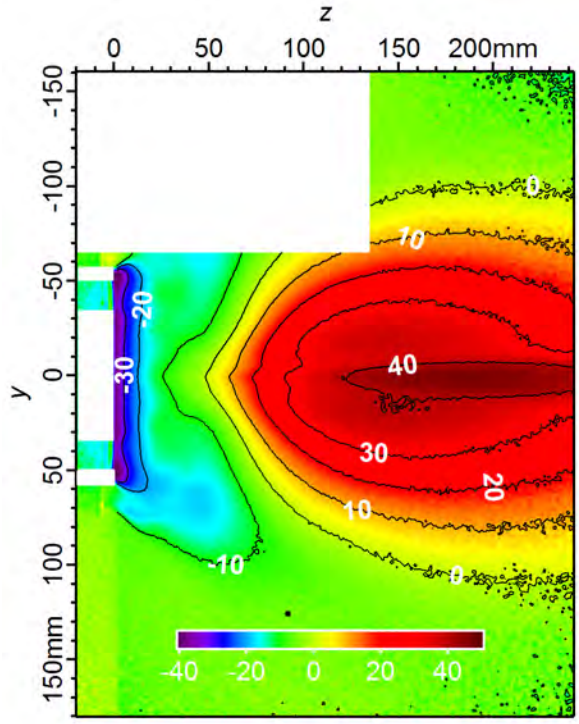

(c) Δ Radiance (%): $(R_{823:Vd390} - R_{823:Vd210})/R_{823:Vd210} \times 100$

Figure 10. Neutral emission radiance (823 nm) of the V_d =210 V operating condition and the V_d =390 V condition. Missing image portion is where optical shade blocked view of cathode.

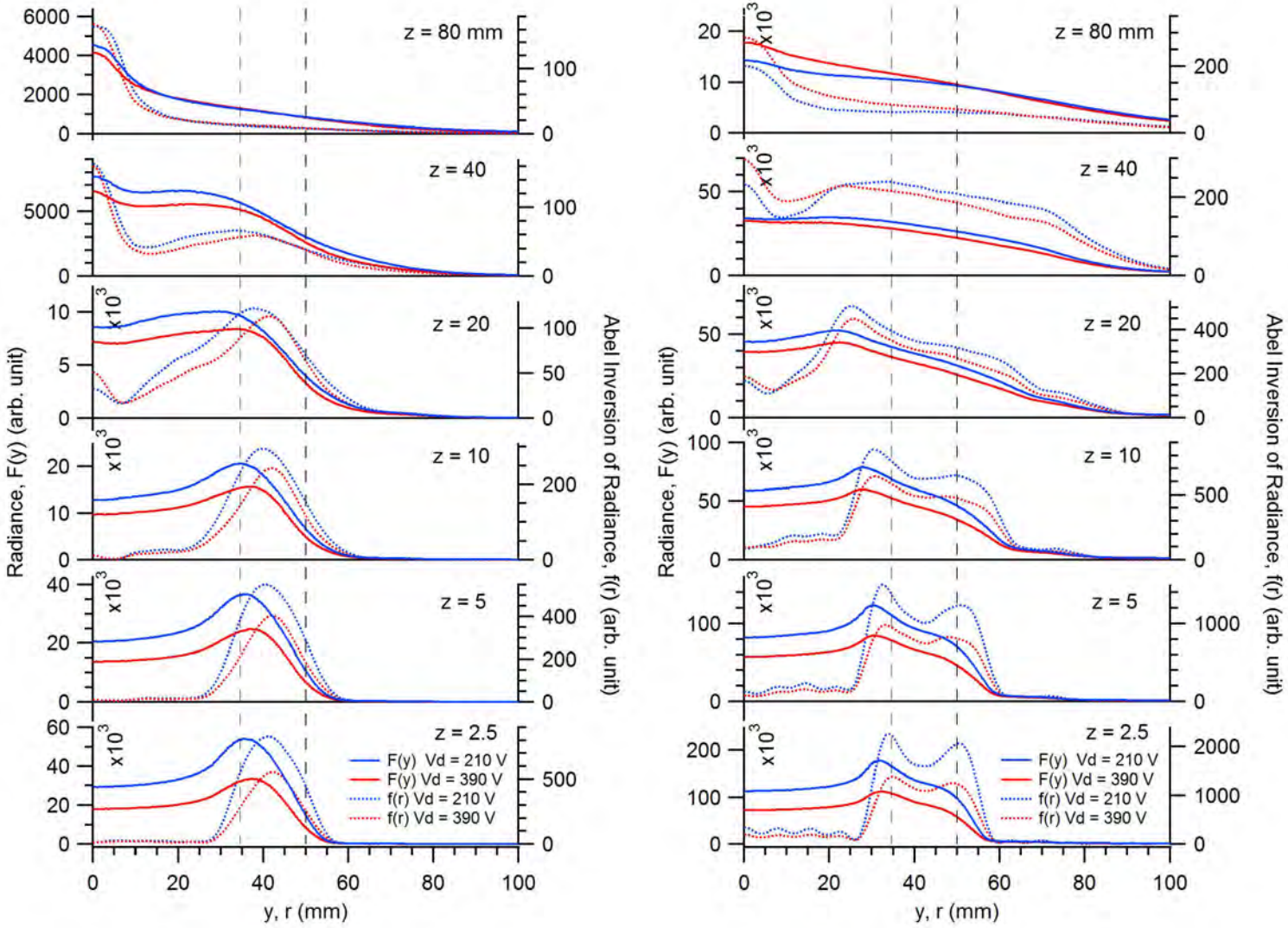

(a) 542 nm emission

(b) 823 nm emission

Figure 11. Cross sections of radiance data for the V_d =210 V and V_d =390 V cases at various z locations and their inverse Abel transforms. Dashed lines represent acceleration channel boundaries.

Conclusions

The imaging of a Hall thruster plume with spectral line filters shows distinct changes in the plume emission structure from ions and neutral particles as operating conditions are changed. These changes reflect variations in plume density and temperature. Photographic measurements can be used as a convenient method for qualitatively examining plume structure, but may also provide a source of useful quantitative analysis when compared to collisional radiative models in numerical simulations or if they can be correlated to other diagnostic measurements of density and/or temperature.

The experimental techniques used in this study showed good promise. Exposures of separate regions of the plume with various integration times and neutral density filters scaled remarkably well in magnitude and plume features blended almost seamlessly when combined for composite images. Overall, the Abel inversion of the photographic data appeared to resolve the evolution of the plume from the exit plane with good detail showing effects that corresponded with the channel geometry. In a few cases, the inversion had trouble resolving data near the plume center and resulted in negative values, but perhaps using a different range of cosine frequencies for the solution or a different inversion technique may alleviate the problem.

In the future, photographic measurements may be performed to match a numerically simulated data set that includes a collisional radiative model for model validation purposes. A more thorough optical calibration technique would allow absolute measurements of thruster radiance, which would add extra value for comparison. Near-field probe measurements of density may be performed to explore the possibility of using photographic data to estimate density values where temperature gradients are sufficiently low. It may be interesting to photograph these probes in the near-field plume to examine the effect their presence has on plasma. The photographic techniques in this study may also be applicable to high-speed photography where time-resolved measurements could be used to study emission as a function of thruster breathing mode oscillations.

References

[1]Hargus Jr., W. A. and Cappelli, M. A., "Laser-Induced Fluorescence Measurements of Velocity within a Hall Discharge," *Applied Physics B*, Vol. 72, No. 8, June 2001, pp. 961–969.

[2]Reed, G. D., William A. Hargus, J., and Cappelli, M. A., "Microwave interferometry (90 GHz) for Hall Thruster Plume Density Characterization," *Proceedings of the 41st AIAA/ASME/SAE/ASEE Joint Propulsion Conference and Exhibit*, 2005, AIAA-2005-4399.

[3]Sekerak, M. J., *Plasma Oscillations and Operational Modes in Hall Effect Thrusters*, Ph.D. thesis, University of Michigan, 2014.

[4]Brown, D. L., *Investigation of Low Discharge Voltage Hall Thruster Characteristics and Evaluation of Loss Mechanisms*, Ph.D. thesis, University of Michigan, 2009.

[5]Sekerak, M. J. et al., "Azimuthal Spoke Propagation in Hall Effect Thrusters," *IEEE Transactions On Plasma Science*, Vol. 43, No. 1, 2014, pp. 72–85.

[6]Roche, S., Bechu, S., Prioul, M., Pagnon, D., Gascon, N., Bouchoule, A., Magne, L., Lasgorceix, P., and Touzeau, M., "Plasma characterisation of an ATON-Hall thruster - Channel and plume investigation," *Proceedings of the 36th AIAA/ASME/SAE/ASEE Joint Propulsion Conference and Exhibit*, 2000, AIAA-2000-3523.

[7]Garner, C. E., Brophy, J. R., Polk, J. E., and Pless, L. C., "Cyclic Endurance Test of a SPT-100 Stationary Plasma Thruster," *In the Proceeding of the 30th AIAA/SAE/ASME/ASEE Joint Propulsion Conference and Exhibit*, 1994, AIAA-94-2856.

[8]Hutchinson, I., *Principles of Plasma Diagnostics*, Cambridge University Press, New York, 1994.

[9]Dribinski, V., Ossadtchi, A., Mandelshtam, V. A., and Reisler, H., "Reconstruction of Abel-transformable images: The Gaussian basis-set expansion Abel transform method," *Review of Scientific Instruments*, Vol. 73, No. 7, 2002, pp. 2634–2642.

[10]Pretzier, G., Jger, H., Neger, T., Philipp, H., and Woisetschlger, J., "Comparison of Different Methods of Abel Inversion Using Computer Simulated and Experimental Side-On Data," *Zeitschrift fr Naturforschung*, Vol. 47a, 1992, pp. 955–970.

[11]Fulge, H., Knapp, A., Eichhorn, C., Wernitz, R., Lohle, S., Fasoulaskand, S., and Herdrich, G., "Improved Abel Inversion Method for Analysis of Spectral and Photo-Optical Data of Magnetic Influenced Plasma Flows," *Proceedings of the 42nd AIAA Plasmadynamics and Lasers Conference*, 2011, AIAA-2011-3456.

[12]Matlock, T., Hargus, Jr., W., Larson, C., and Nakles, M., "Inversion Method for Reconstructing Hall Thruster Plume Parameters from Optical Measurements," *43rd AIAA/ASME/SAE/ASEE Joint Propulsion Conference*, Cincinnati, OH, 2007, AIAA-2007-5303.

[13]Diamant, K. D., Liang, R., and Corey, R. L., "The Effect of Background Pressure on SPT-100 Hall Thruster Performance," *Proceedings of the 50th AIAA/ASME/SAE/ASEE Joint Propulsion Conference*, 2014, AIAA-2014-3710.

[14]Nakles, M. R. and Hargus Jr., W. A., "Background Pressure Effects on Ion Velocity Distribution Within a Medium-Powered Hall Thruster," *Journal of Propulsion and Power*, Vol. 27, No. 4, 2011, pp. 737–743.

[15]Crofton, M. et al., "Neutral Density in the SPT-140 Near-Field Plume," *Proceedings of the 33rd International Electric Propulsion Conference*, 2013, IEPC-2013-399.

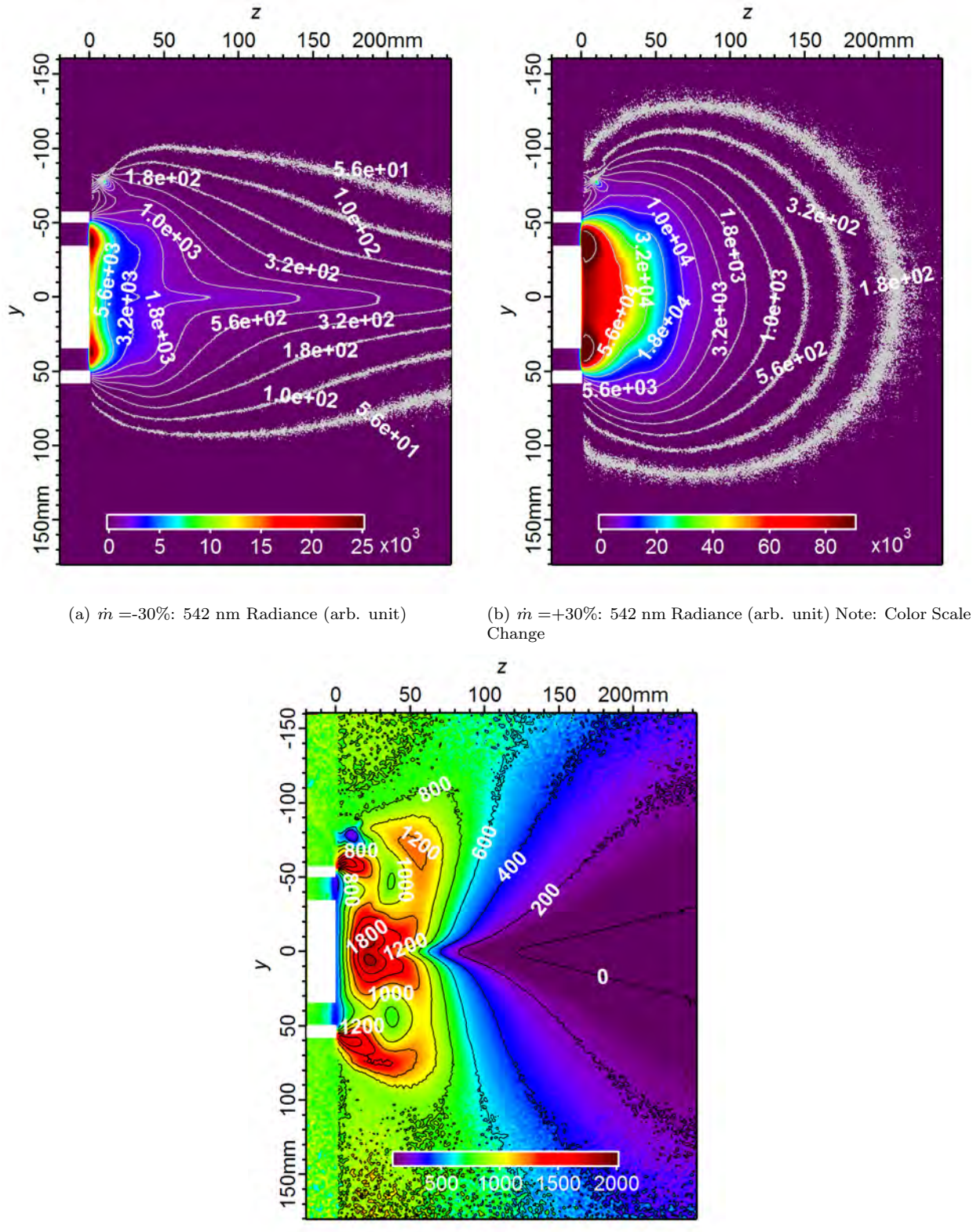

(a) $\dot{m}$ =-30%: 542 nm Radiance (arb. unit)

(b) $\dot{m}$ =+30%: 542 nm Radiance (arb. unit) Note: Color Scale Change

(c) Δ Radiance (%): $(R_{542:m+30\%} - R_{542:m-30\%})/R_{542:m-30\%} \times 100$

Figure 12. Ion emission radiance (542 nm) of the $\dot{m}$ =-30% operating condition and the $\dot{m}$ =+30% condition.

Joint Conference of 30th ISTS, 34th IEPC and 6th NSAT, Kobe-Hyogo, Japan, July 4-10, 2015

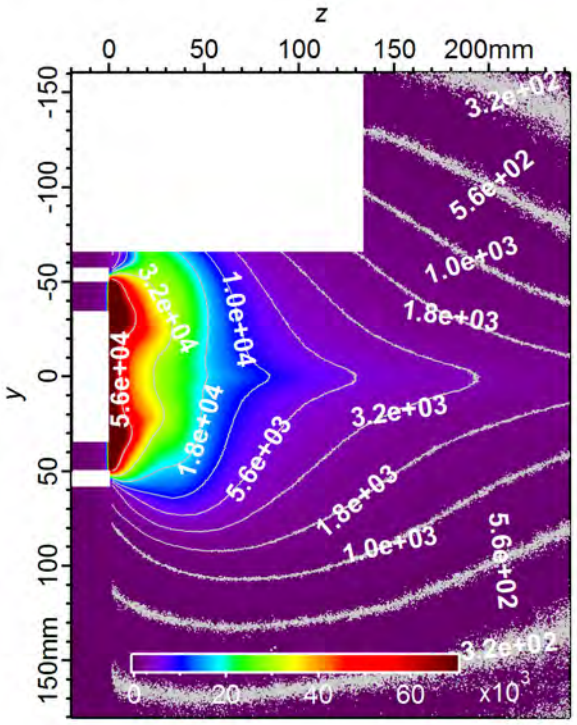

(a) $\dot{m}$ =-30%: 823 nm Radiance (arb. unit)

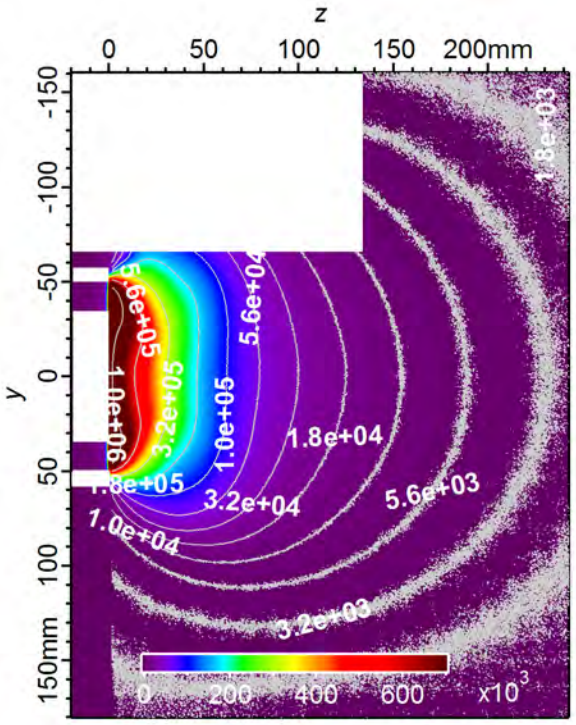

(b) $\dot{m}$ =+30%: 823 nm Radiance (arb. unit) Note: Color Scale Change

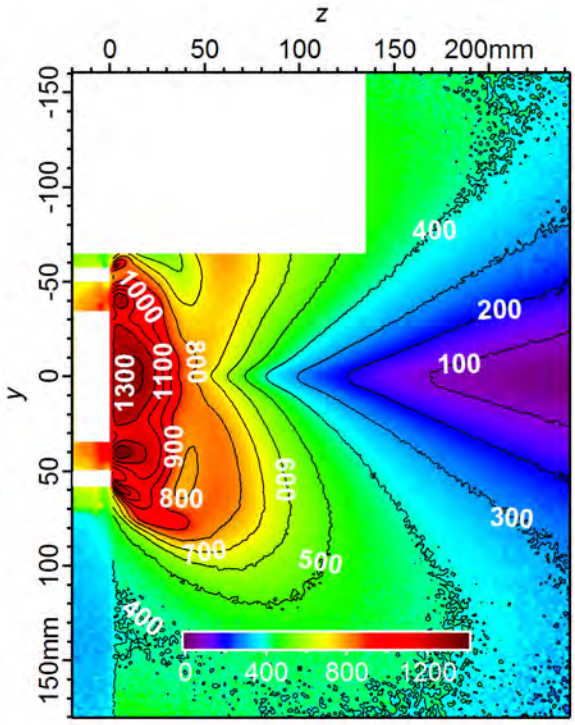

(c) Δ Radiance (%): $(R_{823:m+30\%} - R_{823:m-30\%})/R_{823:m-30\%} \times 100$

Figure 13. Ion emission radiance (823 nm) of the $\dot{m}$ =-30% operating condition and the $\dot{m}$ =+30% condition. Missing image portion is where optical shade blocked view of cathode.

IEPC-2015-416/ISTS-2015-b-416

An Investigation into the Spectral Imaging of Hall Thruster Plumes

M.R. Nakles
ERC, Inc.
Spacecraft Propulsion Branch
Edwards Air Force Base, CA

M.R. Holmes, W.A. Hargus, Jr.
Air Force Research Laboratory
Spacecraft Propulsion Branch
Edwards Air Force Base, CA

Introduction

- **Motivation**
  - Explore the possibility of using photography as a non-intrusive near-field optical diagnostic
  - Emission data can be compared to numerical simulations with collisional radiative models
- **Summary of Experimental Objectives**
  - Use a 16 bit camera with optical interference filters to image ion and neutral emission lines (542, 823 nm)
  - Examine how various operating conditions affect the near-field plume emission of the SPT-100
    - Subtract photos to view relative changes between operating conditions
  - Convert line-of-sight image data to radially dependent emission functions through Abel inversion

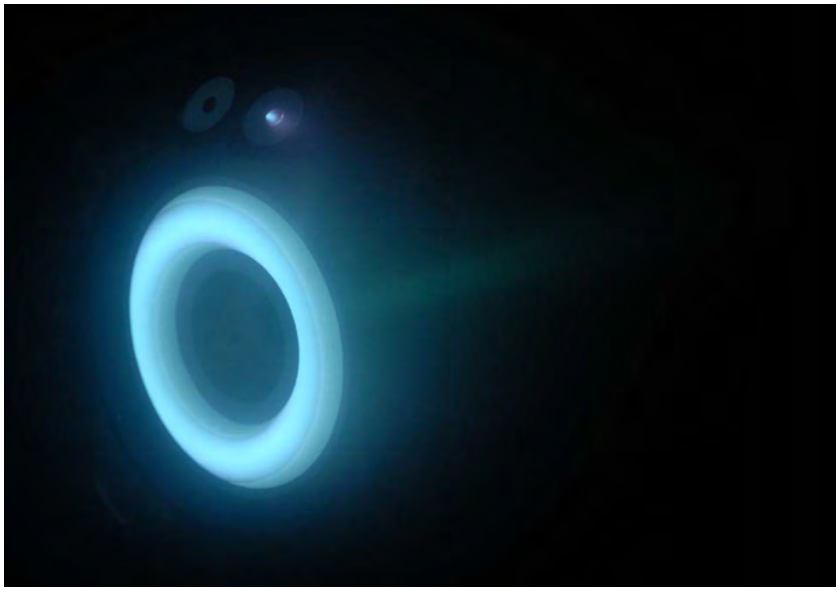

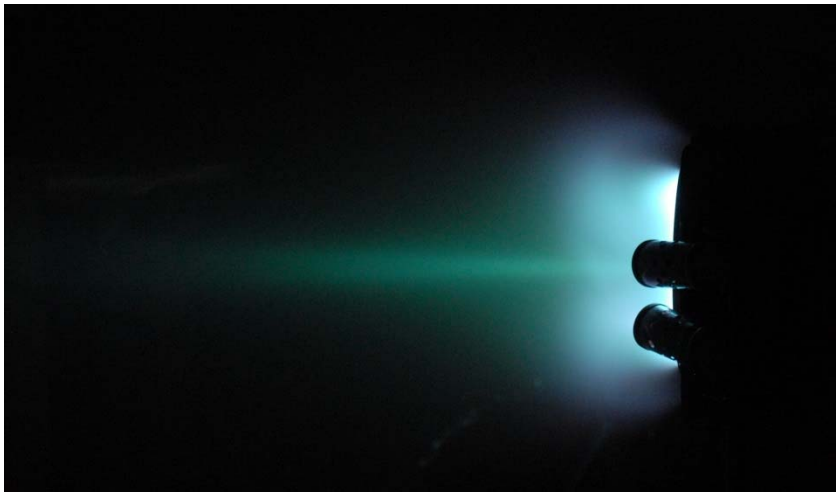

Testing Facility and Hall Thruster

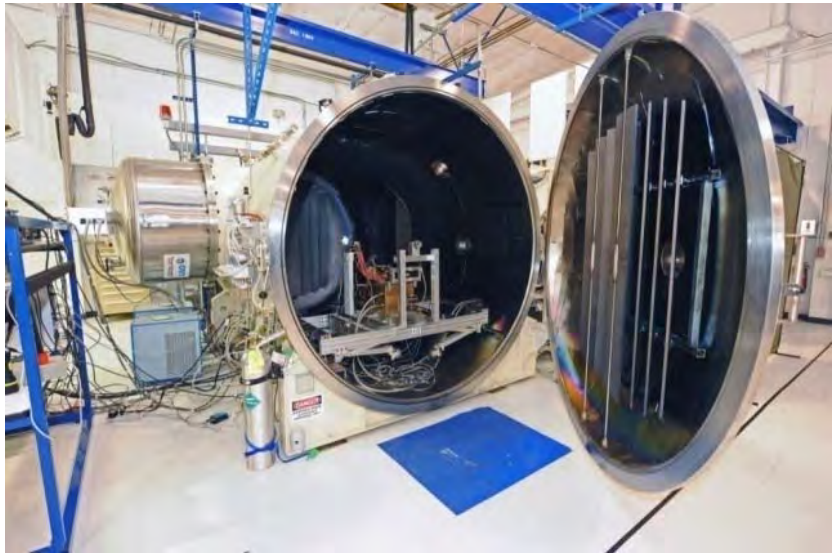

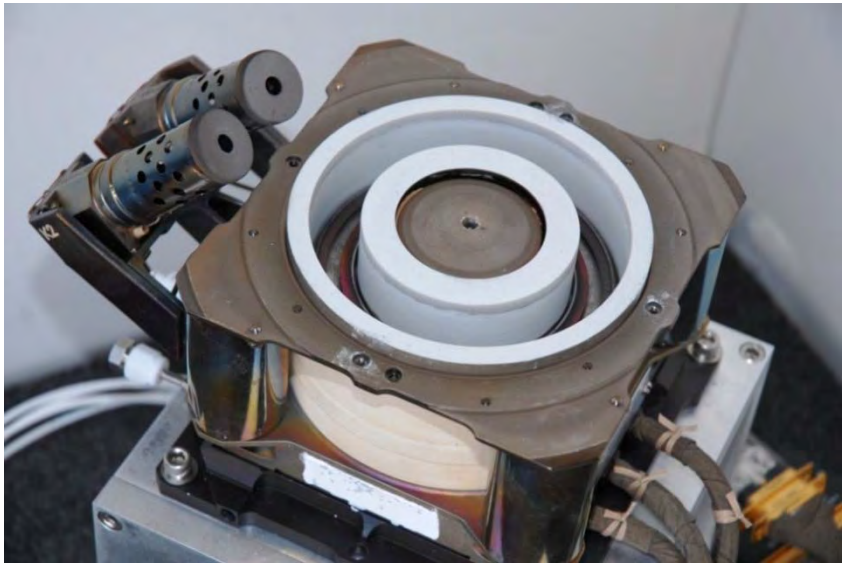

- **Chamber 1 AFRL Edwards AFB**
  - 2.4 m dia., 4.1 m length, stainless steel
  - Two cryogenic pumps
    - 1.2 m dia., LN2 baffled (70 K), 2 stage He (15 K)
    - SPT-100 nominal operation background pressure with Xe: 2.3×10^{-5} Torr (5.55 mg/s)

- **Flight Model SPT-100**
  - Nominal Anode Power: 1350 W
  - Conventional 5 magnetic core design
    - One inner, four outer connected in series
    - Magnetic circuit current supplied by anode current
  - Acceleration channel: 100 mm outer dia., 69 mm inner dia., 28 mm depth
  - 2 lanthanum hexaboride (LaB_6) cathodes

Optical Setup

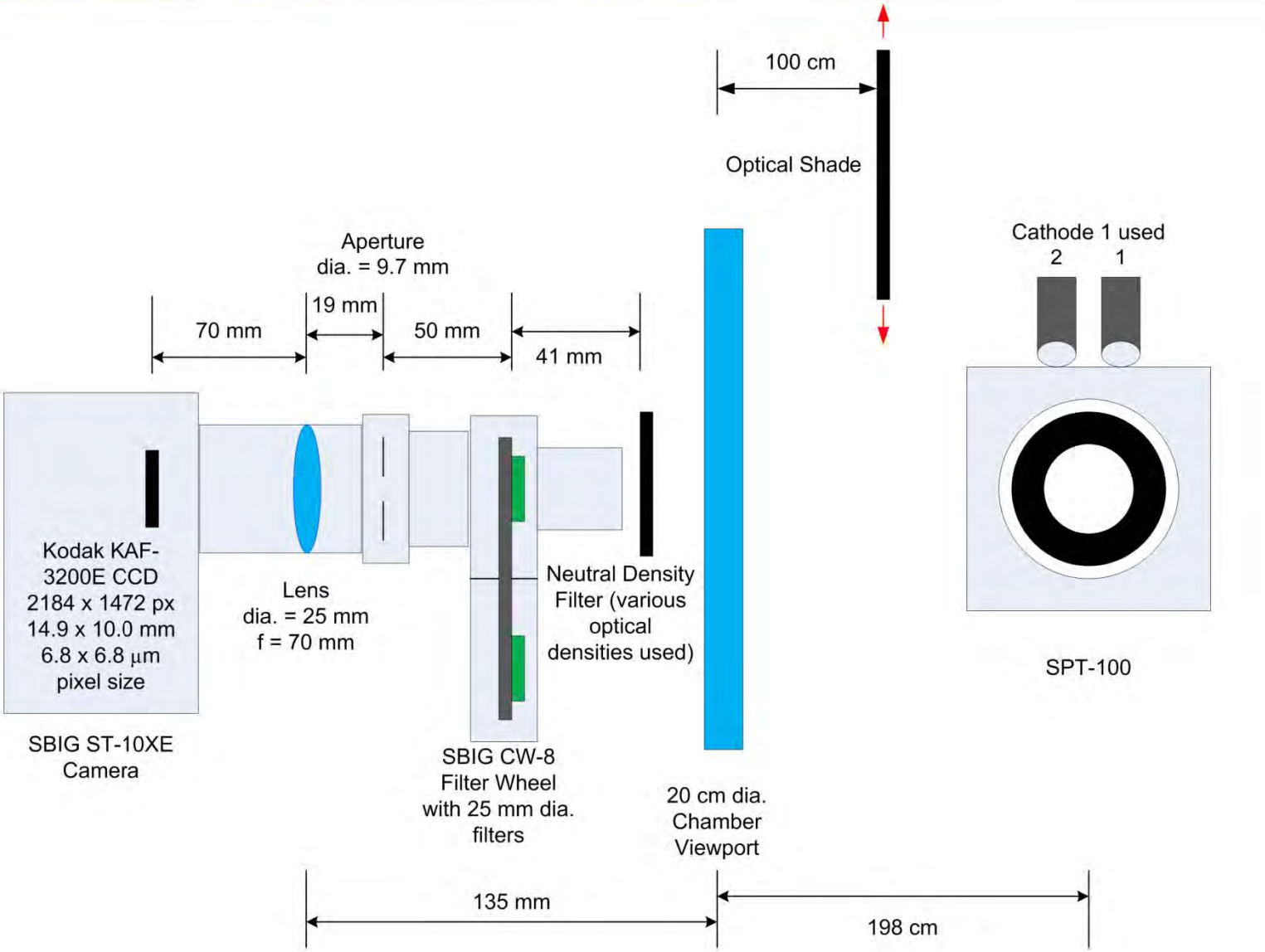

Optical Setup (Continued)

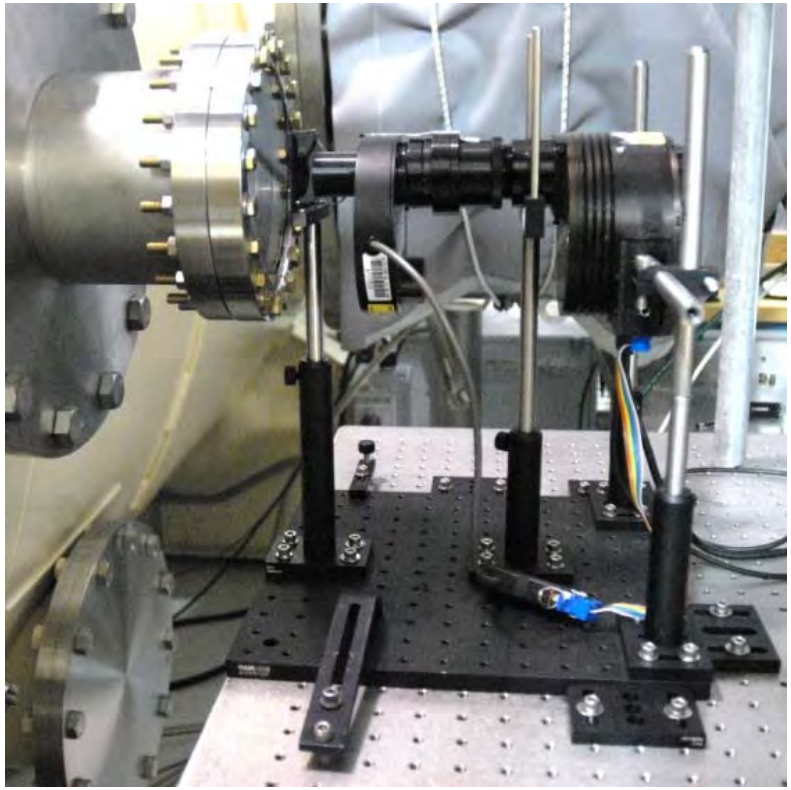

- **SBIG ST-10XE Camera**
  - 16 bit, 3 MP
  - f/7.2 optical setup
  - Covered with shroud during exposures

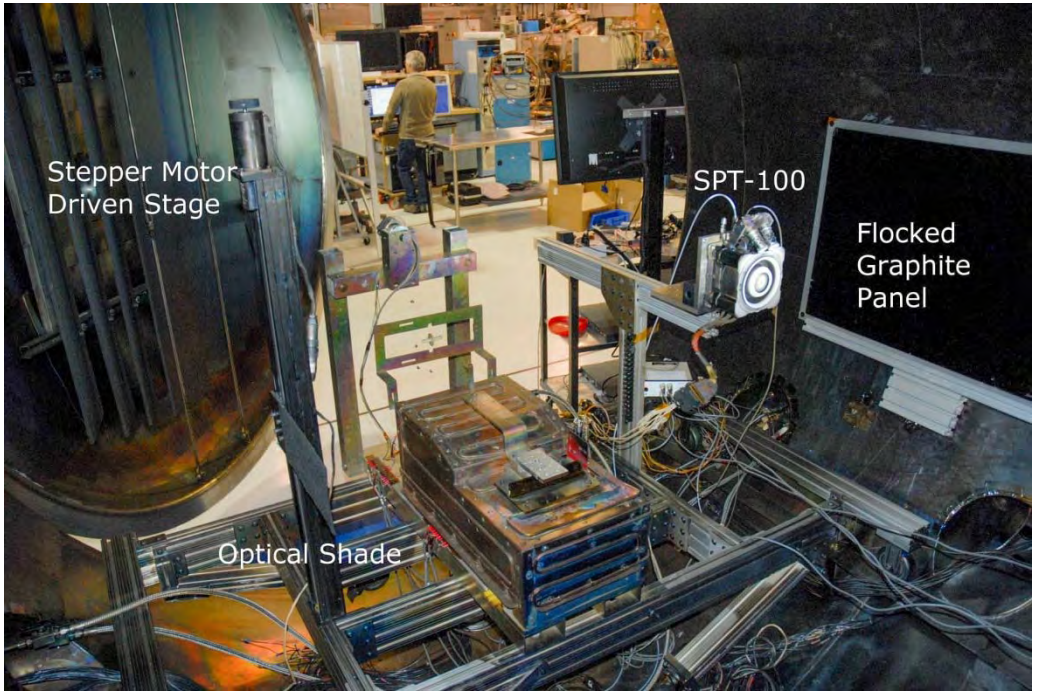

- **Chamber 1 Interior Setup**
  - Thruster mounted for profile view
  - Optical shade controlled with stepper motor driven stage
    - Blocks cathode and upstream plume
  - Non-reflective flocked graphite panel for background

Optical Interference Filters

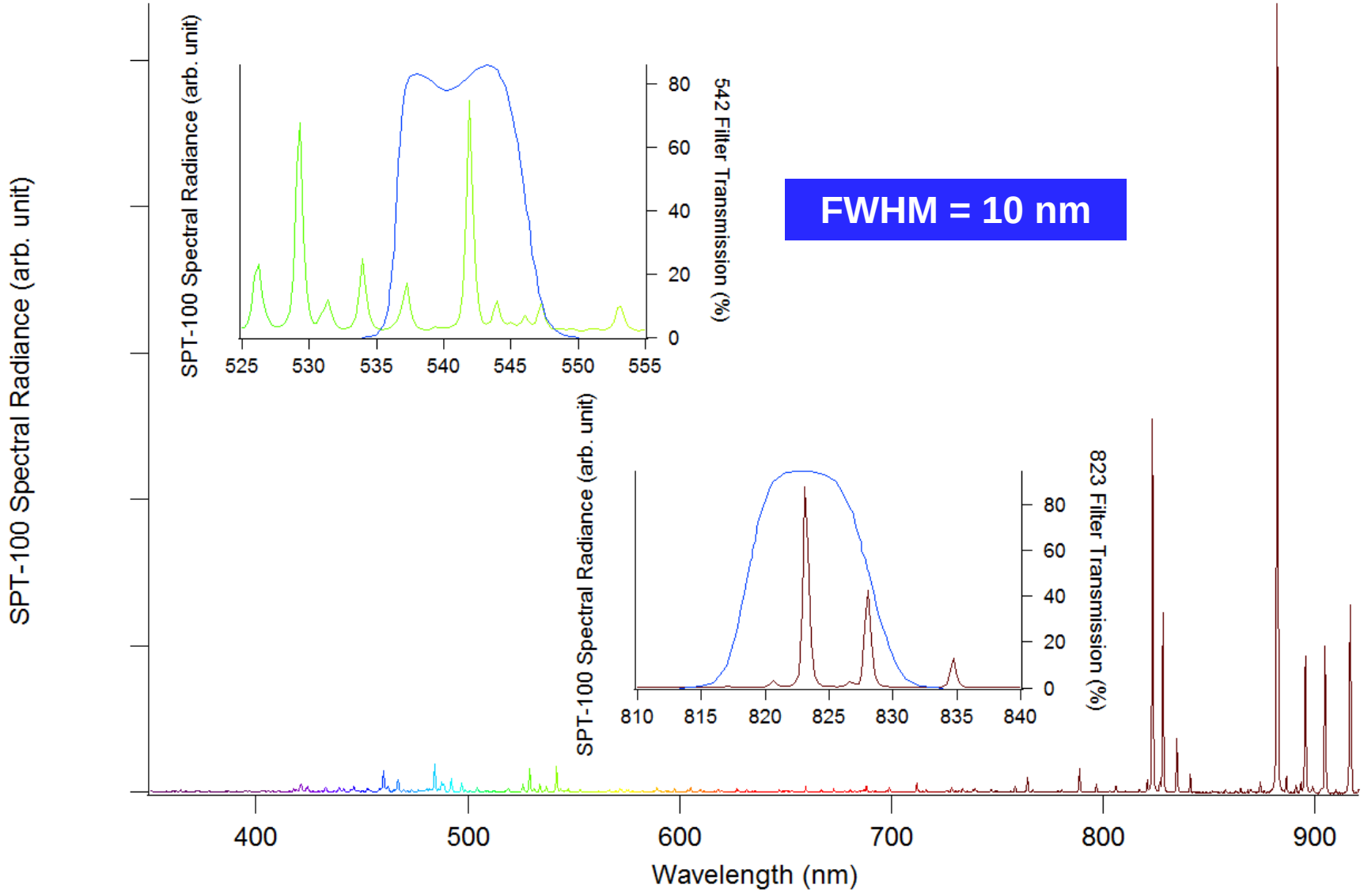

FWHM = 10 nm

Optical Techniques

- **Image Noise Reduction**
  - Average 10 exposures for each image
  - Subtract dark frame from image
  - Set camera's electronic chiller to 5° C
- **Flat-Field Correction**
  - Photograph uniformly illuminated surface
  - Divide images by flat-field images to correct for:
    - Vignetting (up to 60% brightness variation from center to corner in non-corrected images)
    - Non-uniform pixel response
    - Dust particles on CCD

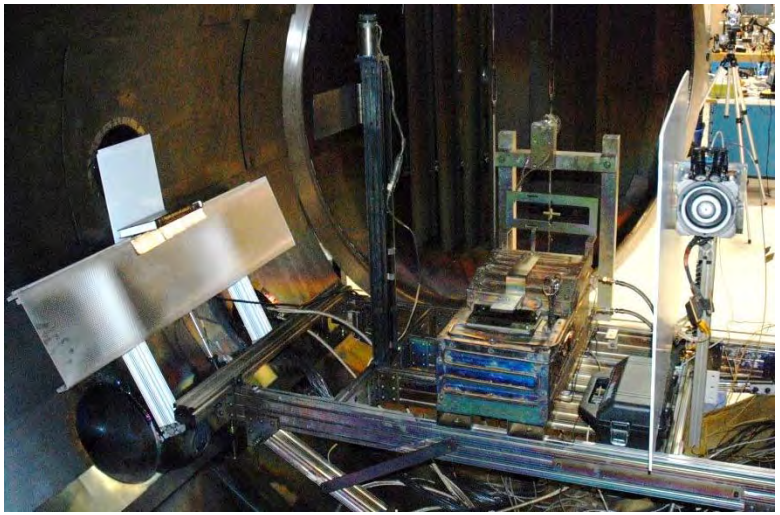

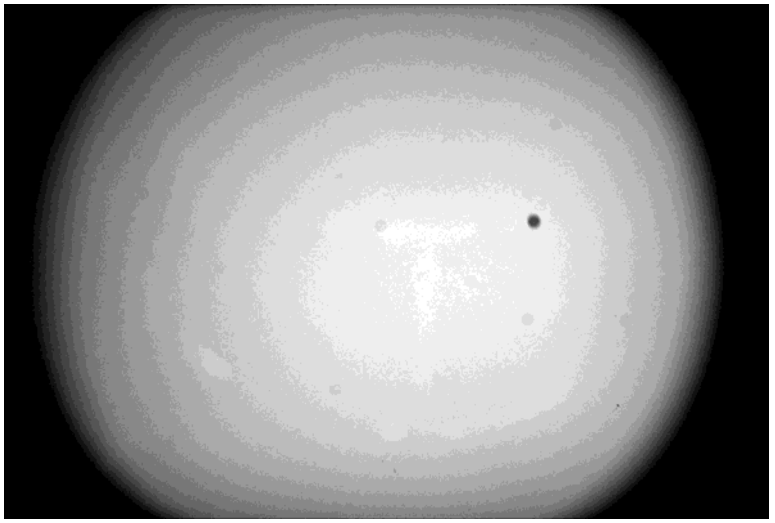

Relative Radiance Calibration

- Scale images through relative radiance calibration
  - Integrating sphere
  - Quartz tungsten lamp with NIST traceable irradiance curve
- Calculate f_λ and Q_{823} / Q_{542}
- Characterize pixel response to ensure exposures are within the linear regime

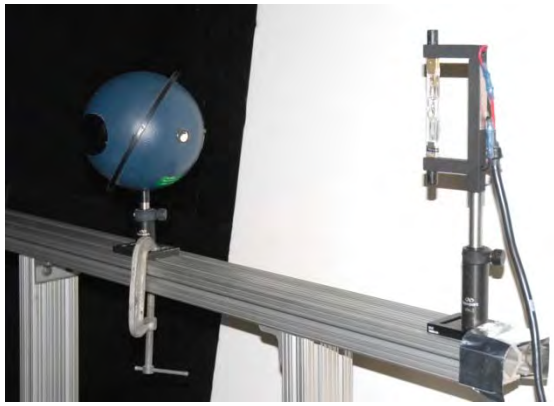

$$R = \frac{n}{f_\lambda Q_\lambda \frac{\lambda}{hc} A_{\text{pixel}} \frac{A_{\text{lens}}}{s'^2} \Delta t} = C \frac{n}{Q_\lambda \lambda \Delta t f_\lambda}$$

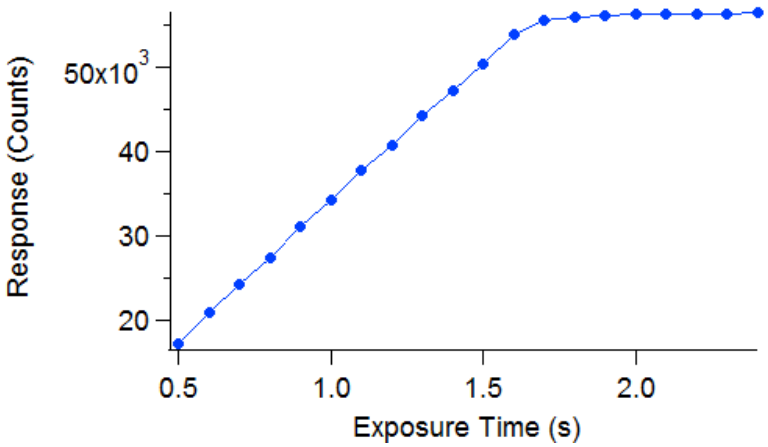

$$\frac{R_1}{R_2} = \frac{n_1}{n_2} \frac{Q_{\lambda 2}}{Q_{\lambda 1}} \frac{\lambda_2}{\lambda_1} \frac{\Delta t_2}{\Delta t_1} \frac{f_{\lambda 2}}{f_{\lambda 1}}$$

C = combined physical and geometrical constants
n = CCD count value
f_λ = fractional transmittance of ND filter at a given wavelength
Q_λ = CCD quantum efficiency at a given wavelength
Λ = wavelength
h = Planck constant
c = speed of light
A_{pixel} = area of CCD pixel
A_{lens} = area of lens
s' = distance between lens and CCD
Δt = exposure time

Abel Inversion Technique

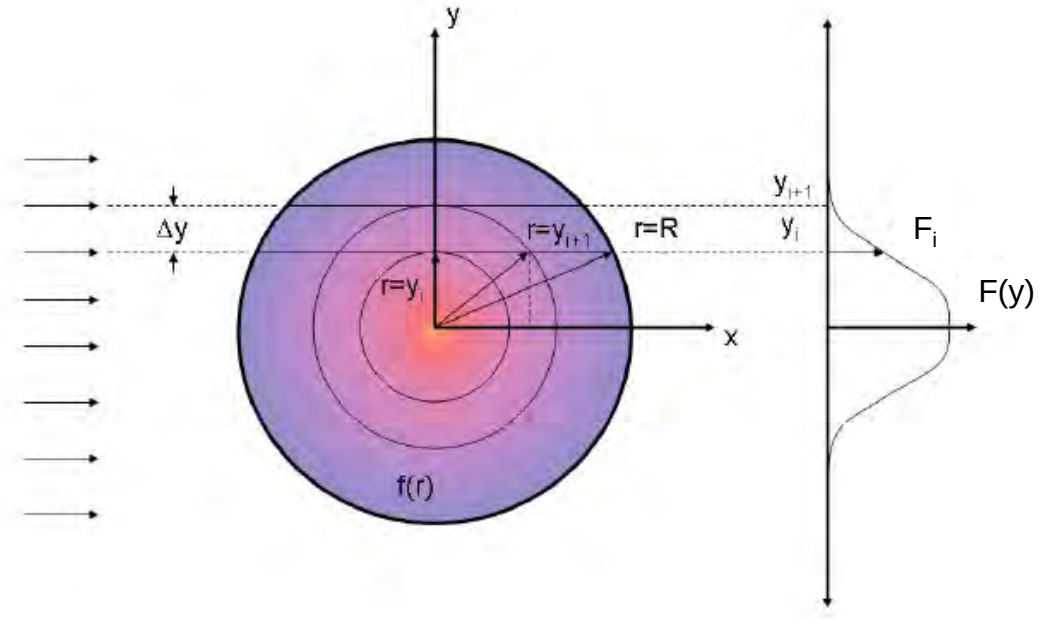

Forward Transform

$$F(y) = 2\int_y^R f(r)\frac{r}{\sqrt{r^2 - y^2}}dr$$

Inverse Transform

$$f(r) = -\frac{1}{\pi}\int_y^R \frac{dF(y)}{dy}\frac{dy}{\sqrt{y^2 - r^2}}$$

- Inverse Abel Transform is not practical to solve directly with numerical means
  - Singularity
  - Requires derivative of experimental data
- Use "Fourier Method"* to approximate *f(r)* as a cosine expansion

$$f(r) = \sum_{N_l}^{N_u} A_n f_n(r)$$

$$f_0(r) = 1,$$

$$\boldsymbol{f_n(r) = 1 - (-1)^n \cos\left(n\pi\frac{r}{R}\right)}$$

- Choose frequency limits to balance noise filtering and detail retention
- Least squares fit of forward transform with experimental data determines values of A_n

*Pretzier, G., Jger, H., Neger, T., Philipp, H., and Woisetschlger, J., "Comparison of Different Methods of Abel Inversion Using Computer Simulated and Experimental Side-On Data," *Zeitschrift fr Naturforschung*, Vol. 47a, 1992, pp. 955-970.

Thruster Operating Conditions

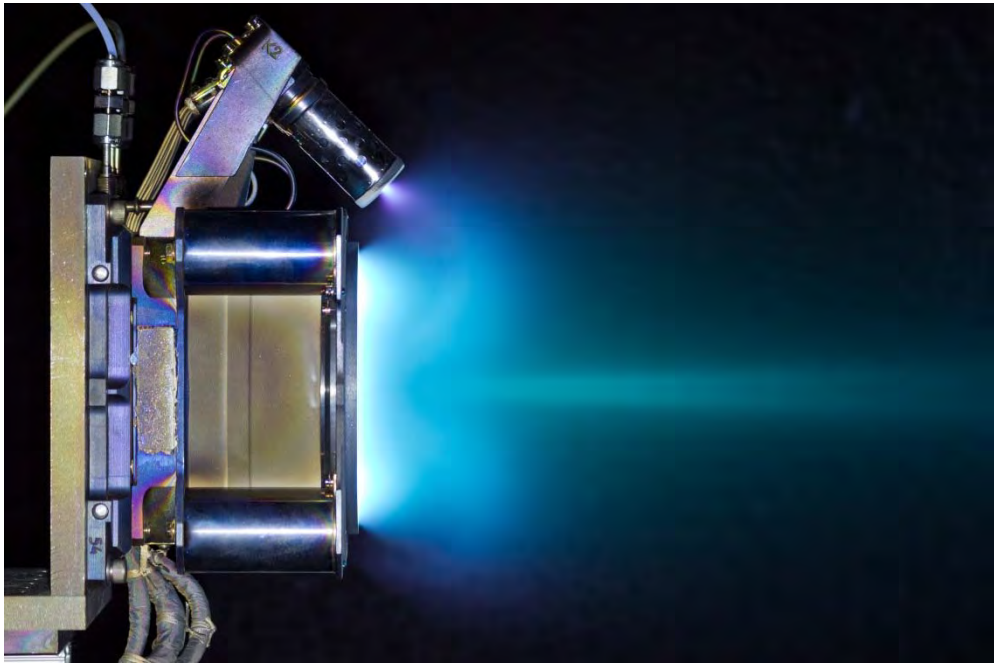

Operating Condition	V_d (V)	I_d (A)	Power (W)	$\dot{m}_a$ (mg/s)	$\dot{m}_c$ (mg/s)	$\dot{m}_b$ (mg/s)	P (Torr-Xe)	P (Pa-Xe)
Nominal	300	4.61	1383	5.15	0.40	0	2.28E-05	3.04E-03
High Back. Press.	300	4.57	1371	5.15	0.40	4.22	4.55E-05	6.07E-03
Low Dis. Voltage	210	4.60	966	5.15	0.40	0	2.09E-05	2.79E-03
High Dis. Voltage	390	4.56	1778	5.15	0.40	0	2.08E-05	2.78E-03
Low Prop. Flow Rate	300	2.90	870	3.60	0.28	0	1.52E-05	2.03E-03
High Prop. Flow Rate	300	5.99	1797	6.69	0.51	0	2.74E-05	3.66E-03

Comparison of Ion and Neutral Emission Radiance (arb. unit)

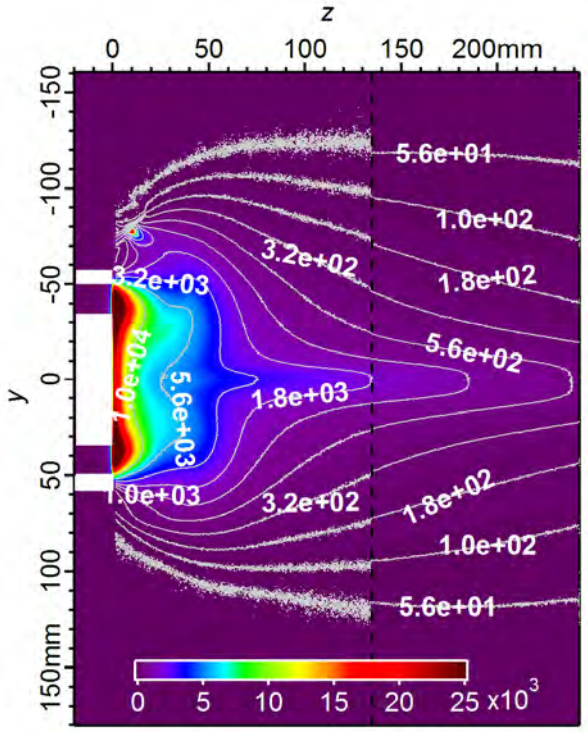

542 nm (ion)

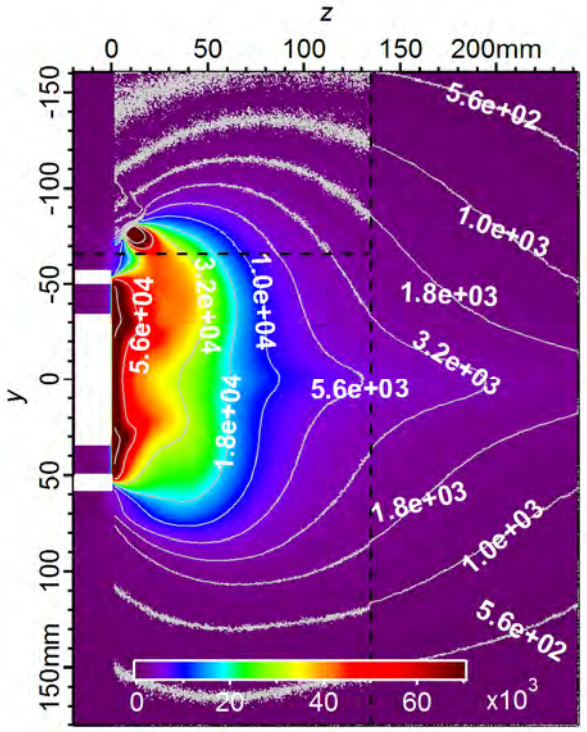

823 nm (neutral)

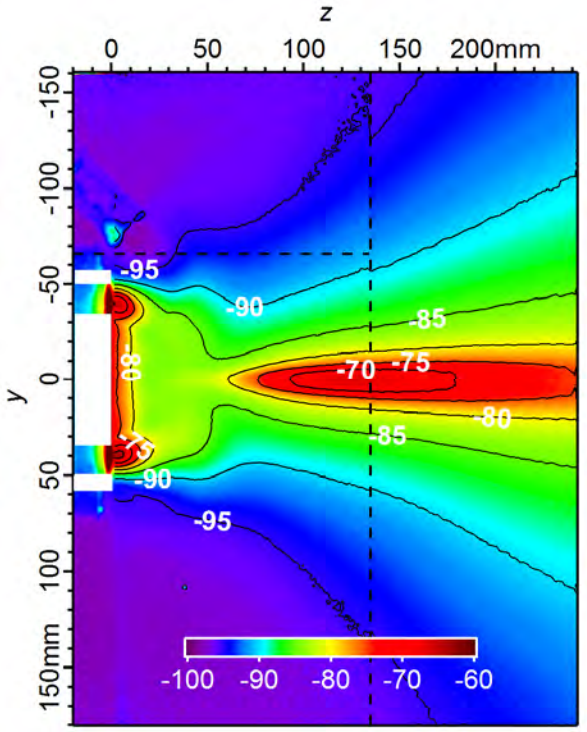

$$\Delta R(\%) = \frac{(R_{542:Nom} - R_{823:Nom})}{R_{823:Nom}} \times 100$$

- Neutral emission is greater than ion emission throughout plume, especially at the cathode (26× greater radiance)
- Highest regions of relative ion emission found at channel exits and central plume core, lowest regions outside of plume beam

542 nm (Ion) Emission Double BG Press. Radiance (arb. unit)

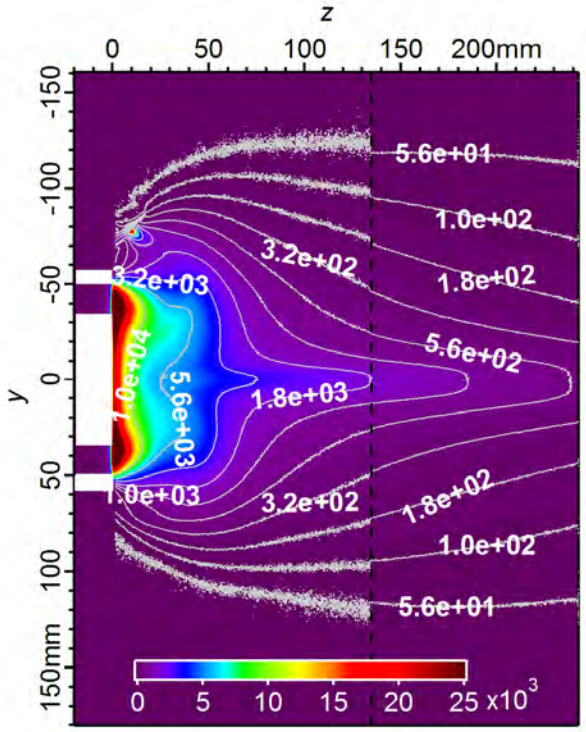

Nominal (P = 2.3e-5 Torr)

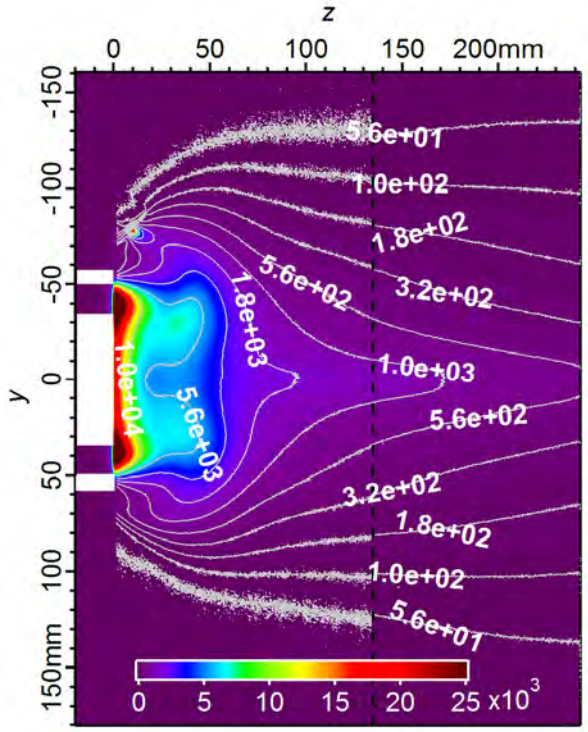

High Pressure (P = 4.6e-5 Torr)

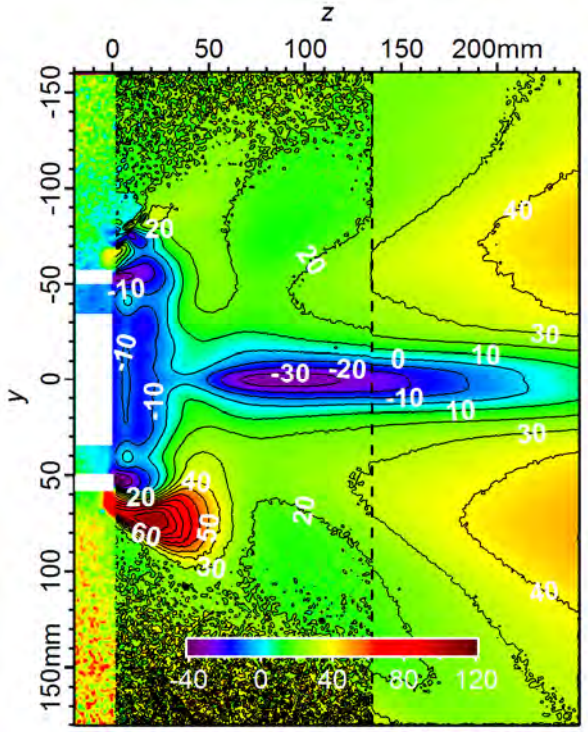

$$\Delta R(\%) = \frac{(R_{542:DP} - R_{542:Nom})}{R_{542:Nom}} \times 100$$

- Higher thrust measured as background pressure increases due mostly to less plume divergence*
- Asymmetrical region of high emission at *z* = 20, y = 75 mm
- Lower emission in plume core and near exit plane, higher elsewhere
  - Maybe less beamlet divergence from channel exits, from upstream shift of ion acceleration region
- Similar emission at channel exit.

*Diamant, K. D., Liang, R., and Corey, R. L., "The Effect of Background Pressure on SPT-100 Hall Thruster Performance," *Proceedings of the 50th AIAA/ASME/SAE/ASEE Joint Propulsion Conference*, 2014, AIAA-2014-3710.

823 nm (Neutral) Emission Double BG Press. Radiance (arb. unit)

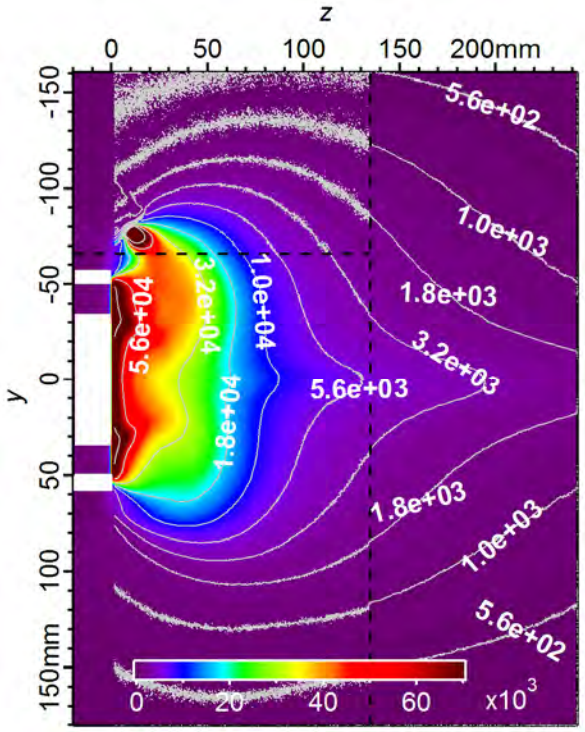

Nominal

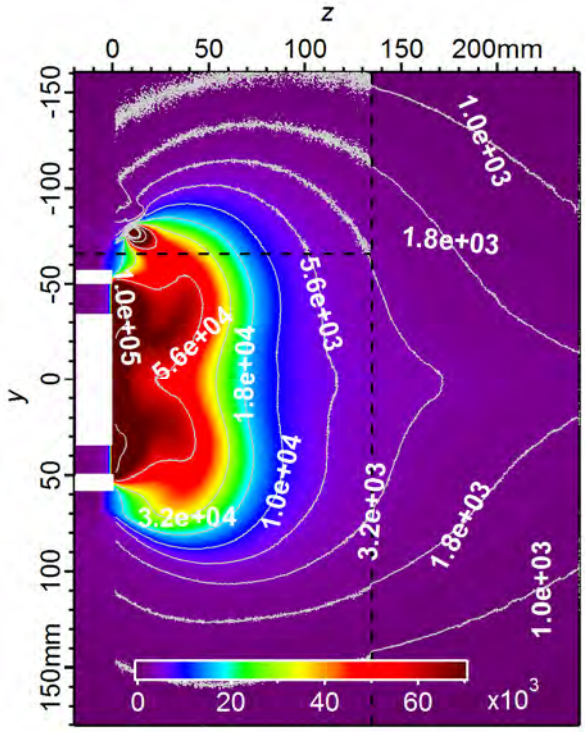

Double BG Pressure

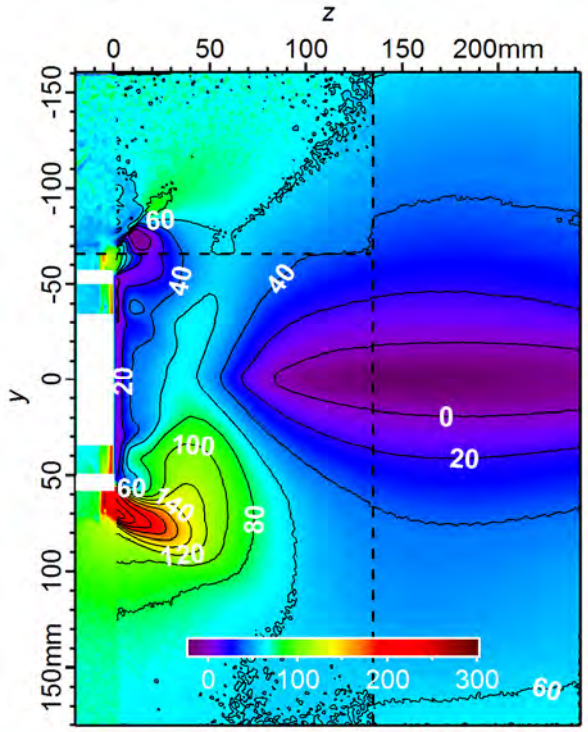

$$\Delta R(\%) = \frac{(R_{823:DP} - R_{823:Nom})}{R_{823:Nom}} \times 100$$

- Similar, but more intense asymmetrical region of high emission at z = 20, y = 75 mm as ion emission
- Broader low emission region in plume core beyond z = 50 mm

Radial Profiles: Double BG Press. vs. Nominal

542 nm (ion)

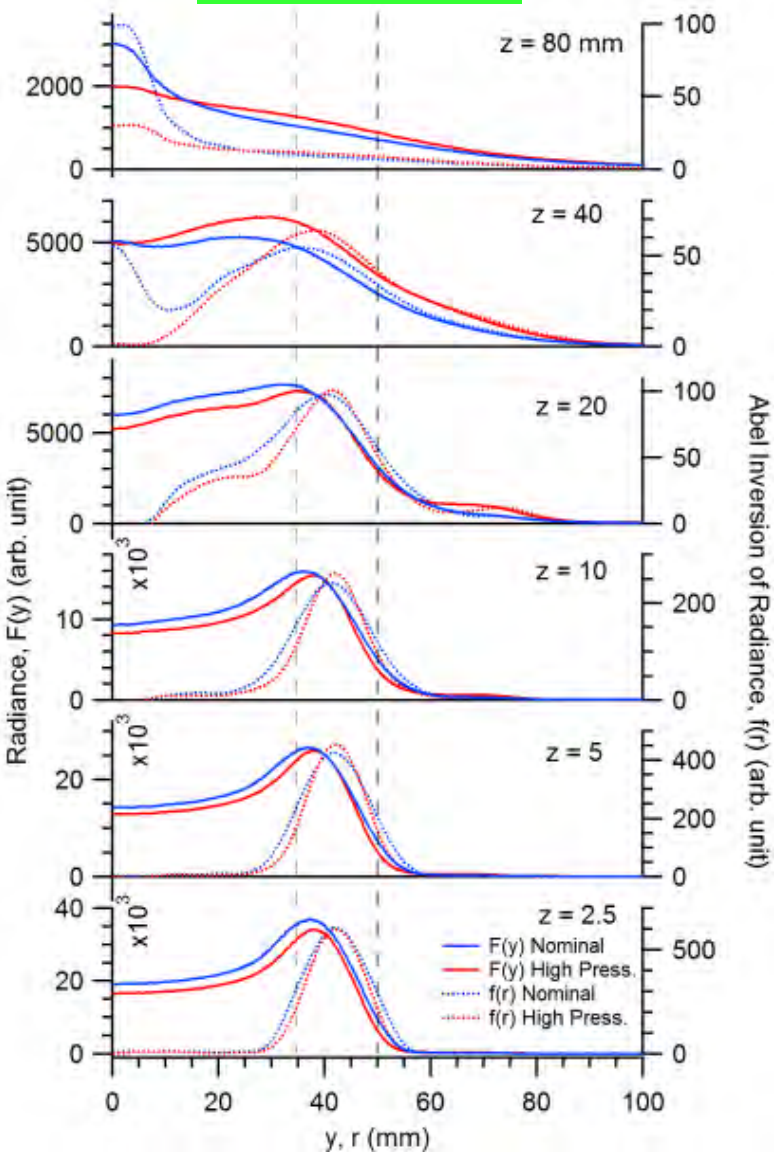

823 nm (neutral)

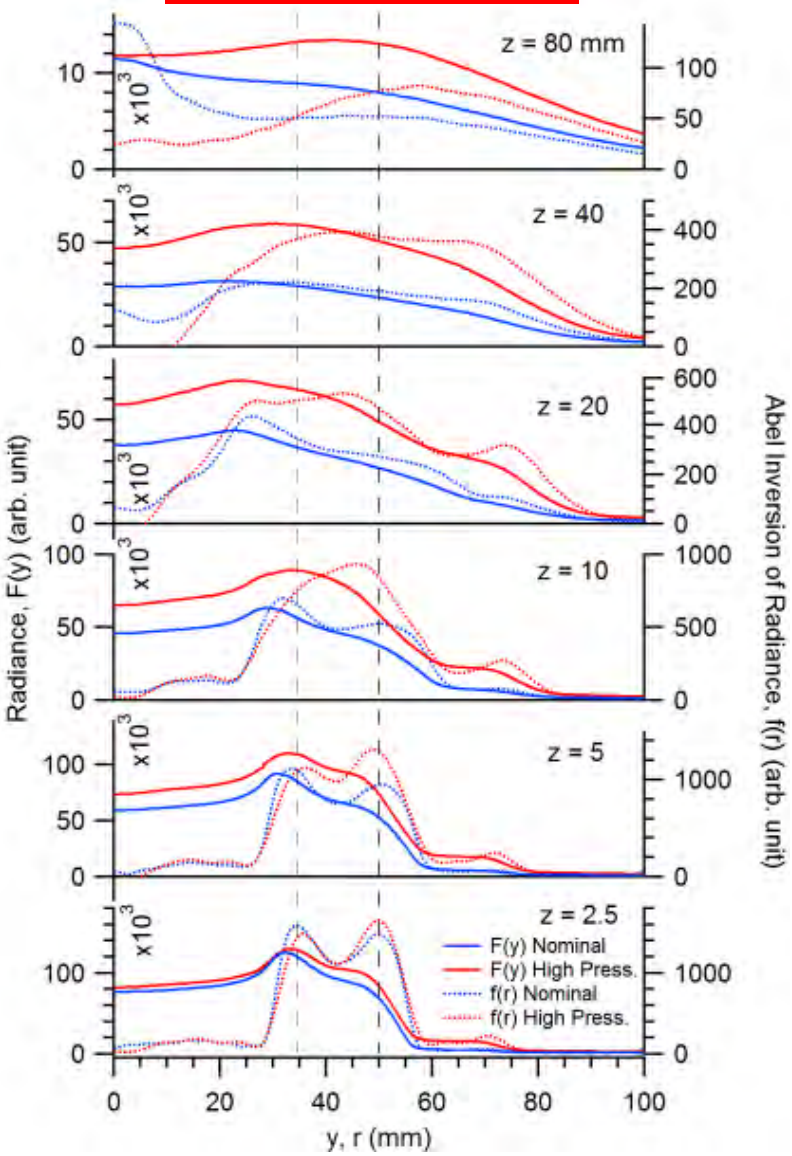

542 nm (Ion) Emission V_d Variations
Radiance (arb. unit)

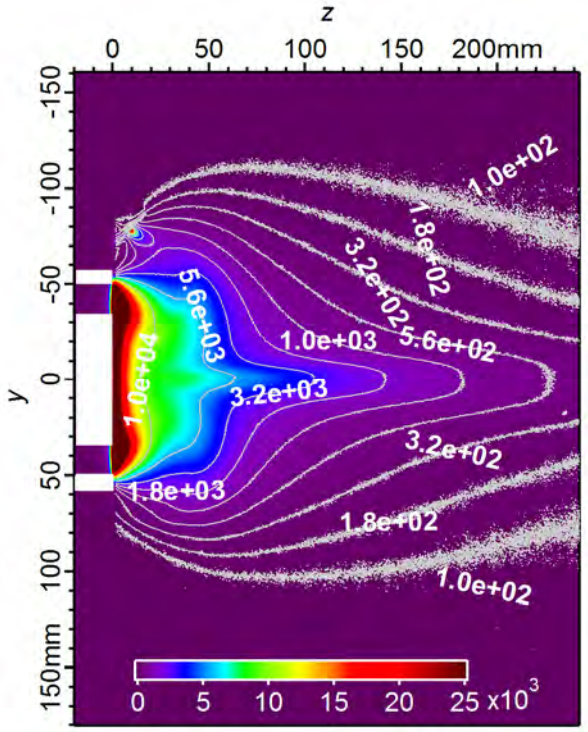

V_d = 210 V

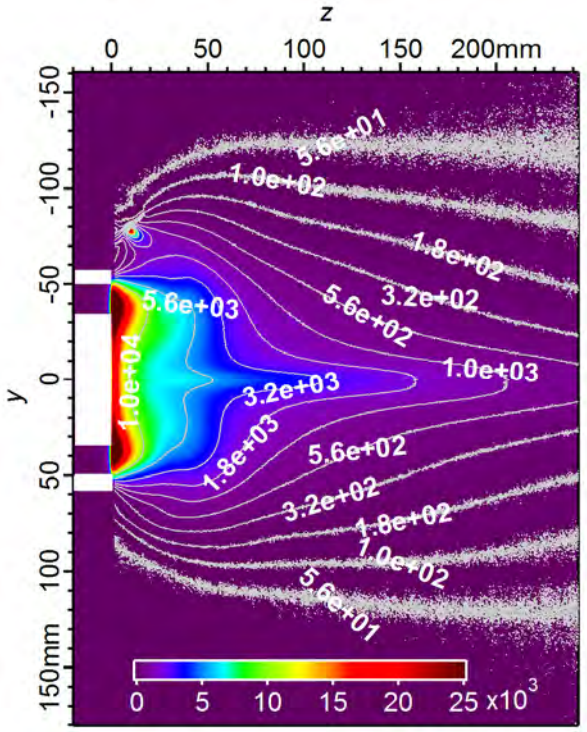

V_d = 390 V

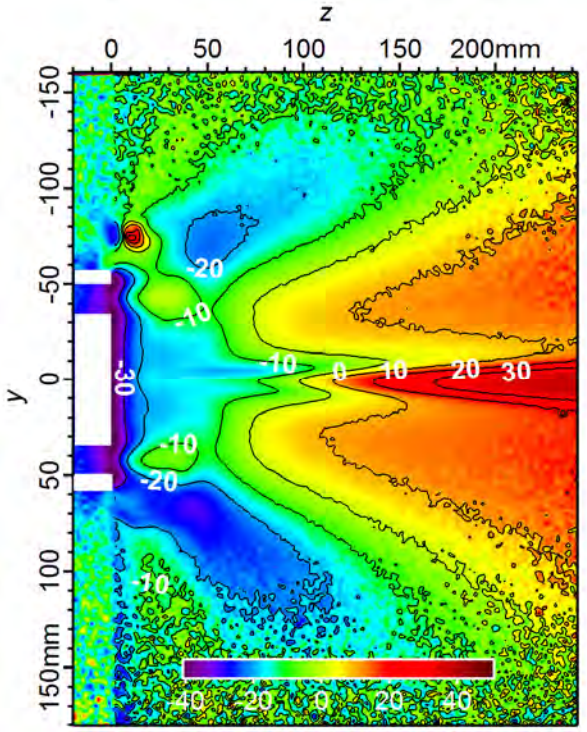

$$\Delta R(\%) = \frac{(R_{542:Vd390} - R_{542:Vd210})}{R_{542:Vd210}} \times 100$$

- Greater emission in plume beyond z = 100 mm, lower upstream
- Maybe beam interaction is occurring farther downstream with the faster ions

823 nm (Neutral) Emission V_d Variations
Radiance (arb. unit)

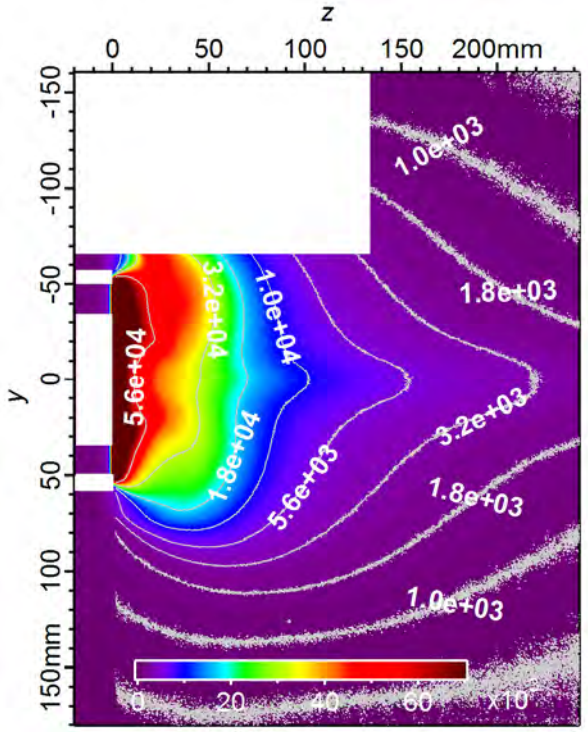

V_d = 210 V

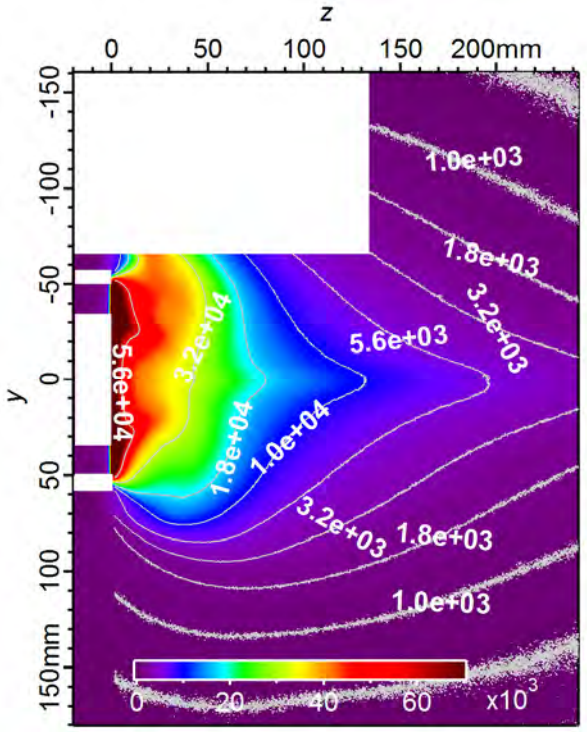

V_d = 390 V

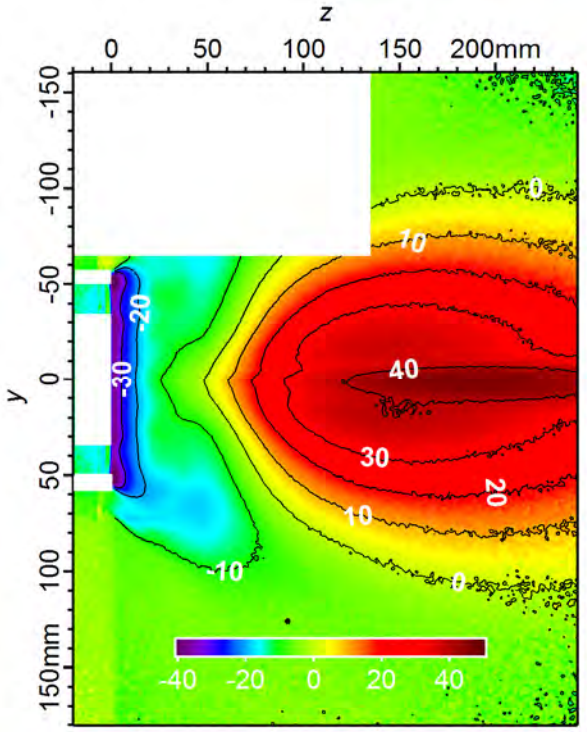

$$\Delta R(\%) = \frac{(R_{823:Vd390} - R_{823:Vd210})}{R_{823:Vd210}} \times 100$$

- Similar changes compared to ion emission, but with broader plume emission features

Radial Profiles: V_d = 210 V vs. V_d = 390 V

542 nm (ion)

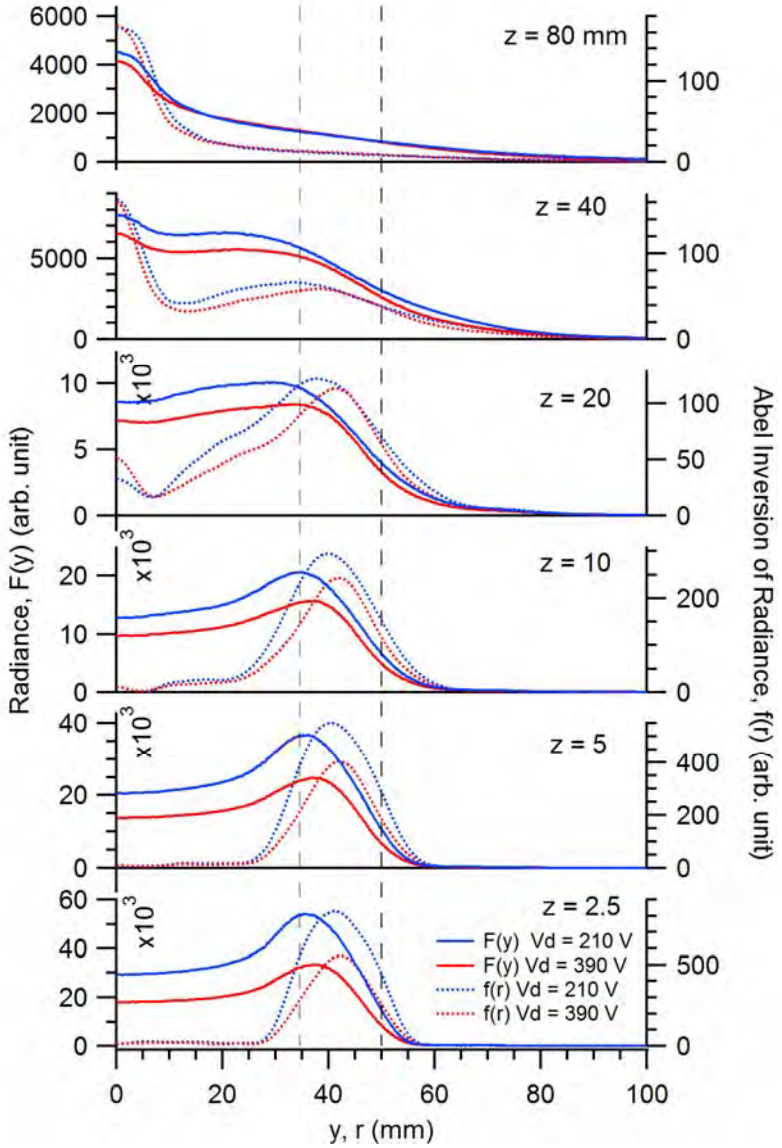

823 nm (neutral)

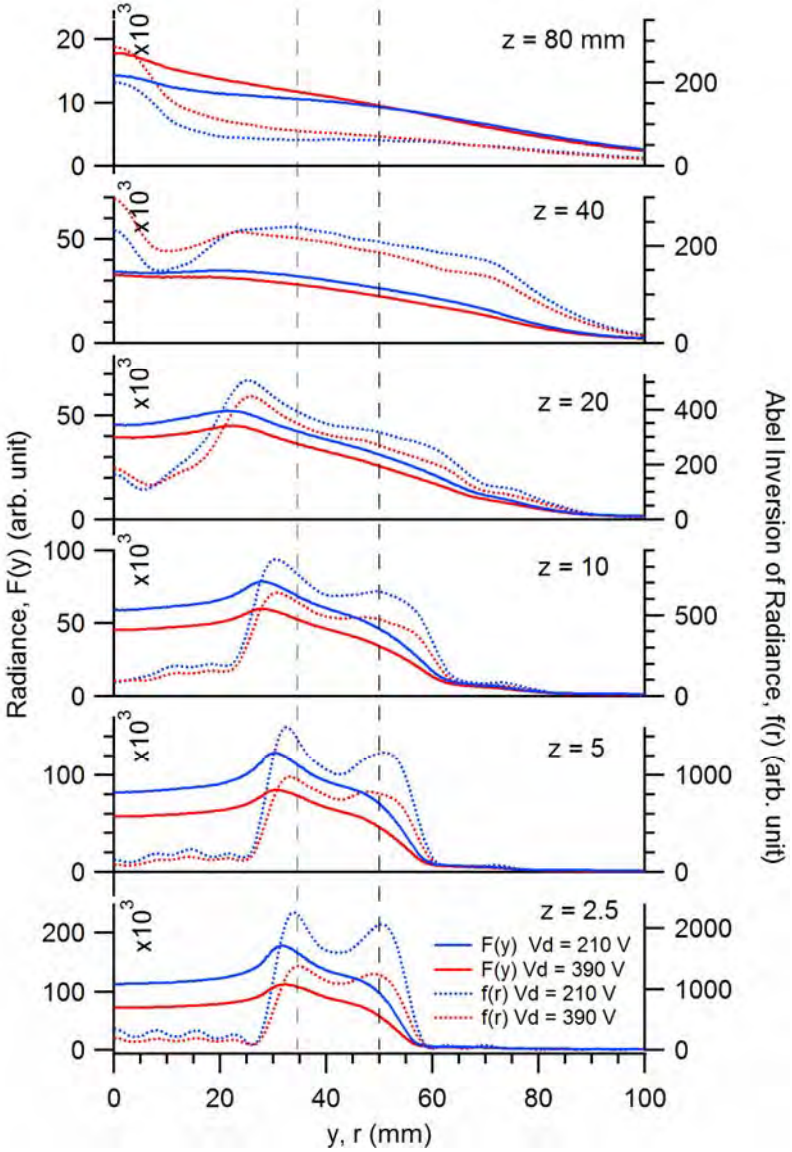

542 nm (Ion) Emission $\dot{m}$ Variations
Radiance (arb. unit)

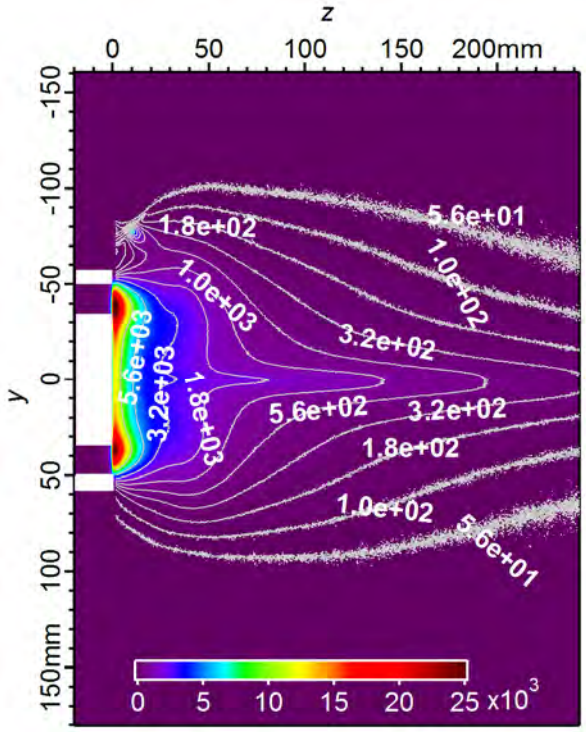

$\dot{m}$ = -30% ($\dot{m}$ = 3.88 mg/s)

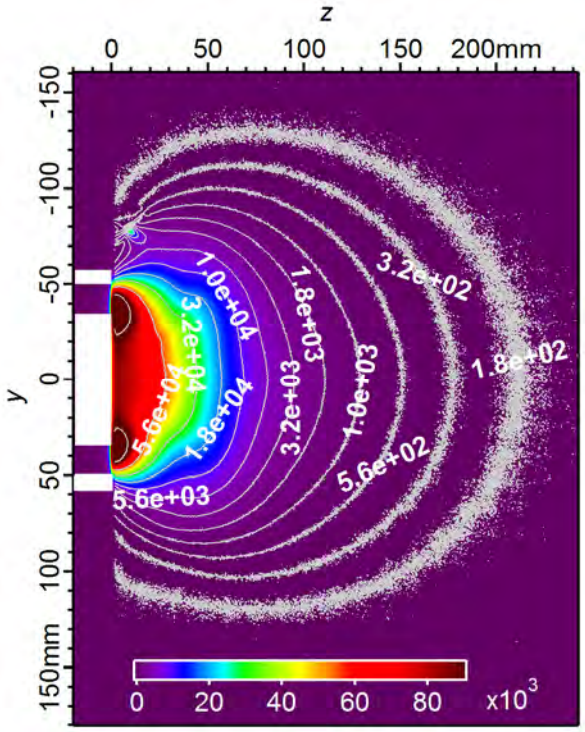

$\dot{m}$ = +30% ($\dot{m}$ = 7.20 mg/s)

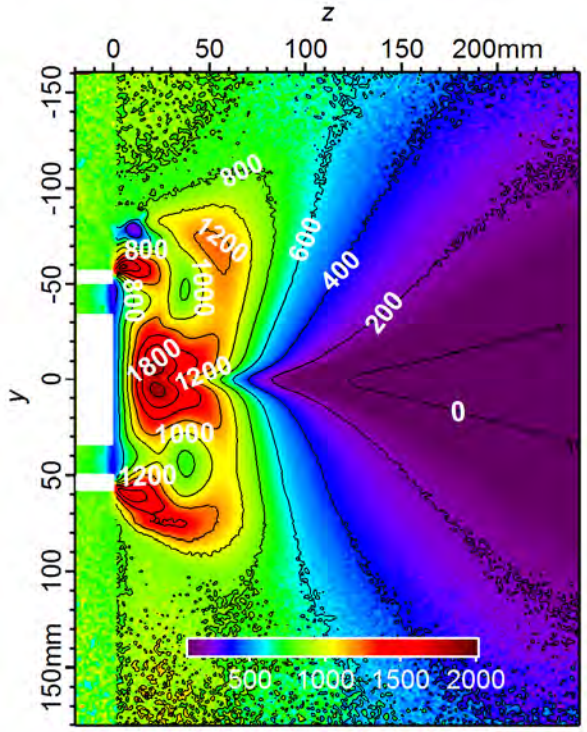

$$\Delta R(\%) = \frac{(R_{542:\dot{m}+30\%} - R_{542:\dot{m}-30\%})}{R_{542:\dot{m}-30\%}} \times 100$$

- Dramatic increase in emission for high propellant flow rate (note color scale change)
  - Highest increase directly downstream of center magnetic pole and outside of channel
  - More collisions with unionized propellant
- Spherical emission shape different from other cases
  - Scattering collisions diffusing plume

823 nm (Neutral) Emission $\dot{m}$ Variations
Radiance (arb. unit)

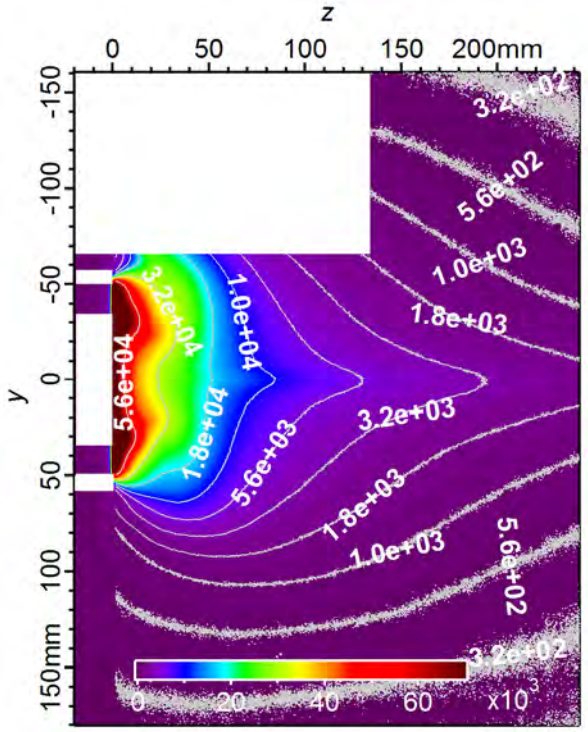

$\dot{m}$ = -30% ($\dot{m}$ = 3.88 mg/s)

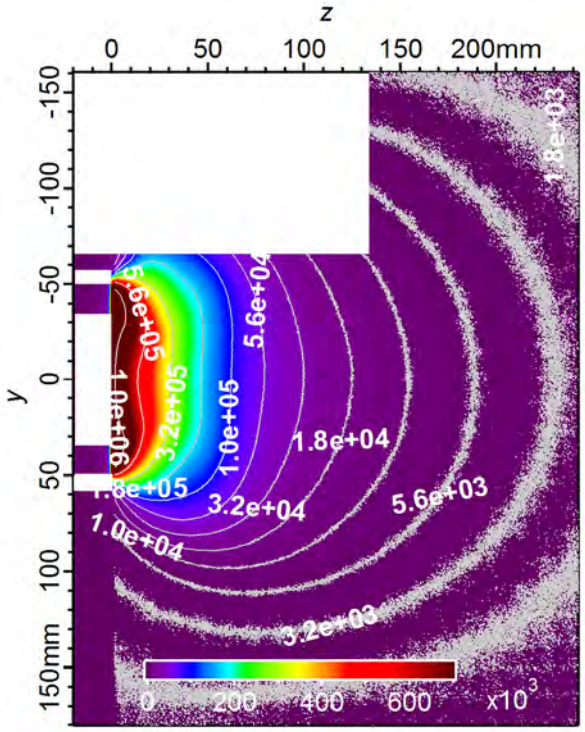

$\dot{m}$ = +30% ($\dot{m}$ = 7.20 mg/s)

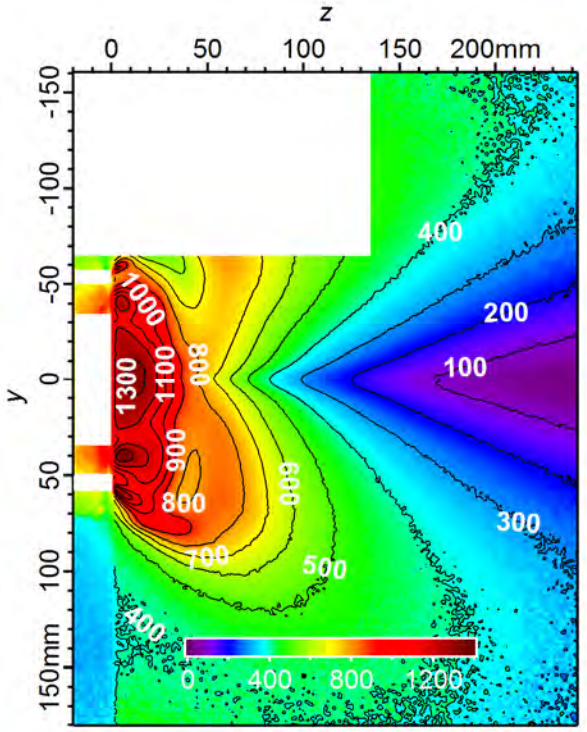

$$\Delta R(\%) = \frac{(R_{823:\dot{m}+30\%} - R_{823:\dot{m}-30\%})}{R_{823:\dot{m}-30\%}} \times 100$$

- Similar changes to plume emission shape as seen for 542 emission
  - High increase in emission directly downstream of channel exit

Conclusions and Future Work

- **Conclusions**
  - **Optical Technique**
    - High degree of repeatability
    - Exposures of separate regions of plume scaled well for composite image increasing dynamic range of data
    - Inverse Abel inversion analysis technique performed well overall
      - Resolved emission detail related to acceleration channel geometry
      - Similar neutral distribution shape across channel as seen in LIF density measurements SPT-140 near-field plume*
      - A few problem areas near $r = 0$ where $f(r) < 0$
  - **Plume Analysis**
    - Distinct changes in emission structure of plume observed for various operating conditions

- **Future Work**
  - ❑ **Model Comparison**
    - Perform measurements to match a numerical model of the near-field plume that includes CRM
    - Compare experimental and numerical results for model validation
    - Examine scaling of emission with density in numerical results to see if photographic density estimates are appropriate
  - ❑ **Probe Comparison**
    - Directly measure density and/or temperature with a probe in the near-field
    - Compare results with emission data to see if density can be estimated from emission where temperature gradients are adequately low
    - Photograph probe in plume to examine the perturbation as function of emission
  - ❑ **Apply experimental technique with high speed camera to study breathing mode**

*Crofton, M. et al., "Neutral Density in the SPT-140 Near-Field Plume," *Proceedings of the 33rd International Electric Propulsion Conference*, 2013, IEPC-2013-399.

Abel Inversion Technique Equations

Forward Abel Inversion

$$h(y) = 2 \int_y^R f(r) \frac{r}{\sqrt{r^2 - y^2}} \, \mathrm{d}r$$

Inverse Abel Inversion

$$f(r) = -\frac{1}{\pi} \int_y^R \frac{\mathrm{d}h(y)}{\mathrm{d}y} \cdot \frac{\mathrm{d}y}{\sqrt{y^2 - r^2}}$$

Approximate *f(r)* as cosine func. expansion

$$f(r) = \sum_{n=N_l}^{N_u} A_n f_n(r)$$

$$f_0(r) = 1 \,,$$

$$f_n(r) = 1 - (-1)^n \cos\left(n \pi \frac{r}{R}\right)$$

Forward Abel Inversion becomes

$$H(y) = 2 \sum_{n=N_l}^{N_u} A_n \int_y^R f_n(r) \frac{r \, \mathrm{d}r}{\sqrt{r^2 - y^2}}$$

Set each integral term numerically

$$h_n(y) = \int_y^R f_n(r) \frac{r \, \mathrm{d}r}{\sqrt{r^2 - y^2}}$$

Perform least squares fit to fit amplitude values A_n

$$2 \sum_{n=N_l}^{N_u} \left(A_n \sum_{k=1}^{N} h_n(y_k) \, h_m(y_k) \right) = \sum_{k=1}^{N} h(y_k) \, h_m(y_k),$$

$$\forall m: \; N_l \le m \le N_u$$

$$\sum_{k=1}^{N} [H(y_k) - h(y_k)]^2 \stackrel{!}{=} \text{Min}$$

*Pretzier, G., Jger, H., Neger, T., Philipp, H., and Woisetschlger, J., “Comparison of Different Methods of Abel Inversion Using Computer Simulated and Experimental Side-On Data," *Zeitschrift fr Naturforschung*, Vol. 47a, 1992, pp. 955-970.